Neutron stars dynamics and the dense matter equation of state

by Michał Bejger

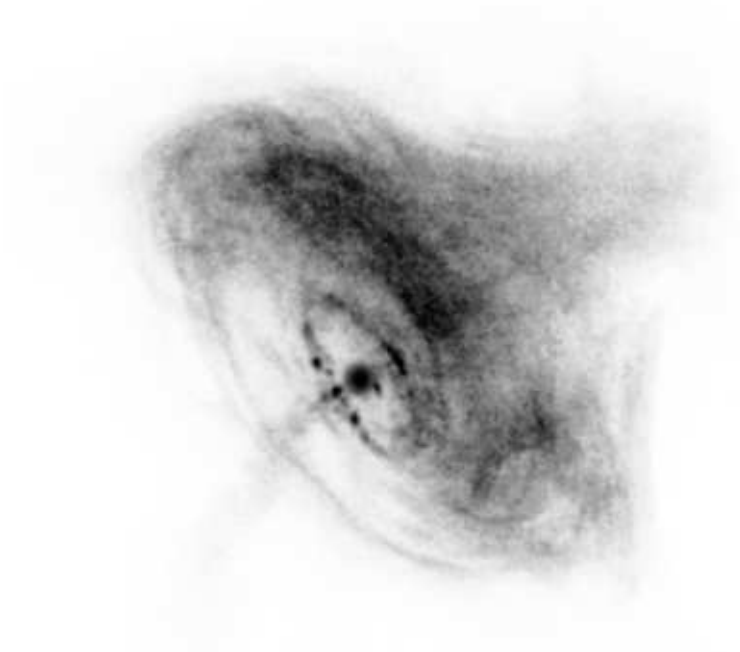

Centrum Astronomiczne im. Mikołaja Kopernika PAN
(Nicolaus Copernicus Astronomical Center, Polish Academy of Sciences)
April 2005

Abstract

Neutron stars can be treated as the ultimate laboratories for testing theories of dense matter. I present several different approaches to numerically model the signatures of dense matter in the observational behavior of astrophysical objects, namely:

- phase transition induced star-quakes and the star's reaction to the appearance of a newly-born mixed-phase core – I provide estimates for the changes of stellar parameters (radius, moment of inertia, mass-energy) for both realistic and parametric (polytropic) equations of state,
- the influence of phase transitions on the observational parameters of rotating solitary pulsars and accreting stars – the properties of a temporal change of rotation rate induced by the softening of the equation of state (back-bending phenomenon) is studied by means of parametric equations of state, and the realistic examples are provided,
- the signatures of the equation of state at the last orbits of binary neutron star systems – I have obtained the gravitational wave frequencies at the last stable orbit of the inspiral phase for typical binary neutron star systems. Three *very different* realistic equations of state were used. The final frequencies are strongly correlated with the mass to radius ratio of component stars. Moreover, calculated data sets can be used as the initial conditions during the simulations of realistic hydrodynamical merger.

I hope that future astrophysical observations will be used to constraint these calculations which in this way will contribute to our knowledge of the equation of state of dense matter.

Acknowledgements

I would like to thank my thesis supervisor Prof. Paweł Haensel and Dr Leszek Zdunik with whom I collaborated during my PhD studies. I have enjoyed their fruitful comments, constant encouragement and interest in my work – our numerous scientific discussions have been of great value to me.

A significant part of the thesis work was completed during my visits to the Observatoire de Paris-Meudon (section LUTH). I am very grateful to my French collaborator, Dr Eric Gourgoulhon and the `LORENE` team for their warm hospitality, support and extraordinary numerical codes.

I acknowledge the Polish-French Jumelage/LEA Astro-PF collaboration programs, the State Committee for Scientific Research (KBN) and the Ministry of Science and Information Society Technologies (MNiI) grants as well as the CNRS/PAN exchange program without which I could have not financed my scientific collaboration with the `LORENE` group and my access to computing facilities.

I thank all the employees at Copernicus Center for providing a good working atmosphere, and my fellow students for their unforgettable companionship during these years. It has been a great pleasure to study at CAMK.

I thank Grzegorz Stachowski for many suggestions which greatly improved the text of my thesis.

Finally, I thank my family for their understanding and patience.

Cover photo: Crab nebula in X-rays, courtesy of NASA/CXC/ASU/Hester et al. (2001).

Table of contents

List of figures

List of tables

Chapter 1

Introduction

Neutron stars (NSs) are truly fascinating objects. They are the densest stars known - while about 10 km in radius, a NS has a mass approximately the same as the Sun (thus its mean density is greater than the density of an atomic nucleus). NSs are commonly treated as cosmological laboratories of nuclear and particle physics. Indeed, NSs provide an unique site for studying fundamental questions in physics and astrophysics, including the influence of super-strong magnetic fields, superfluidity and superconductivity, the properties of nuclear forces at high densities, possible phase transitions to exotic matter, and gravitational physics in the strong-field regime. Additional important input from nuclear physics is however required in order to resolve the mysteries of many interesting astrophysical problems. The cooperation between dense matter physics and astrophysics is developing rapidly due to the observational and experimental data becoming available from many space-born and Earth-based instruments. Our understanding of dense matter under extreme conditions is also constantly being improved through elaborate numerical techniques.

The story of NSs begins with the correct interpretation of experimental data by J. Chadwick (1932), who announced the discovery of the neutron. The theoretical prediction of the existence of NSs and their relation to supernova explosions was presented by W. Baade and F. Zwicky in a series of papers (Baade and Zwicky, 1934b,c,a). Another very important step was accomplished by Tolman (1939) and Oppenheimer and Volkoff (1939), who obtained the first spherically symmetric star models in hydrostatic equilibrium within the framework of General Relativity. They derived the maximum allowable

mass of NS to be approximately 0.7 $M_\odot$ using the equation of state (EOS) of a strongly degenerate gas of non-interacting neutrons (the EOS describes the relation between the pressure P and the density of matter ρ, and possibly other parameters). As we now know, this mass is far too low to properly explain the observational properties of NSs. The maximum allowable mass i.e. the limiting mass above which stable star configurations are not present (such mass exists for every EOS) is much higher because of the presence of strong interactions in dense matter (a repulsive force between particles provides additional pressure, thus increasing the maximum mass). Current observational data suggest that the maximum allowable mass is greater than 1.44 $M_\odot$ (from observations of relativistic binary pulsars), and probably even greater than $\simeq$ 1.6 $M_\odot$ (from white dwarf-neutron star binaries, Nice et al. 2004).

An enormous boost of activity was provided by the astrophysical observations of X-ray sources (Giacconi et al., 1962), and the discovery of the first radio pulsar (Hewish et al., 1968). Many hypotheses were proposed to explain the properties of these unknown objects e.g. models of pulsating white dwarfs, eclipsing and oscillating sources, but they were all ruled out. The last possibility were rotating magnetized NSs, a model proposed independently by Pacini (1967) and Gold (1968). Their claim soon received robust observational support through the discovery of Crab pulsar with its 33 millisecond period. Today we understand that many astrophysical phenomena cannot be explained without NSs. Objects like Soft Gamma Repeaters (SGR) and Anomalous X-ray Pulsars (AXP) are now considered to be NSs with superstrong magnetic fields $\sim 10^{15}$ G. Observations of glitches (sudden increases of spin frequency) are possibly related to the interaction of superfluid matter with normal matter inside NS. Accretion-powered millisecond pulsars in binary systems, X-ray pulsars, X-ray bursters, sources of quasi-periodic oscillations, and other sorts of transient bursting sources provide important informations about the physics of accretion and nuclear burning. Isolated NSs are best for measurements of surface temperatures and for modeling their cooling history, which is influenced by the interior composition. Finally, NSs in relativistic binary systems provide excellent opportunities to test General Relativity, study pulsar magnetospheres and detect gravitational waves.

At present it is commonly accepted that the huge range of densities inside

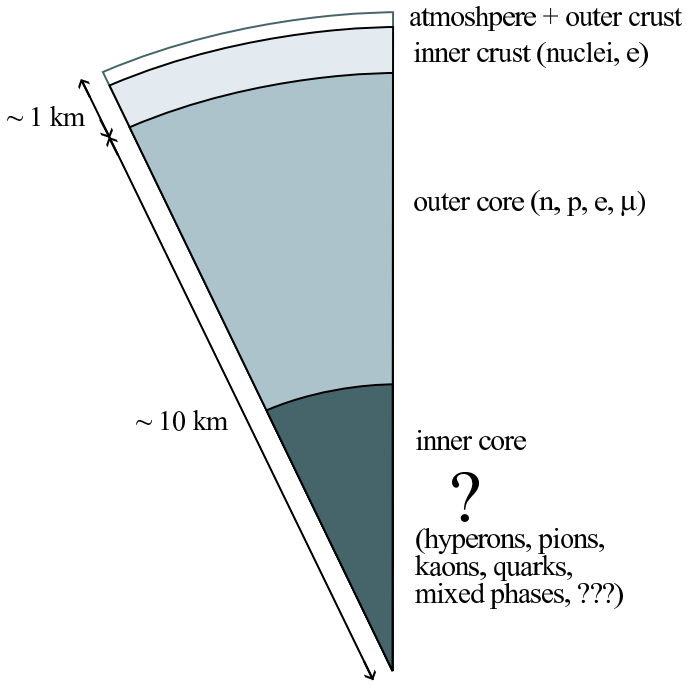

Figure 1.1: Schematic plot of the interior structure of neutron stars.

NS can be naturally divided into several regions (Fig. 1.1). To better visualize the state of dense matter, I also reproduce in Fig. 1.2 the behavior of the adiabatic index as a function of mass-density ρ for modern SLy EOS by Douchin and Haensel (2001). The adiabatic index equals $\gamma = \mathrm{d}\ln P/\mathrm{d}\ln n_\mathrm{b}$ (in their notation – Γ), where P is the pressure and n_b is the baryon density. The index γ describes the stiffness of matter (its susceptibility to compression) in relation to different regimes of the NS interior. The outermost part is called the *atmosphere*. This is a plasma layer, where the observed radiation is formed and emitted. The thickness of an atmosphere depends on its temperature – only a few millimeters for a cold ($T \sim 10^5$ K) star, it can become up to several centimeters thick for a hot star (with temperature greater than 10^6 K). The region below the atmosphere extending up to densities of around $\rho_\mathrm{nd} \simeq 4 \times 10^{11}$ g/cm^3 (the neutron-drip density denoted by dotted line in Fig. 1.2) is called the *outer crust*. This layer is a few hundred meters thick, and consists of nuclei and a strongly degenerate gas of relativistic electrons (with the exception of the surface layer in hot stars, in which non-degenerate electrons exist). The pressure is provided by a gas of electrons, non-relativistic for smaller densities ($\gamma \simeq 5/3$) and ultra-relativistic for densities $\gtrsim 10^8$ g/cm^3

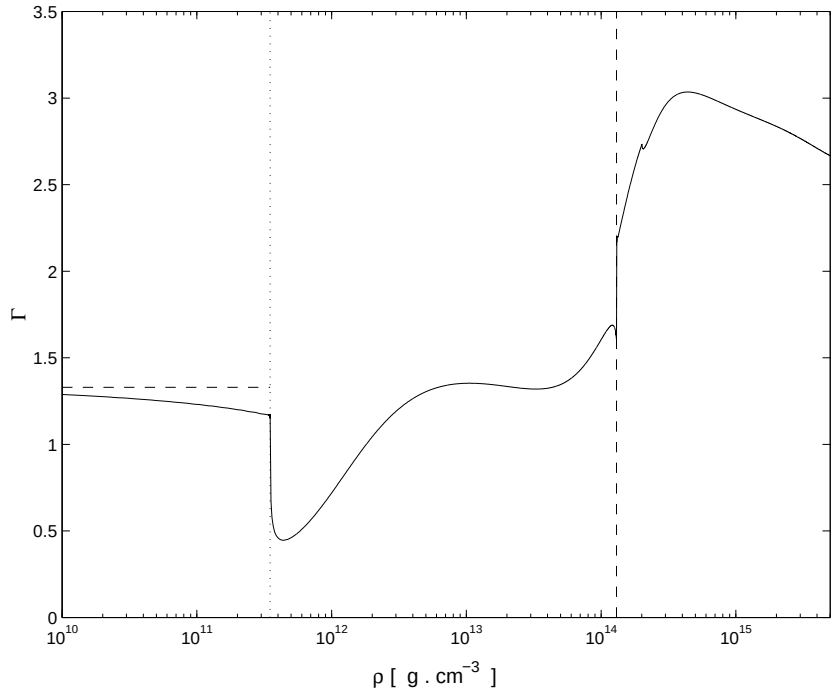

Figure 1.2: Adiabatic index as a function of density in the interior of NS (Douchin and Haensel, 2001). The dotted line denotes the neutron-drip density $\rho_{\rm nd}$, while the vertical dashed line denotes the crust-core interface density $\rho_{\rm cc}$ (the dashed horizontal line corresponds to $\gamma = 4/3$).

($\gamma \simeq 4/3$). The ions form a Coulomb liquid system for smaller densities and a Coulomb solid in the denser parts. The number of neutrons in nuclei grows with density because of the increasing Fermi energy of the electrons. At $\rho_{\rm nd}$, neutrons start to drip from nuclei and for higher densities they from a free gas in which the nuclei are immersed. The atmosphere and outer crust of massive ($\sim 1\ M_\odot$) NS constitute about 10^{-5} of the total mass of the star.

Below the outer crust is a region of about one kilometer in thickness, called the *inner crust*. It extends from the neutron-drip density $\rho_{\rm nd}$ to the crust-core density $\rho_{\rm cc}$. The precise value of $\rho_{\rm cc}$ is model dependent, and varies within $(0.6-1.4)\times 10^{14}$ g/cm^3 (crust-core interface is denoted by dashed vertical line in Fig. 1.2). Matter in the inner crust is composed of free neutrons (which can be in superfluid state), neutron-rich nuclei, and electrons. The appearance of free neutrons at $\rho_{\rm nd}$ is related to a strong decrease in the stiffness of matter. The increasing number density of neutrons leads, however, to repulsive interactions which recover the higher stiffness of matter for densities close to $\rho_{\rm cc}$.

Near $\rho_{\rm cc}$ nuclei can have shapes other than spherical (this result is however dependent on the specific model). The mass of the inner crust is of the order of 1% of the total mass.

For densities higher than $\rho_{\rm cc}$ the nuclei dissolve forming nuclear matter. This region of NS is called *outer core* and extends to about twice the nuclear density, $\rho_{\rm nuc} = 2.8 \times 10^{14}$ g/cm^3. From the assumption of β-equilibrium we expect that the composition of the outer core consists of neutrons, protons, electrons and muons – all those components are strongly degenerate, with nucleons possibly in a superfluid state. The thickness of the outer core is several kilometers.

The *inner core* contains matter of a density significantly larger than the normal nuclear density $\rho_{\rm nuc}$ (this density corresponds to the baryon number density $n_{\rm nuc} = 0.16$ fm^{-3}). For $\rho > \rho_{\rm nuc}$, the EOS of the core is poorly known, and this uncertainty grows rapidly with increasing density. The theoretical EOSs derived using different theories of dense matter and different methods of solution of the many-body problem differ significantly at 10^{15} g/cm^3, characteristic of the central cores of massive NSs. At the same time, the properties of the inner core have most influence on the structure of NSs and, e.g. on the value of the maximum allowable mass of NS.

In the next section, I will briefly describe some of the hypotheses the concerning composition of the inner core and outline the mechanisms of possible phase transitions.

1.1 Phase transitions in dense matter

Despite the lack of precise Earth-based experimental data involving matter at densities much higher that the nuclear saturation density $\rho_{\rm nuc}$ it is possible that astrophysical observations of compact objects will provide a unique chance of understanding the underlying physics. Observations in various electromagnetic bands (radio, visual, infrared, X-rays, γ-rays) will be used to constrain many of the intrinsic properties of these stars, including their masses, radii, magnetic fields, and internal structure. Moreover, we may hope that in the near future we will observe the imprint of possible phase transitions leading to a state of matter not observed in terrestrial laboratories.

Through the years, researchers have postulated condensation of bosons, e.g. pion condensate (Migdal, 1971, 1972; Sawyer, 1972; Scalapino, 1972), as a result of strong pion-nucleon attraction which leads to generation of a condensate of pion-like excitations. Condensation of kaons, mesons with non-zero strangeness appearing in dense matter due to weak processes, was proposed by Kaplan and Nelson (1986) – they showed that the negative kaons could form a zero-momentum state for densities few times the nuclear saturation density, $\rho_{\rm nuc}$.

Apart from bosons, it was also proposed that quarks, the fundamental building blocks of hadrons, should manifest themselves in dense matter. The existence of de-confined quarks in the dense cores of compact stars was first postulated by Ivanenko and Kurdgelaidze (1965); Itoh (1970) calculated star configurations built from a free gas of massive quarks. The "MIT bag" model of quark confinement in their own QCD vacuum was proposed by Chodos et al. (1974) and Baym and Chin (1976). This model was motivated by the self-bound strange matter hypothesis (Witten, 1984; Farhi and Jaffe, 1984) and was used to construct models of self-bound quark stars, Haensel et al. (1986a) and Alcock et al. (1986).

The creation of other strange particles, namely hyperons, is not as exotic as quark de-confinement, and thus is more probable. The existence of hyperonic degrees of freedom in dense matter was first postulated by Cameron (1959) and Salpeter (1960). Unfortunately, even after forty years our knowledge of nucleon-hyperon and hyperon-hyperon interactions is still insufficient to build reliable models. The overview by Weber (1999) as well as Heiselberg and Hjorth-Jensen (2000) covers recent developments in understanding the exotic phases of matter.

Throughout this work the "new" phase (new particles) will be represented by S (superdense) phase, whereas the "old" phase will be called N (normal) phase. Creation of the N phase results in the *softening* of the EOS. At a threshold density, the appearance of new degrees of freedom moderates the pressure increase P as a function of density – i.e. decrease of the adiabatic index, $\gamma = \mathrm{d}\ln P/\mathrm{d}\ln n_{\rm b}$ – the particle degeneracy is reduced and energy is consumed in the production of massive particles. In other words, new fermion particles soften the EOS because they are more massive than the existing "old"

particles, and when they start to fill their Fermi sea they replace the highest energy particles. In the case of boson condensates, the condensate contributes to the energy, but not to the pressure, because the particles occupy a single state.

At present, it is not entirely clear how the new S phase will appear in the surrounding N matter, as the order of the transition – first, second or even higher – is not certain. The difference between the orders is significant: if the transition is of second order, the new phase appears instantly after the threshold pressure is exceeded – the formation of an S phase core in the center of the star is quasi-static. If, however, the phase transition happens to be of first order, the consequences from the point of view of the observations are more interesting. In a first order phase transition the new phase arises by *nucleation*, which means that the meta-stable core formed during the star's evolution (e.g. accretion, spin-down) converts itself into a stable new-phase core. This transition is accompanied by a star-quake, energy (latent heat) release, radius change and possible other violent phenomena. The nucleation is related to fluctuation in density and/or composition in the meta-stable phase.

If the temperature is sufficiently high, for example in the protoneutron-star stage, the S phase can nucleate via *thermal fluctuations* (Landau and Lifshitz, 1993; Lifshitz and Pitaevskii, 1981; Langer, 1969). In some cases, it is essential for several conditions to be fulfilled, as was shown by Norsen (2002) who discussed formation of a kaon-condensed core. Very high temperatures $\simeq 10^{11}$ K and low kaon effective masses are needed because of the slowness of weak-interaction processes. Favorable surroundings are created in newly born NSs, with sufficient mass for the central density to exceed that required for kaons to appear. There is a problem, though: it may be that the NSs are born with the canonical mass of $\simeq 1.4\ M_\odot$ which can be too low to have the right density. Moreover, if their mass increased via accretion processes, the temperature in the center may already dropped below the threshold suitable for nucleation of kaons. Below a certain characteristic temperature $T_c \lesssim 10^9$ K thermal fluctuations become insignificant, and the new phase (if any) arises only by *quantum fluctuations* corresponding to the tunneling effect (Lifshitz and Kagan, 1972). However, as long as the pressure stays below a certain value, the nucleation of the S phase in the quantum regime is impossible (the

nucleation time is infinite). At some pressure larger than the critical pressure nucleation starts and the pure S phase fills the center of the star, up to the critical pressure, as proposed by Iida and Sato (1997, 1998) for the nucleation of de-confined quarks into the baryonic matter.

I will mainly focus on the first order phase transitions, as they are more interesting from an astrophysical point of view. First order phase transitions in one-component substances have well-known properties. Only one chemical potential, which corresponds to conserved baryon number, is needed. A familiar every-day example is the liquid-vapor transition in water – vapor cooled at constant pressure (or compressed at constant temperature) will condense to liquid water. The two phases are in equilibrium when their chemical potentials, pressures and temperatures are equal:

$$\begin{aligned} \mu_{\mathrm{N}} &= \mu_{\mathrm{S}} = \mu \ , \\ T_{\mathrm{N}} &= T_{\mathrm{S}} = T \ , \\ P_{\mathrm{N}}(\mu,\ T) &= P_{\mathrm{S}}(\mu,\ T) = P_0 \ , \end{aligned} \tag{1.1}$$

Fixing the temperature enables us to obtain a unique value of the chemical potential μ, constant through the phase transition and independent of the proportions of phases. The method of constructing such type of equilibrium phase transition is often called the "equal area" or "Maxwell construction" method (see Landau and Lifshitz 1993, §84). The energy density and baryon number density is equal to

$$\mathcal{E} = (1-\chi)\mathcal{E}^{\mathrm{N}} + \chi\mathcal{E}^{\mathrm{S}} \ , \tag{1.2}$$

$$n_{\mathrm{b}} = (1-\chi)n_{\mathrm{N,b}} + \chi n_{\mathrm{S,b}} \ , \tag{1.3}$$

where the values are volume averaged, and χ is the volume fraction of phases. The absence of a pressure gradient, i.e. the constancy of pressure (P_0 through the phases), means that in the presence of gravitational field the phases are physically separated in space – there is a density jump between them.

In the case of dense matter composed of baryons we can expect that, due to β-stability we will have at least two independent conserved numbers: baryonic and electric charge. Therefore, it is not correct to treat dense matter as a simple substance – it has more than one chemical potential. In the previous example the *local* electric charge neutrality condition was fulfilled, trivially;

now it should be substituted by the more physical *global* (macroscopic) electric charge neutrality. Taking this assumption into account opens the possibility of realization of a *structured mixed phase* i.e., such first order phase transition which leads to an intermediate state of matter between one pure phase and another – a mixture of phases with non-trivial geometry (bubbles, rods, plates) supported by Coulomb and surface tension interactions and spanned on a interval of pressures. The importance of relaxation of the local electrical neutrality condition was noted by Glendenning (1991, 1992). For two charges, baryonic and electric, the following conditions should be fulfilled:

$$\begin{aligned} &\mu_{\mathrm{N,b}} = \mu_{\mathrm{S,b}} = \mu_{\mathrm{b}} \ , \\ &\mu_{\mathrm{N,e}} = \mu_{\mathrm{S,e}} = \mu_{\mathrm{e}} \ , \\ &T_{\mathrm{N}} = T_{\mathrm{S}} = T \ , \\ &P_{\mathrm{N}}(\mu_{\mathrm{b}},\ \mu_{\mathrm{e}},\ T) = P_{\mathrm{S}}(\mu_{\mathrm{b}},\ \mu_{\mathrm{e}},\ T) \ , \end{aligned} \tag{1.4}$$

where μ_{b} and μ_{e} are baryonic and electric chemical potentials, respectively.

In a realistic matter model, if the surface tension and Coulomb contribution to the energy is not too large, the mixed phase is preferred over a state of pure phases. The thermodynamical equilibrium in a mixture of N and S phases and its bulk properties are obtained by the calculation of the minimum of the mixture energy density

$$\mathcal{E} = (1-\chi)\mathcal{E}^{\mathrm{N}} + \chi\mathcal{E}^{\mathrm{S}} + \mathcal{E}_{\mathrm{surf}} + \mathcal{E}_{\mathrm{Coulomb}} \ , \tag{1.5}$$

where $\mathcal{E}^{\mathrm{N}}$, $\mathcal{E}^{\mathrm{S}}$, $\mathcal{E}_{\mathrm{surf}}$ and $\mathcal{E}_{\mathrm{Coulomb}}$ are energy densities of N and S particles, surface and Coulomb contribution, respectively. The densities are averaged over a volume; it is important in this case to assume that the size of the region occupied by a droplets of new phase is sufficiently large compared to the characteristic size of the droplets. The minimalization is done under the constraint of macroscopic electrical neutrality, for a fixed average baryon density n_{b}:

$$\rho_{\mathrm{e}} = (1-\chi)\rho_{\mathrm{e}}^{\mathrm{N}} + \chi\rho_{\mathrm{e}}^{\mathrm{S}} = 0 \ . \tag{1.6}$$

where $\rho_{\mathrm{e}}^{\mathrm{N}}$ and $\rho_{\mathrm{e}}^{\mathrm{S}}$ are electric charge densities of N and S particles.

Coulomb and surface energies provide positive contributions to energy $\mathcal{E}$ as well as the chemical potentials. In Fig. 1.3 the mixed phase is plotted for

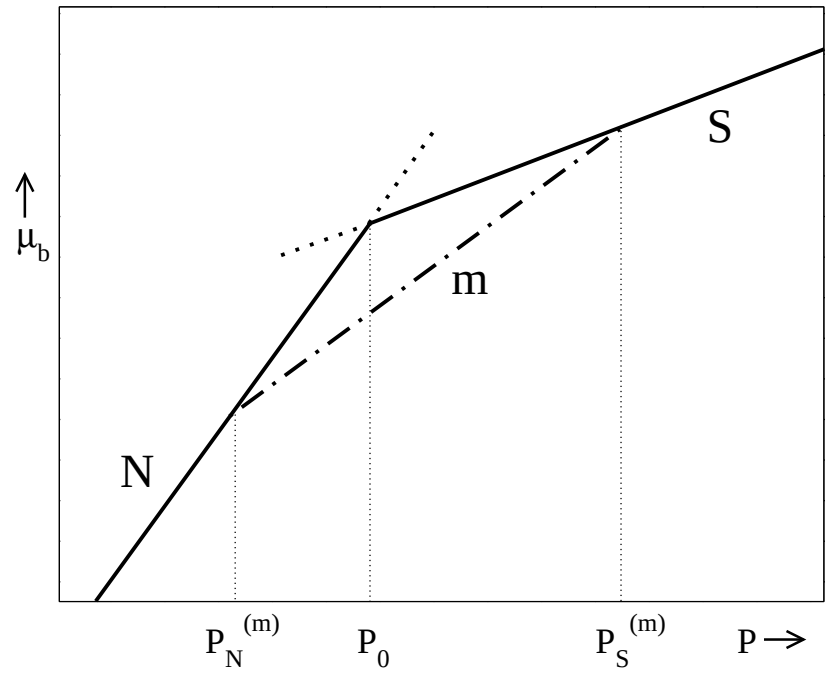

Figure 1.3: Baryon chemical potential $\mu_{\rm b}$ as a function of pressure P in the presence of an equilibrium first order phase transition, at $P = P_0$, between the N and S phases. The stable N phase is represented by the solid line; dotted lines represent *over-* and *under-compressed* states of N phase, meta-stable with respect to the transformation into the S phase. Mixed m-phase ($P_{\rm N}^{\rm (m)} < P < P_{\rm S}^{\rm (m)}$) is denoted by the dash-dotted line.

the baryon chemical potential $\mu_{\rm b}$ as a function of the pressure P. The aforementioned contributions increase the mixed phase onset pressure $P_{\rm N}^{\rm (m)}$ and decrease the termination pressure $P_{\rm S}^{\rm (m)}$, thus increasing $\mu_{\rm b}(P)$ and narrowing the mixed-phase layer in the stellar interior. The competition between these two contributions determines the size, shape and spacing of the charged structures within the mixed phase. It is particularly important for the appearance of less populated phase at the edges of the mixed-phase region. Ravenhall et al. (1983) and Pethick and Ravenhall (1995) demonstrated that for periodic structure, the surface contribution is twice the Coulomb one (so-called virial theorem). If sufficiently large, the surface and Coulomb contributions can make the mixed phase not favorable from an energetic point of view: from calculations the difference in $\mu_{\rm b}(P)$ for the transitions between pure and mixed phases is usually small, although it must be said that the surface contribution to the energy is most often not known precisely (see e.g., Heiselberg et al. 1993 for an example of the hadron-quark transition). The importance of the surface of the new phase nuclei was also taken into consideration by Christiansen and

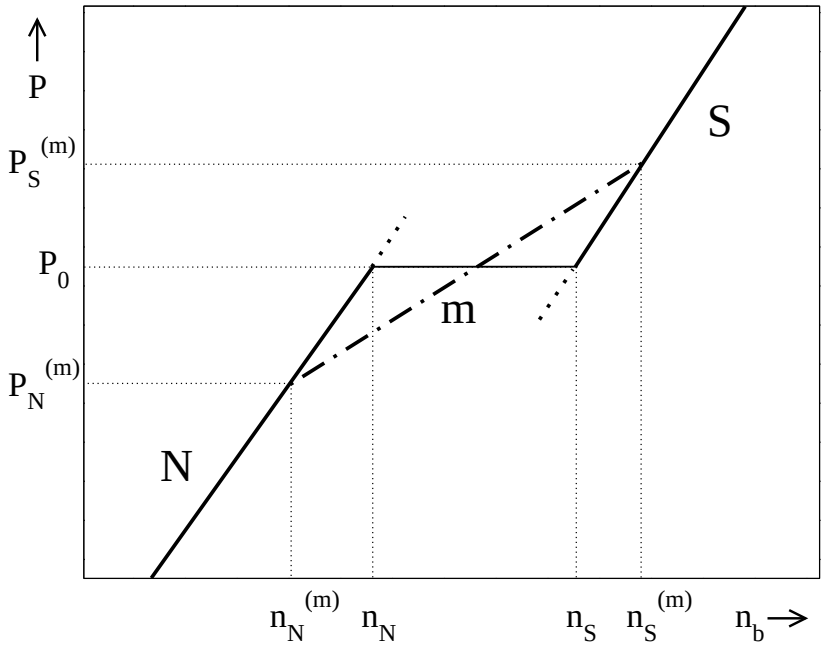

Figure 1.4: Schematic plot of mixed-phase EOS - pressure P as a function of baryon density $n_{\rm b}$, thin solid line denoted constant pressure phase transition between pure phases (notation of lines is the same as in Fig. 1.3).

Glendenning (1997); Christiansen et al. (2000) and Norsen and Reddy (2001).

A schematic mixed-phase state in the (P, $n_{\rm b}$) variables is presented in Fig. 1.4. First-order phase transition between the pure N and S phases is clearly visible - in Fig. 1.3 it corresponded to a single point at P_0. We see that for a N-S phase transition between pure phases the pressure P is constant between $P_{\rm N}^{(\rm m)}$ and $P_{\rm S}^{(\rm m)}$ while the density grows from $n_{\rm N}$ to $n_{\rm S}$. As was mentioned before, this situation results in a density jump configuration, because in the presence of the gravitational field P cannot provide an outward force to balance the gravitation. The mixed phase, however, spans between the densities $n_{\rm N}^{(\rm m)} < n_{\rm b} < n_{\rm S}^{(\rm m)}$ and pressures $P_{\rm N}^{(\rm m)} < P < P_{\rm S}^{(\rm m)}$ and can exist as a *structure* in the interior of the NS. The volume fraction occupied by the S phase grows monotonously with P, from zero at $P_{\rm N}^{(\rm m)}$ to one at $P_{\rm S}^{(\rm m)}$ - for $P > P_{\rm S}^{(\rm m)}$ only pure S phase is present. The calculations of a phases with kaon-condensed matter mixed with baryon matter were performed by Glendenning and Schaffner-Bielich (1998, 1999), Norsen and Reddy (2001) and Pons et al. (2000) in case of proto-neutron stars. Heiselberg et al. (1993) and Glendenning and Pei (1995) constructed

models of a mixed phase of de-confined quark matter coexisting with baryon phase; also Harko et al. (2004) presented recently a model of quark droplet nucleation.

Future observations will hopefully provide reliable evidence on possible phase transitions in NSs. So far the only precisely measured masses are those from relativistic binary systems. They are all around the "canonical" NSs mass of 1.35 $M_\odot$ – this mass agrees well with the supernova-core birth scenario. We also know that NS can acquire mass by accretion; the estimates for high NS masses are either uncertain, or it is not clear that the massive compact object is indeed a NS, and not a black hole. If the claims of massive $\simeq 2\ M_\odot$ NS (Quaintrell et al., 2003; Stairs, 2004; Nice et al., 2004) were to be proved correct, one would be obliged to abandon some EOSs of dense matter which are too soft, possibly due to phase transition, and therefore give small maximum mass and/or to reconsider the assumptions of the theories of dense matter. Either way, we can expect a well-defined signal on the dense matter EOS.

The thesis is arranged as follows: in Chapter 2 a brief description of numerical methods used in calculations is provided. Compact star's response to the appearance of a small mixed-phase core and the character of changes of stellar parameters following the creation of such core is studied in Chapter 3. The influence of phase transitions on the observational properties of rotating stars (solitary pulsars and accreting NSs) is discussed in Chapter 4. In Chapter 5 the inspiral evolution of realistic EOS binary NSs systems, driven by the loss of energy due to the emission of gravitational waves, is presented. Chapter 6 contains the summary. Moreover, I provide a set of appendices: Appendix A presents the thermodynamical properties of simple fluids, Appendix B contains the formulae describing sample parametric EOSs, Appendix C describes the spherically-symmetric star case (and the solution of Tolman-Oppenheimer-Volkoff equation), whereas Appendix D shows the method of calculation the moment of inertia of slowly rotating star. Appendix E contains the basics of spectral methods. The index, short glossary of terms and bibliography are placed at the end of the thesis.

Some of the results included in the thesis were presented by Bejger et al. (2005a,b) and Zdunik et al. (2004).

Chapter 2

Numerical methods in General Relativity

General Relativity (GR) is now almost one century old, and no one doubts it is a very successful theory. GR has turned around our understanding of space and time; while highly economic in assumptions, it has great predictive abilities. Einstein's field equations, which describe the properties of a gravitational field surrounding a given mass, can be written in beautiful compact form, as

$$\mathcal{G}_{\mu\nu} = 8\pi\mathcal{T}_{\mu\nu} \ , \tag{2.1}$$

where the left-hand side accounts for the *geometry* of spacetime and the right-hand side describes the *matter* placed in spacetime ($G = c = 1$). Einstein tensor $\mathcal{G}_{\mu\nu}$ is written as $\mathcal{G}_{\mu\nu} = \mathcal{R}_{\mu\nu} - \frac{1}{2}g_{\mu\nu}\mathcal{R}$, where $\mathcal{R}_{\mu\nu}$ in Ricci curvature tensor, $\mathcal{R} = \mathcal{R}^{\mu}_{\mu}$ is Ricci scalar and $g_{\mu\nu}$ is metric tensor. The stress-energy tensor, $\mathcal{T}_{\mu\nu}$ is responsible for the matter-energy. Most often its ideal fluid form is adopted in calculations:

$$\mathcal{T}_{\mu\nu} = (\mathcal{E} + P)u_{\mu}u_{\nu} + Pg_{\mu\nu} \ , \tag{2.2}$$

where $\mathcal{E}$ is matter-energy density, P is the pressure and u_{μ} is the 4-velocity of the fluid. Eq. (2.1) is often portrayed as the way of *matter* showing *spacetime* how to *curve* and *spacetime* forcing *matter* to *move*.

Among many theoretical constructs boldly anticipated by GR are gravitational waves, gravitational redshift as well as black holes, objects without which it would be extremely hard to explain many astrophysical phenomena. GR is involved in the clarification at the highest possible level – at cosmological scales

it predicts models of the whole Universe. It is also expected that soon we will *directly* detect the gravitational waves (as opposed to indirect detections from relativistic binary NSs).

The development of GR was slowed down in the past because of poor capability of computers and difficulties of finding the analytical solutions of Einstein field equations. Fortunately, numerical methods are finally mature enough for the ability of making *qualitative and quantitative* predictions concerning real astrophysical objects.

There were many attempts to find analytic solutions to the Einstein field equations for rapidly rotating compact objects. One may think that the exterior metric of a rapidly rotating neutron star is similar to that from the Kerr metric (Kerr, 1963), but the reality is different. As was shown by Hartle and Thorne (1969) the two metrics agree to the lowest order in the rotational frequency only. Recently, Manko et al. (2000) proposed a solution which approximates exterior gravitational field of the star by the use of its mass, angular momentum and quadrupole moment. Different approximations e.g. Shibata and Sasaki (1998) employing a multipole expansion of exterior spacetime far from the star were used to locate the innermost stable circular orbit and to study the accretion onto the surface of rapidly rotating NSs. Those methods are in quite good agreement with numerical results.

However, at present all *self-consistent* methods for obtaining the equilibrium configurations for rotating stars are numerical – no analytical solution which covers *whole* spacetime is known. First numerical solutions were proposed by Bonazzola and Maschio (1971) and Wilson (1972), improved by Bonazzola and Schneider (1974) with the application to the Crab pulsar and by Bardeen and Wagoner (1971) in the case of thin rotating disks. But even before these works, there was other approximate method called the "slow rotation formalism", proposed by Hartle (1967), and further applied by Hartle and Thorne (1968). Rotation was there treated as a perturbation over a spherically symmetric star profile, up to $\mathcal{O}(\Omega^2)$ order. Instead of complicated partial differential equations one had to solve a set of ordinary differential equations. The formalism was greatly improved by the efforts of Weber and Glendenning (1991, 1992), in particular by including the frame-dragging effect and rotational stretching of a star's profile, as well as more accurate estimate of the angular velocity at

the mass-shedding limit. However, as it was shown by Salgado et al. (1994), this method is suitable for calculating the rotation properties of simple fluids far from the the mass-shedding limit (as its name indicates), but it fails near the Keplerian frequency.

Method proposed by Butterworth and Ipser (1976) (BI code) assumes gradual procedure of treating a new rotating model as a linear perturbation of the previously computed rotating model – the iteration process starts with a non-rotating model and increases the angular velocity in small steps, while solving four linearized Einstein field equations. In this approximation, spacetime is truncated at some distance from the star by setting boundary conditions on metric potentials. The method was used also by Friedman et al. (1986) and Lattimer et al. (1990), who employed the realistic EOSs. Improved formalism of this type was presented by Komatsu et al. (1989a,b) (KEH code) – some of differential field equations were converted into integrals by means of Green functions. Similar to BI code, the region of integration is truncated at a finite distance from the star, but the boundary conditions are incorporated into the integrals. The method of solution is iterative. It was later improved by Cook et al. (1992) and Cook et al. (1994b,a) (CST code) by mapping the whole range of radial variable from the center to the infinity onto the compactified closed region. Still later on, Stergioulas and Friedman (1995) proposed their own (SF code) version of KEH/CST formalism. The above codes are based on finite difference schemes.

I will now describe the basic equations underlying numerical methods used in calculations presented in the thesis (as a general reference I find books by Misner et al. 1973 and Wald 1984 valuable). We will demand that the considered spacetime has several properties. Let us first focus on axisymmetric spacetime, for simplicity: we demand that it should be *stationary* (there should exist Killing vector field $\mathbf{e}_t$ which is timelike at spatial infinity) and *axisymmetric* (there should exist a Killing vector field $\mathbf{e}_\phi$, which vanishes on a timelike two-surface, the axis of symmetry, and is spacelike everywhere else with close orbits – of course, in the case of non-axisymmetric spacetimes e.g. for binary NSs systems this assumption will be dropped). Third property is the *asymptotic flatness*; with above assumptions it means that scalar products associated with the spacetime metric of $\mathbf{e}_t$ and $\mathbf{e}_\phi$ should be equal, respectively:

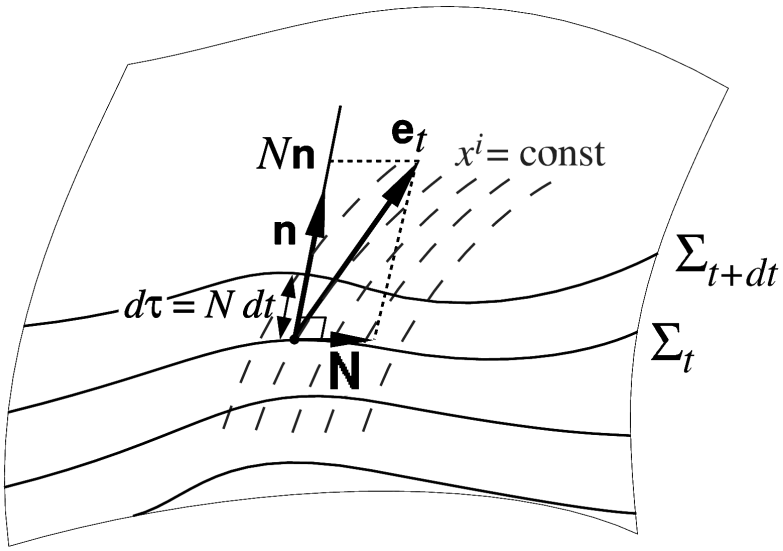

Figure 2.1: The 3+1 formalism of the foliation of spacetime into hypersurfaces. On the hypersurface Σ_t induced metric is defined, along with lapse N and shift $\mathbf{N}$ which describe the coordinate changes when traveling from Σ_t to $\Sigma_{t+\mathrm{d}t}$. Normal timelike vector $\mathbf{n}$ correspond to the Eulerian observers in the spacetime (based on the plot of Gourgoulhon 2004).

$\mathbf{e}_t\mathbf{e}_t = -1$, $\mathbf{e}_\phi\mathbf{e}_\phi = \infty$ and $\mathbf{e}_t\mathbf{e}_\phi = 0$ at spatial infinity. One can choose the coordinate system such that $e_t = \partial/\partial t$ and $e_\phi = \partial/\partial\phi$, where t is the coordinate time, and ϕ is the azimuthal angle coordinate. In general, asymptotically flat spacetimes have nice properties from a numerical point of view – they can be conformally compactified and are equipped in boundary conditions at infinity in a natural way.

Let us recall the general 3+1 formalism used frequently in numerical General Relativity. Einstein field equations split into *dynamical equations* and *constraint equations* in this formalism. It was invented to deal with the evolution of relativistic objects and to simulate their dynamics, but even without actually doing the dynamical calculations (which will be the case here) the formalism is still useful: it can provide initial data conditions for real time-dependent calculations. The formalism is based on foliation of the spacetime in a family of hypersurfaces Σ_t, labelled by coordinate time t (Smarr and York, 1978). In other words, the method separates time and three-dimensional space, hence its name. On each hypersurface the coordinate system is given. If $\mathbf{n}$ is the unit 4-vector normal to Σ_t and oriented in the direction of increasing t ($\mathbf{n}$ corresponds to the Eulerian observer in the spacetime), one can define the lapse function N as $\mathbf{n} = N\nabla t$, the metric induced on Σ_t is defined as

$\mathbf{h} = \mathbf{g} + \mathbf{n} \otimes \mathbf{n}$ and the shift vector equals $\mathbf{N} = -\mathbf{h}e_t$ ($\otimes$ denotes the tensor product, e.g. $\boldsymbol{A} = \boldsymbol{a} \otimes \boldsymbol{b}$, $A^{ij} = a^i b^j$).

The metric expressed in therms of lapse, shift and induced metric reads:

$$g_{\alpha\beta}\mathrm{d}x^\alpha \mathrm{d}x^\beta = -(N^2 - N_i N^i)\mathrm{d}t^2 - 2N_i \mathrm{d}t\, \mathrm{d}x^i + h_{ij}\mathrm{d}x^i\, \mathrm{d}x^j \ , \tag{2.3}$$

As pictured in Fig. 2.1, the lapse N provides the clock "ticking" and separates three-dimensional hypersurfaces defined by the foliation, giving the proper time $\mathrm{d}\tau = N\mathrm{d}t$ measured by the Eulerian observer. The shift vector $\mathbf{N}$ contains the information how much the spatial coordinates differ on subsequent hypersurfaces.

By decomposition of the general stress-energy tensor $\mathcal{T}$ into $\mathcal{T} = \mathbf{S} + \mathbf{n} \otimes \mathbf{J} + \mathbf{J} \otimes \mathbf{n} + E\mathbf{n} \otimes \mathbf{n}$, where $E = \mathcal{T}_{\mu\nu} n^\mu n^\nu$, $J_i = -h_i^\mu \mathcal{T}_{\mu\nu} n^\nu$ and $S_{ij} = h_i^\mu h_j^\nu \mathcal{T}_{\mu\nu}$ and by the orthogonal projection of Einstein's equations onto Σ_t and along the normal to Σ_t we get the Hamiltonian constraint and the momentum constraints equations

$$\mathcal{R} + K^2 - K_{ij}K^{ij} = 16\pi E, \quad D_j K^{ij} - D^i K = 8\pi J^i \ , \tag{2.4}$$

respectively, as well as the dynamical equations

$$\frac{\partial K_{ij}}{\partial t} - \mathcal{L}_{\mathbf{N}} K_{ij} = -D_i D_j N \ + $$

$$+ \ N\left(\mathcal{R}_{ij} - 2K_{ik}K^k_j + K K_{ij} + 4\pi\{(S-E)H_{ij} - 2S_{ij}\}\right) \ , \tag{2.5}$$

where D_i is the covariant derivative on $\mathbf{h}$, $\mathcal{R}_{ij}$ is the corresponding Ricci tensor, $\mathcal{R}$ is the Ricci scalar, K_{ij} is the extrinsic curvature tensor of the hypersurfaces Σ_t defined as $K_{\alpha\beta} = \frac{1}{2}\mathcal{L}_n h_{\alpha\beta}$, where $\mathcal{L}_n$ denotes Lie derivative along $\mathbf{n}$, $K := K^i_i$ and $S := S^i_i$. We also have a kinematic relation

$$\frac{\partial h_{ij}}{\partial t} + D^i N^j + D^j N^i = 2NK^{ij} \ , \tag{2.6}$$

between metric $\mathbf{h}$ and the curvature $\mathbf{K}$. In general, the resolution of Einstein's field equations amounts to the Cauchy problem i.e. to find the shape of the boundary and the reasonable solutions for the boundary conditions.

It is of course possible to slice the spacetime into hypersurfaces in various ways. The choice of slicing implemented in the numerical codes used in the thesis is

called the "maximal slicing", which is related to the extrinsic curvature tensor $\mathbf{K}$. Trace K equals the covariant divergence of $\mathbf{n}$, $K = -\nabla\mathbf{n}$. The maximal slicing condition is then $K = 0$, a particularly suitable condition for studying collapses and other dynamical phenomena, because of vanishing divergence of Eulerian observers as well as asymptotically flat slices. This condition is also exact for arbitrary relativistic spherical configurations and it is very accurate for axisymmetric rotating NSs (Cook et al., 1996).

Together with the maximal slicing condition the choice of spatial coordinates fully specifies the coordinate choice. In the numerical codes employed in the thesis, the quasi-isotropic gauge is used (Shapiro and Teukolsky, 1980), because it results in elliptic partial differential equations for which the existence and uniqueness theorems exist. Also, such coordinates cover whole spacetime generated by e.g. rotating object, from the center to infinity.

From a numerical point of view the most important feature is obviously the control of numerical errors during computation. Equilibrium configurations in Newtonian gravity satisfy the well-known virial theorem. In General Relativity there exists a different identity valid for a stationary and axisymmetric spacetime (Bonazzola, 1973). More recently, two other relativistic virial theorems were obtained. First of them, three-dimensional virial identity (Gourgoulhon and Bonazzola, 1994) is an extension of the Newtonian virial theorem to General Relativity. The two-dimensional (Bonazzola and Gourgoulhon, 1994) identity generalizes the mentioned identity found by (Bonazzola, 1973) for axisymmetric spacetimes to general asymptotically flat spacetimes. The identities of Bonazzola and Gourgoulhon (1994) and Gourgoulhon and Bonazzola (1994) will be used to check the accuracy of the codes.

In Sect. 2.1 I will briefly describe the numerical implementation of Bonazzola et al. (1993) method, called BGSM, improved later by Bonazzola et al. (1998) (`LORENE/rotstar`) for axisymmetric rotating stars. The code is based on multi-domain spectral methods (basic introduction to spectral methods can be found in Appendix E). Sect. 2.2 is devoted to similar type of code employed in the calculations of binary compact objects (Bonazzola et al., 1997, 1999a; Gourgoulhon et al., 2001). The numerical codes can be downloaded freely from `http://www.lorene.obspm.fr` (the homepage of C++ library `LORENE`). The main codes are called `rotstar.C` and `coal.C` and are located in the

`Lorene/Codes/Rot_star/` and `Lorene/Codes/Bin_star/` directories for isolated and binary NSs, respectively.

Through the next sections I will try to keep the original notation for the consistency with the original articles (short glossary of the most important symbols is located at the end of the thesis).

2.1 Rotating axisymmetric neutron stars

I will shortly describe equations which should be solved in order to obtain stationary axisymmetric rotating NS configuration. Numerical methods and tests, as well as detailed description of the code is contained in the articles by Bonazzola et al. (1993, 1999a). There were many previous calculations done with the code, and the numerical methods are well advanced, thanks to multi-domain spectral methods (Appendix E). These methods were used in the past to calculate stationary models of compact stars is order to determine their maximum mass, maximum rotation rates, innermost stable circular orbits frequencies, and to simulate accretion-induced spin-up for many models of dense matter.

In the quasi-isotropic coordinates with the assumption of maximal slicing, stationarity, axisymmetry and asymptotic flatness, the metric described by Eq. (2.3) takes a following form:

$$g_{\alpha\beta}\mathrm{d}x^\alpha \mathrm{d}x^\beta = -N^2\mathrm{d}t^2 + A^4B^2r^2\sin^2\theta(\mathrm{d}\phi + N^\phi \mathrm{d}t)^2 + \frac{A^4}{B^2}(\mathrm{d}r^2 + r^2\mathrm{d}\phi^2) \ , \quad (2.7)$$

where the lapse N, ϕ shift component N^ϕ, and conformal factors A and B are functions of r and θ. Following logarithms of metric potentials are defined as

$$\nu(r,\ \theta) := \ln(N), \quad \alpha(r,\ \theta) := \ln(A), \quad \beta(r,\ \theta) := \ln(B) \quad (2.8)$$

together with

$$G(r,\ \theta) := NA^2B, \quad \zeta(r,\ \theta) := \nu + 2\alpha - \beta \ . \quad (2.9)$$

The Hamiltonian and momentum constraints and the evolution equations – Eq. (2.4) and Eq. (2.5) give the following elliptic equations:

$$\begin{aligned}
\Delta_3\nu &= \frac{A^4}{B^2}\left[4\pi(E+S)+2(k_1^2+k_2^2)\right]-\partial\nu\partial(\nu+2\alpha+\beta)\ ,\\
\tilde{\Delta}_3\tilde{N}^\phi &= 16\pi\frac{N}{B^4}\frac{J_\phi}{r\sin\theta}-r\sin\theta\partial N^\phi\partial(6\alpha+3\beta-\nu)\ ,\\
\Delta_2\tilde{G} &= 8\pi\frac{NA^6}{B}r\sin\theta(S_r^r+S_\theta^\theta)\ ,\\
\Delta_2\zeta &= \frac{A^4}{B^2}\left[8\pi S_\phi^\phi+3(k_1^2+k_2^2)\right]-(\partial\alpha)^2\ ,
\end{aligned} \tag{2.10}$$

where the following notation was introduced:

$$\partial\alpha\partial\beta := \frac{\partial\alpha}{\partial r}\frac{\partial\beta}{\partial r}+\frac{1}{r^2}\frac{\partial\alpha}{\partial\theta}\frac{\partial\beta}{\partial\theta}\ ,\quad (\partial\alpha)^2:=(\partial\alpha)(\partial\alpha)\ , \tag{2.11}$$

$$\tilde{G}(r,\ \theta):=r\sin\theta G\ ,\quad \tilde{N}^\phi(r,\ \theta):=r\sin\theta N^\phi\ , \tag{2.12}$$

$$k_1 := -\frac{B^2 r\sin\theta}{2N}\frac{\partial N^\phi}{\partial r}\ ,\quad k_1 := -\frac{B^2\sin\theta}{2N}\frac{\partial N^\phi}{\partial\theta}\ , \tag{2.13}$$

and

$$\begin{aligned}
\Delta_2 &:= \frac{\partial^2}{\partial r^2}+\frac{1}{r}\frac{\partial}{\partial r}+\frac{1}{r^2}\frac{\partial^2}{\partial\theta^2}\ ,\quad \Delta_3:=\Delta_2+\frac{1}{r^2}\frac{1}{\tan\theta}\frac{\partial}{\partial\theta}\ ,\\
\tilde{\Delta}_3 &:= \Delta_3-\frac{1}{r^2\sin^2\theta}\ .
\end{aligned} \tag{2.14}$$

Eqs. (2.14) define the scalar Laplacian in two-dimensional flat space, the scalar three-dimensional Laplacian and the azimuthal ϕ component of vector three-dimensional Laplacian, respectively. Remaining quantities, E, $\mathbf{J}$ and $\mathbf{S}$, were defined by introducing Eq. (2.4) and Eq. (2.5).

In the perfect fluid case (Eq. 2.2) and with the assumption of absence of meridional currents, the fluid 4-velocity $\mathbf{u}$ is represented by its t and ϕ components:

$$\mathbf{u} := u^t\mathbf{e}_t+u^\phi\mathbf{e}_\phi\ . \tag{2.15}$$

We can define the fluid coordinate angular velocity

$$\Omega := \frac{u^\phi}{u^t} \tag{2.16}$$

as seen by an observer at infinity at rest with respect to the star. The Lorentz factor connecting the Lorentzian (co-moving with the fluid) observer and the Eulerian (static) observer is equal to

$$\Gamma := -\mathbf{nu} = Nu^t = (1-U^2)^{-1/2}\ . \tag{2.17}$$

Its relation to U, the physical fluid velocity in ϕ direction, can be also written as

$$U = \frac{A^2 B r \sin\theta}{N}(\Omega - N^\phi) = \mathbf{u}\frac{1}{\Gamma}\frac{\mathbf{e}_\phi}{|\mathbf{e}_\phi|} \ . \tag{2.18}$$

Dynamical quantities E, $\mathbf{J}$ and $\mathbf{S}$ in the case of perfect fluid are equal to

$$\begin{aligned} E = \Gamma^2(\mathcal{E} + P) - P \ , \quad J_\phi = (E+P)A^2 B U r \sin\theta \ , \\ S^r_r = S^\theta_\theta = P \ , \qquad S^\phi_\phi = P + (E+P)U^2 \ . \end{aligned} \tag{2.19}$$

Projection of the momentum-energy conservation equation $\Delta\mathcal{T} = 0$ orthogonally onto the hypersurface Σ_t leads to matter equation of motion. The first integral of motion is equal, for rigidly rotating star:

$$H(r,\ \theta) + \nu(r,\ \theta) - \ln\Gamma(r,\ \theta) = H(0,\ 0) + \nu(0,\ 0) = const., \tag{2.20}$$

where $H(r,\ \theta)$ is the log-enthalpy of the fluid, (Eq. A.7, see Appendix A for related definitions). Eq. (2.20) is the relativistic generalization of the Bernoulli theorem for stationary flow.

Several useful quantities have to be defined in order to get physical information about a rotating star. From the condition of asymptotic flatness we know the behavior of metric potentials near the infinity, for example $\nu(r,\ \theta)|_{r\to+\infty} \to\ 0$. In fact the leading term of the solution for ν from first equation of Eqs. (2.10) is equal to $\nu(r,\ \theta) \sim -M/r$. The quantity M is the gravitational mass of the star measured by a distant observer. By computing it carefully, one has

$$\begin{aligned} M \ &:= \ \int_{\Sigma_t} (2\mathcal{T}_{\mu\nu} - \mathcal{T} g_{\mu\nu}) n^\mu e^\nu_t \sqrt{h}\mathrm{dx}^3 = \\ &= \ \int \frac{N A^6}{B}\left(E + S^i_i + \frac{2}{N}N^\phi J_\phi\right) r^2 \sin\theta \mathrm{d}r\mathrm{d}\theta\mathrm{d}\phi \ . \end{aligned} \tag{2.21}$$

Additionally we have the baryon current $\mathbf{u}n_\mathrm{b}$, so that the number of baryons inside the star can be evaluated as

$$A_\mathrm{B} := -\int_{\Sigma_t} \mathbf{u}\mathbf{u} n_\mathrm{b}\sqrt{h}\mathrm{d}x^3 = \int \frac{A^6}{B}\Gamma n_\mathrm{b} r^2 \sin\theta \mathrm{d}r\mathrm{d}\theta\mathrm{d}\phi \ . \tag{2.22}$$

The baryon mass will be therefore

$$M_\mathrm{B} := A_\mathrm{B} m_0 \ , \tag{2.23}$$

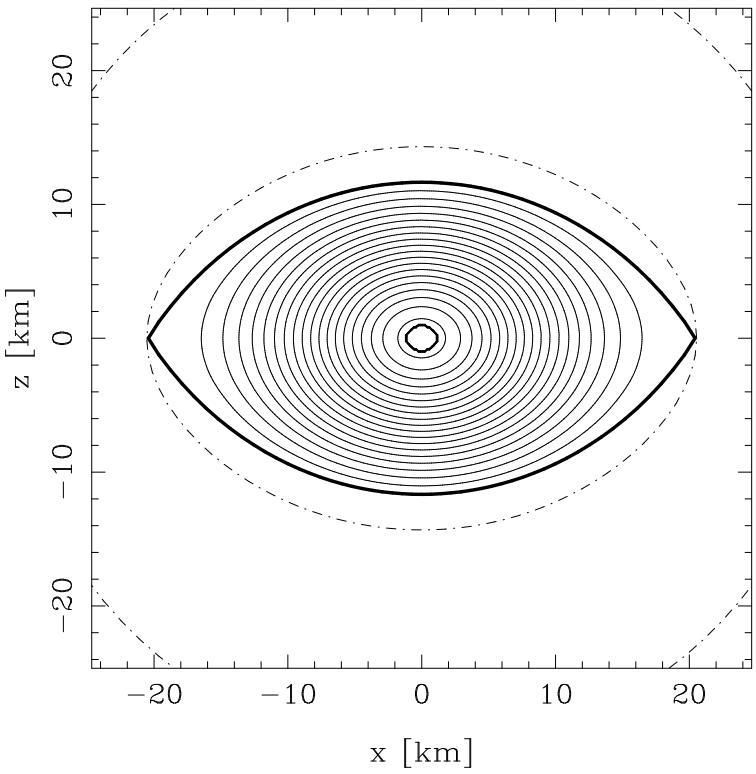

Figure 2.2: A star rotating with the Keplerian velocity. Star's EOS exhibits a constant-pressure phase transition with the density jump of $n_{\rm S}/n_{\rm N} = 1.25$ – the new dense phase is pictured as the small nucleus domain in the center; see also Fig. 2.3 for the profile of energy density.

where m_0 is the mass of the baryon particle (typically $m_0 = 1.66 \times 10^{-24}$ g $\equiv$ Mass(^{56}Fe crystal)/56 in the ground state at $T = 0$, $P = 0$).

The solution for N^ϕ has a leading term $N^\phi(r,\ \theta) \sim -2J/r^3$ for $r \to +\infty$ (similar to the slow rotation approximation from Appendix D). Function $J(r,\ \theta)$ can be identified with the angular momentum of the star:

$$J := -\int_{\Sigma_t} \mathcal{T}_{\mu\nu} n^\mu e^\nu_\phi \sqrt{h} \mathrm{d}x^3 = \int \frac{A^6}{B} J_\phi r^2 \sin\theta \mathrm{d}r\mathrm{d}\theta\mathrm{d}\phi \ . \tag{2.24}$$

Yet another physical quantity is the equatorial (circumferential) radius $R_{\rm eq}$ as measured by the Eulerian observer. If stems directly from the metric, Eq. (2.7), as a function of r coordinate at the equator:

$$R_{\rm eq} = A^2(r_{\rm eq},\ \pi/2) B(r_{\rm eq},\ \pi/2) r_{\rm eq} \ , \tag{2.25}$$

where $r_{\rm eq}$ is the coordinate radius (determined from the condition of e.g. vanishing enthalpy on the surface).

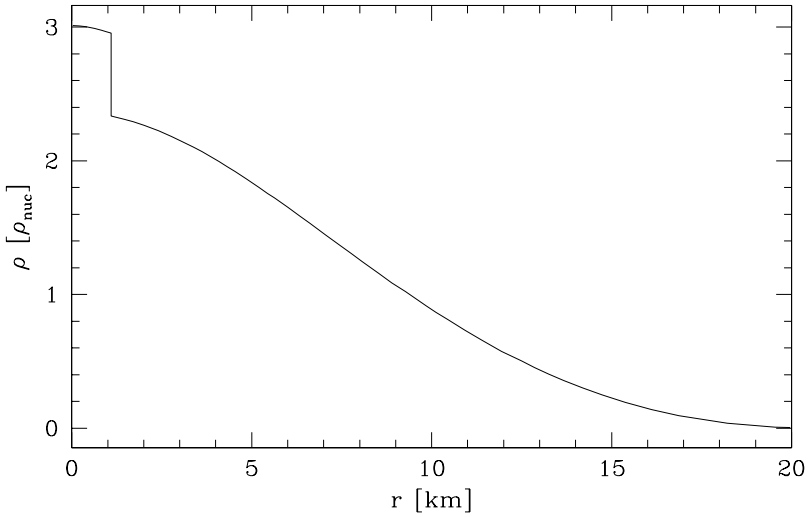

Figure 2.3: The density profile (in units of $\rho_{\rm nuc}$) in the equatorial plane of a star rotating with the Keplerian velocity, the same as in Fig. 2.2. The EOS exhibits a constant-pressure phase transition (new dense phase is pictured as the small nucleus domain in the center) with the baryon density jump of $n_{\rm S}/n_{\rm N} = 1.25$. Due to multi-domain structure of codes, no spurious oscillations are present at the boundary of phases.

Numerical implementation of above equations is based on multi-domain spectral methods and is described in detail by Bonazzola et al. (1993) and Bonazzola et al. (1999a). Eqs. (2.10) have all the form of pseudo-Poisson equations, with the "sources terms" (gravitational mass-energies and/or radiation) on the right-hand side. Additional, fifth equation, the first integral of motion – Eq. (2.20) – is an algebraic equation in the case of rigid rotation. This set of equations is then solved by the use of iterative procedure. Most of the sources terms (right-hand sides of Eqs. 2.20) fill all the available space, from $r = 0$ to $r = +\infty$, the numerical technique of solving the partial differential equations with e.g. discontinuous source terms is as follows: the space is divided into several domains inside the star (it is possible to have many of them in order to precisely reconstruct the internal structure), and in the space for $r > R$. Last computational domain extends to infinity, and in this region compactified radial coordinate $\sim 1/r$ is introduced. At each step of iteration matching conditions across the domain boundaries and at infinity are fulfilled to guarantee the uniqueness of the solution.

On Fig. 2.2 and Fig. 2.3 I present a sample calculation of a star rotating with the Keplerian (mass-shedding) velocity. Due to the multi-domain structure

of the code it is possible to call a different EOS in each domain (in this case there are two domains with the polytropic $\gamma = 2$ EOSs in each of them). In this way the so-called Gibbs phenomenon (spurious oscillations) is completely eliminated from the series expansions on the jumpy profiles and the surface. As we see, it is also possible to deal with very small cores of dense phases without losing the accuracy spectral methods provide. The code will be used to obtain rotating equilibrium configurations of compact stars with phase transition EOSs in Chapter 4.

2.2 Binary neutron stars systems

Numerical computations of close binary NS systems presented in Chapter 5 rely on several assumptions. The orbital evolution is approximated by a sequence of equilibrium states with decreasing separation, in order to simulate the reaction of the system to the emission of gravitational waves. We will assume the quasi-equilibrium state (helical Killing vector approximation) with the irrotational flow of the fluid and a conformally flat spatial 3-metric, the use of which is often called the Isenberg-Wilson-Mathews (IWM) approximation.

Quasi-equilibrium approximation is well justified before the innermost stable orbit, because the gravitational radiation tends to circularize the orbits, and the time evolution of orbital period is much longer than the period itself. As far as second assumption is concerned, an irrotational state corresponds to the situation where the evolution of gravitational-driven radiation is to rapid for the viscous forces to synchronize the spin of each NS with the orbit period. In numerical scheme presented here it is also possible to simulate the corrotational i.e. synchronized systems, similar to the Earth-Moon configuration (the case which is actually simpler from a numerical point of view, because one needs not to solve the equation for the irrotational flow of matter inside NSs). Physical situation is more similar to the irrotational case – if the initial periods of NSs are not $\sim$milliseconds, close binary systems are better approximated by a zero vorticity (irrotational) state, because the viscosity is rather negligible, and we may assume that the fluid circulation with respect to inertial frame is conserved.

The numerical code which will be used in computations has been successfully applied in calculating the final phase of the inspiral of binary NSs with polytropic equation of state (Taniguchi et al., 2001; Taniguchi and Gourgoulhon, 2002b,a). The complete description of the resulting general relativistic equations, the whole algorithm, as well numerous tests of the code (for polytropes) were done by Bonazzola et al. (1997) and Gourgoulhon et al. (2001). Additional tests were also performed by Taniguchi and Gourgoulhon (2003) (Sect. III). Here I will present a brief outline to the equations which will be solved.

For a perfect fluid at zero temperature, we will adopt the stress-energy tensor of the form of Eq. (2.2). According to Lichnerowicz (1967), the main equation, namely the momentum-energy conservation equation $\nabla \mathcal{T} = 0$ can be written as

$$\mathbf{u}(\nabla \wedge \mathbf{w}) = 0 \quad \text{and} \quad \nabla(n\mathbf{u}) = 0 \ , \tag{2.26}$$

where $\mathbf{u}$ is the fluid 4-velocity and $\mathbf{w}$ the momentum density 1-form $\mathbf{w} = h\mathbf{u}$, h being the fluid specific enthalpy, Eq. (A.8). Signature $\nabla \wedge \mathbf{w}$ denotes the exterior derivative of $\mathbf{w}$. A potential flow

$$\mathbf{w} = \nabla\Psi \tag{2.27}$$

is a solution of the equations of motion, Eq. (2.26), where Ψ is the scalar potential. As was said previously, it corresponds to the physical situation reached by a binary system of NSs. It will also be assumed that there exists a helicoidal symmetry (Bonazzola et al., 1997) – let us denote by $\mathbf{l}$ the associated Killing vector. It implies Lie derivative $\mathcal{L}_{\mathbf{l}}\mathbf{w} = 0$ and, from Cartan's identity, $\mathcal{L}_{\mathbf{l}}\mathbf{w} = \mathbf{l}\nabla \wedge \mathbf{w} + \nabla(\mathbf{lw})$; the potential form Eq. (2.27) leads to the following first integral of motion ($\nabla \wedge \nabla\Psi \equiv 0 \rightarrow \nabla(\mathbf{lw}) = 0$):

$$\mathbf{lw} = const., \tag{2.28}$$

as pointed out by Carter (1979). Note that this result is not merely the relativistic generalization of the Bernoulli theorem, which states that $\mathbf{lw}$ is constant along each single streamline and which comes directly from the existence of a Killing vector without any hypothesis on the flow. One needs an additional assumption – we have assumed the potential character (irrotationality) of the flow.

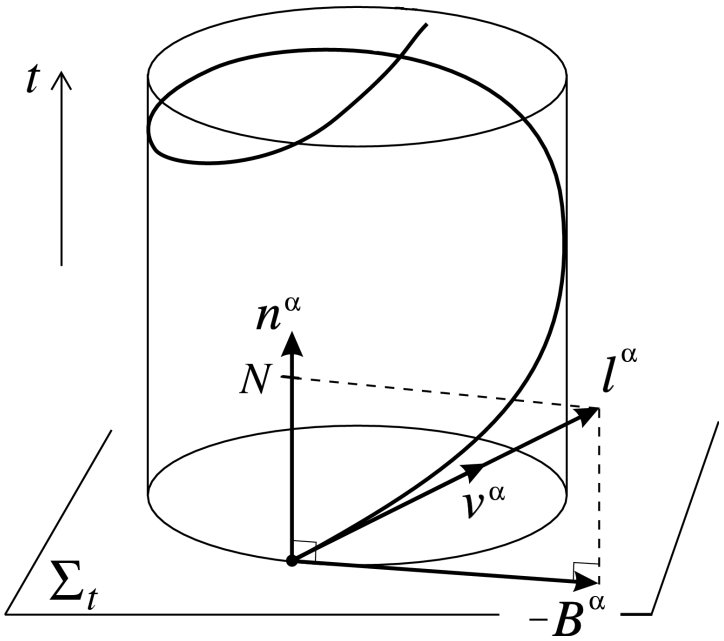

Figure 2.4: Spacetime foliation Σ_t, helicoidal Killing vector l^α and its trajectory – worldline of the co-orbiting observer (4-velocity: v^α). The rotating-coordinate shift vector B^α and the unit future-directed vector n^α, normal to the spacelike hypersurface Σ_t, corresponding to the 3+1 approximation are also shown (as presented by Bonazzola et al. 1997)

The Isenberg-Wilson-Mathews (IWM) approximation for the form of the metric is then adopted. This approximation consists of taking a conformally flat 3-metric, $\mathbf{h} = A^2\boldsymbol{\eta}$, so that the full spacetime metric is given by

$$g_{\alpha\beta}\mathrm{d}x^\alpha\mathrm{d}x^\beta = -(N^2 - B_iB^i)\mathrm{d}t^2 - 2B_i\mathrm{d}t\,\mathrm{d}x^i + A^2\eta_{ij}\mathrm{d}x^i\,\mathrm{d}x^j\ , \qquad (2.29)$$

where $\boldsymbol{\eta}$ is the flat space metric tensor, and A is the conformal factor (the condition of asymptotic flatness is then $\mathbf{h} \to \boldsymbol{\eta}$ at spatial infinity). The field equations reduce now to the form of Wilson and Mathews (1995); Wilson et al. (1996) for lapse N, shift vector $\mathbf{B}$ and the conformal factor A. As a gauge condition, maximal slicing is chosen.

The helicoidal Killing vector $\mathbf{l}$ (Fig. 2.4) satisfies

$$\mathbf{l} = \frac{\partial}{\partial\tau} + \Omega\frac{\partial}{\partial\phi}\ , \qquad (2.30)$$

by introducing the orbital angular frequency Ω, following Bonazzola et al. (1997) – τ and ϕ are respectively the time and azimuthal coordinate associated with the asymptotic inertial observer at rest with respect to the system. The non-rotating coordinates shift vector $\mathbf{N}$ is defined as $\mathbf{B} = \mathbf{N} - \Omega\partial/\partial\phi$.

Fluid motion is determined by the scalar potential Ψ, Eq. (2.27). The equation for Ψ can be derived from the baryon number conservation, Eq. (2.26). We have

$$\frac{n_{\rm b}}{h}\nabla\nabla\Psi + (\nabla\Psi)\nabla\left(\frac{n_{\rm b}}{h}\right) = 0\ . \tag{2.31}$$

Within the 3+1 formalism and with taking into account the helicoidal symmetry, this equation reads

$$n_{\rm b}D_iD^i\Psi + D^in_{\rm b}D_i\Psi = -\frac{h\Gamma_{\rm n}}{N}B^iD_in_{\rm b} + Kn_{\rm b}h\Gamma_{\rm n} +$$

$$+\ n_{\rm b}\left\{\left(D^i\Psi + \frac{h\Gamma_{\rm n}}{N}B^i\right)D_i\ln h - D^i\Psi D_i\ln N - \frac{B^i}{N}D_i(h\Gamma_{\rm n})\right\}, \tag{2.32}$$

where D_i is the covariant derivative with respect to the spatial 3-metric, K is the trace of the extrinsic curvature tensor, shift vector $\mathbf{B}$ and lapse N relate to the orthogonal decomposition of the helicoidal Killing vector $\mathbf{l} = N\mathbf{n} - \mathbf{B}$, $\mathbf{n}$ equals the unit future directed normal vector to the hypersurface $t = const.$ $\Gamma_{\rm n} = -\mathbf{nu}$ denotes the Lorentz factor of the fluid with respect to the Eulerian observer whose 4-velocity is $\mathbf{n}$ (Teukolsky, 1998; Shibata, 1998).

The gravitational field equations derived within the 3+1 formalism from the Hamiltonian constraint, momentum constraint and trace of the spatial part of the Einstein equation (Wilson et al., 1996; Baumgarte et al., 1998) are written, by additional introducing $\nu = \ln N$ and $\beta = \ln(AN)$ as

$$\underline{\Delta}\beta = 4\pi A^2S + \frac{3}{4}A^2K_{ij}K^{ij} - \frac{1}{2}\left(\overline{\nabla}_i\nu\overline{\nabla}^i\nu + \overline{\nabla}_i\beta\overline{\nabla}^i\beta\right)\ , \tag{2.33}$$

$$\underline{\Delta}\nu = 4\pi A^2(E+S) + A^2K_{ij}K^{ij} - \overline{\nabla}_i\nu\overline{\nabla}^i\beta\ , \tag{2.34}$$

$$\underline{\Delta}N^i + \frac{1}{3}\overline{\nabla}^i\left(\overline{\nabla}_jN^j\right) = -16\pi NA^2(E+P)U^i + 2NA^2K^{ij}\overline{\nabla}_j(3\beta - 4\nu)\ , \tag{2.35}$$

where $\overline{\nabla}$ is the covariant derivative associated with the flat 3-metric $\boldsymbol{\eta}$ and $\underline{\Delta} = \overline{\nabla}^i\overline{\nabla}_i$ is the corresponding Laplacian, $\overline{\nabla}^i = \eta^{ij}\overline{\nabla}_j$. $E = \Gamma_{\rm n}^2(\mathcal{E}+P) - P$, $S = 3P + (E+P)U_iU^i$ and $U^i = D^i\Psi/(h\Gamma_{\rm n})$ are the fluid energy density, trace of the stress tensor and fluid 3-velocity measured by the Eulerian observer, respectively. $\Gamma_{\rm n}$ can be computed according to the following equation:

$$\Gamma_{\rm n} = \frac{1}{\sqrt{1-U_iU^i}} = \left[1 + \frac{1}{A^2h^2}\overline{\nabla}_i\Psi\,\overline{\nabla}^i\Psi\right]^{1/2}. \tag{2.36}$$

The extrinsic curvature tensor results from the Killing equation for $\mathbf{l}$

$$K^{ij} = -\frac{1}{2A^2N}\left\{\overline{\nabla}^i N^j + \overline{\nabla}^j N^i - \frac{2}{3}\eta^{ij}\overline{\nabla}_k N^k\right\} , \tag{2.37}$$

The matter distribution is determined by the first integral of motion, Eq. (2.28). Taking its logarithm leads to

$$H + \nu + \frac{1}{2}\ln\left(1 - A^2\eta_{ij}\frac{B^iB^j}{N^2}\right) + \ln\Gamma = const., \tag{2.38}$$

where, according to Eq. (A.9), $H = \ln h$ is the log-enthalpy and Γ is the fluid Lorentz factor with respect to the co-orbiting observer

$$\Gamma = \Gamma_{\rm n}\left(1 + A^2\eta_{ij}\frac{B^i}{N}U^j\right)\left(1 - A^2\eta_{ij}\frac{B^iB^j}{N^2}\right)^{-1/2} . \tag{2.39}$$

Eq. (2.38), just like Eq. (2.20) in the case of axisymmetric rotating star, is the relativistic analogue of Bernoulli theorem for stationary flow of ideal fluid in the presence of gravitational field.

Introducing

$$\zeta = \frac{{\rm d}\ln H}{{\rm d}\ln n_{\rm b}} , \tag{2.40}$$

the fluid velocity potential equation, Eq. (2.32) can be written as

$$\zeta H\underline{\Delta}\Psi + \overline{\nabla}^i H\overline{\nabla}_i\Psi = -A^2h\Gamma_{\rm n}\frac{B^i}{N}\overline{\nabla}_i H +$$

$$+ \zeta H\left\{\left(\overline{\nabla}^i\Psi + A^2h\Gamma_{\rm n}\frac{B^i}{N}\right)\overline{\nabla}_i H - \overline{\nabla}^i\Psi\overline{\nabla}_i\beta - A^2\frac{B^i}{N}\overline{\nabla}_i(h\Gamma_{\rm n})\right\} . \tag{2.41}$$

As was shown by Gourgoulhon et al. (2001), Eq. (2.41) can be further improved, because the potential Ψ is dominated by a translational part. Therefore, for each star

$$\Psi = \Psi_0 + \eta_{ij}W_0^i x^j , \tag{2.42}$$

where W_0^i is the constant translational velocity field defined as the central value of

$$W^i = -A^2h\Gamma_{\rm n}\frac{B^i}{N} . \tag{2.43}$$

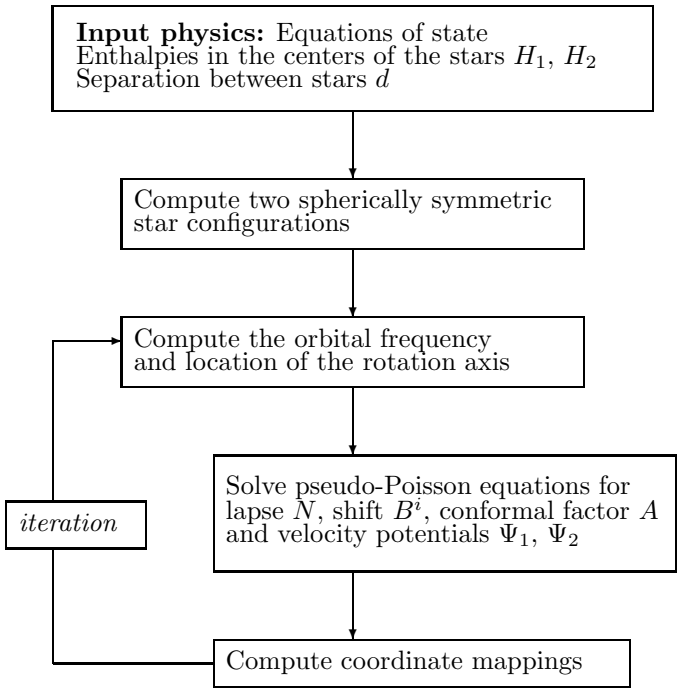

Figure 2.5: Block diagram of a numerical run in the case of binary NSs.

Eq. (2.41) can be finally written as

$$\zeta H \underline{\Delta} \Psi_0 + \left((1-\zeta H) \overline{\nabla}^i H + \zeta H \overline{\nabla}^i \beta \right) \overline{\nabla}_i \Psi_0 \; =$$

$$= \; (W^i - W_0^i) \overline{\nabla}_i H + \zeta H \left(W_0^i \overline{\nabla}_i (H - \beta) + \frac{W^i}{\Gamma_{\rm n}} \overline{\nabla}_i \Gamma_{\rm n} \right) . \qquad (2.44)$$

The right-hand side of Eq. (2.44) is much smaller than the right-hand side of Eq. (2.41) which means that now the problem is better-posed from a numerical point of view. Eqs. (2.33–2.35) and Eq. (2.44) consist of a system of non-linear pseudo-Poisson equations. Because of the non-linear character of equations, an iterative procedure based on a multi-domain spectral methods (Bonazzola et al., 1999b, 1998) is used to obtain the solution, see Fig. 2.5 for the scheme of computational run. The stars (Fig. 2.6) are placed in non-rotating frame in Cartesian coordinates at fixed distance d between their centers. In addition, each star has its own spherical system of coordinates. At the beginning of the computation two spherically symmetric models are obtained in order to get initial conditions. Then the orbital frequency is computed, and the location of rotational axis is established (for starting the calculations post-Newtonian value of the frequency is provided). Elliptic Eqs. (2.33–2.35) and Eq. (2.44)

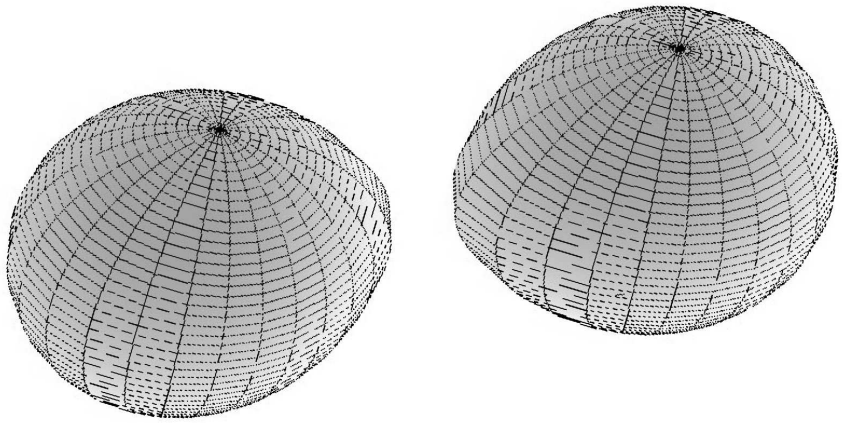

Figure 2.6: A binary system of neutron stars on its last orbit before the merger – similar configurations are computed using methods described in this section (figure by Taniguchi et al. 2001).

are solved iteratively at each step of the main loop. At the end of the main iteration the coordinates used for description of stars interior and surface are updated, and prepared for the next step. Numerical implementation of above equations are presented by Bonazzola et al. (1999a) and Gourgoulhon et al. (2001) where one can find detailed description of the initial conditions, approximations, as well as numerous tests.

Having in mind subsequent calculations of binary NS systems I will recall the definition of the so-called Arnowitt-Deser-Misner (ADM) mass which denotes the total mass-energy of the system on a slice hypersurface Σ_t of the spacetime:

$$\begin{aligned} M_{\rm ADM} &= \frac{1}{16\pi}\oint_\infty \left[\eta^{ik}\eta^{jl}(\overline{\nabla}_j h_{kl} - \overline{\nabla}_k h_{jl})\right] {\rm d}S_i = \\ &= \frac{1}{16\pi}\oint_\infty \left[\overline{\nabla}^j h_{ij} - \overline{\nabla}_i\left(\eta^{kl}h_{kl}\right)\right] {\rm d}S^i \ , \end{aligned} \tag{2.45}$$

where, as we remember h_{ij} is the metric induced on Σ_t, η_{ij} is the flat metric on Σ_t and $\overline{\nabla}_i$ is the covariant derivative associated with η_{ij}. The integral is evaluated on a sphere at spatial infinity. In the case considered here $h_{ij} = A^2\eta_{ij}$, the surface integral can be converted into a volume integral over the whole hypersurface Σ_t by means of Gauss-Ostrogradsky theorem:

$$M_{\rm ADM} = \int_{\Sigma_t} A^{5/2}\left(E + \frac{1}{16\pi}K_{ij}K^{ij}\right) {\rm d}^3x \ , \tag{2.46}$$

The changes of the $M_{\rm ADM}$ mass will be used in Chapter 5 to monitor the gravitational wave energy loss during the inspiral phase of NS binary system.

Previous such computations were mainly done using the polytropic EOSs (Gourgoulhon et al., 2001; Taniguchi and Gourgoulhon, 2002a, 2003; Bonazzola et al., 1999a; Marronetti et al., 1999; Uryū and Eriguchi, 2000; Uryū et al., 2000). The differences with respect to the realistic EOSs stem from the fact that realistic EOS are usually given in a tabulated form and a certain thermodynamic coefficient ζ (Eq. 2.40), required in the computation of the velocity potential of the irrotational fluid flow (Eq. 2.44), is not given explicitly by the tabulated EOS. The approximation of the perfect fluid for the form of the stress-energy tensor will be adopted, the matter is well represented by the zero-temperature EOS and the Gibbs-Duhem identity provided by Eq. (A.12) will be used. I will rewrite the Eq. (2.40) as

$$\zeta = \frac{\mathrm{d}(\ln H)}{\mathrm{d}(\ln n_{\rm b})} = \frac{\mathrm{d}(\ln H)}{\mathrm{d}(\ln P)} \frac{\mathrm{d}(\ln P)}{\mathrm{d}(\ln n_{\rm b})} = \gamma \times \frac{\mathrm{d}(\ln H)}{\mathrm{d}(\ln P)} \ , \tag{2.47}$$

where $\gamma = \mathrm{d}\ln P / \mathrm{d}\ln n_{\rm b}$ is the adiabatic index – it determines the response to the compression or decompression of matter. As we remember, the log-enthalpy H is related to the specific enthalpy of the fluid h by Eq. (A.9). From Eq. (A.12) we obtain the *exact* thermodynamical relation $\mathrm{d}(\ln P)/\mathrm{d}(\ln H) = (\mathcal{E} + P)H/P$.

In actual calculations, two methods were used to obtain the adiabatic index, which according to Eq. (2.47) should be available in order to obtain the value of ζ. One can use the analytical formulae for the adiabatic index, using tabulated values of γ (the drawback of this approach is that one should prepare the tables of γ values before actual calculations). The second method is more general – adiabatic index is obtained directly from the tabulated EOS by taking the derivative of the second order polynomial going through three consecutive (P, $n_{\rm b}$) tabulated EOS points. The value of the $\mathrm{d}P/\mathrm{d}n_{\rm b}$ multiplied by the $n_{\rm b}/P$ is evaluated at the middle point, and the resulting discrete values of γ are interpolated, as other quantities from the tabulated EOS (see Sect. A.1).

Both methods proved to be very robust. Second method was tested against the SLy EOS (Douchin and Haensel, 2000), for which precise values of the adiabatic index obtained from the microscopic considerations were available.

Calculations of the parameter ζ constituted additional consistency check in the process of obtaining final results. In Chapter 5 the first calculations of a true *realistic EOS inspiral* will be presented. From this point of view it was essential to be sure that the EOS is treated properly, especially in the crust part. The crust part of the EOS influences the behavior of stars when they are deformed by tidal forces of the gravitational field of the companion NS.

Chapter 3

Nucleation-induced stellar core-quakes

The results contained in this chapter are an extension of the linear response theory developed in the Newtonian regime by Schaeffer et al. (1983) and then further developed and applied in General Relativity by Haensel et al. (1986b) and Zdunik et al. (1987). This method is based on expressing the changes in a star's density profile, due to the appearance of a small core, as the combination of two independent solutions of linearly perturbed equations of stellar structure. It was employed by P. Haensel, J. L. Zdunik and R. Schaeffer to the case of first order phase transitions between *pure* phases – corresponding to the EOS with a density-jump constant-pressure phase transition. As advocated in Sect. 1.1, the requirement of *local* electric charge conservation leads to a constant-pressure phase transition ("Maxwell construction" phase transition), which, in the presence of a gravitational field, leads to a density jump at the phase boundary. However, revision of the local charge neutrality in favor of the more physical *global* (macroscopic) electric charge neutrality condition results in the more recently proposed scenario of a *structured* mixed phase transition (Glendenning, 1991, 1992).

In subsequent sections, I will justify the validity of the linear response theory in the case of a structured mixed phase transition. I will show that the formulae which describe the changes of the global stellar parameters (the radius R, the moment of inertia I and the mass-energy $E = Mc^2$) are proportional to specific powers of the radius of a newly-born core under the transition from a metastable core to a stable core of mixed phase – this feature emerges naturally from the linear response theory. For simplicity, the approach presented here

neglects the rotation of the star. Moreover, since the EOS of the mixed phase is unknown, it will be approximated by a parametric polytropic EOS; this simplifying assumption will be justified with the use of a sample of realistic mixed-phase EOSs.

From the astrophysical point of view, there are several ways to successfully create a mixed-phase core inside a NS. First of all, the matter in the center of the star can be compressed during the epoch of the pulsar's spin-down. Rotation affects the pressure distribution in a manner approximately proportional to the spin frequency squared, Ω^2. The rate of the quasi-static increase of the central pressure is thus $\dot{P}_{\rm c} \propto -\dot{\Omega}\Omega$. If the matter in the N phase is over-compressed above some critical value (see Sect. 3.4 for the definition of over-compression), the nucleation of a new phase takes place – when the temperature inside the star is lower than 10^9 K the nucleation occurs by quantum fluctuations in the over-compressed core. Nucleation induces collapse of the central core, matter heating and energy release. We should also expect a flow of matter, the treatment of which is, however, not a subject of this study.

Similarly, a binary system with an accreting NS is a good candidate for observations of core phase transitions; the problem of accreting NSs with pion degree of freedom was studied in the past by Miralda-Escudé et al. (1990). The central pressure increases due to accreted material collecting on the surface of the star – one then has the central pressure increase $\dot{P}_{\rm c} \propto \dot{M}$. As in the case of a spinning-down pulsar, the temperature is too low to induce thermal fluctuations ($T < 10^9$ K), so the new phase will be created by quantum fluctuations. Further development of a newly-born core happens as in the previous case: the pressure deficit triggers core collapse, accompanied by matter heating and flow; finally, mixed-phase core forms.

Another scenario relates to NS birth. Proto-NSs form in the gravitational collapse of a massive stellar core. During the first few seconds the fraction of leptons inside the star is high – this is a direct result of neutrino trapping. As a consequence, the EOS of matter is relatively stiff, compared to the EOS of a "normal", mature NS. Gradual loss of neutrinos and deleptonization of matter softens the EOS in the core which means that the matter inside is compressed. The temperature of the core is high enough to enter the regime of thermal fluctuations, $T \sim 10^{11}$ K – the new phase nucleates due to those

fluctuations. In all those cases the new phase appears as an S phase fluctuation in the meta-stable N phase medium. When the system can no longer be in the meta-stable state, typically due to over-compression, it relaxes to a stable state of mixed N and S phases.

The present chapter is divided into several sections: in Sect. 3.1 a brief description of the theoretical background and methods used is provided. Sects. 3.2 and 3.3 contain the results of numerical calculations for polytropic and realistic EOSs, respectively. Sect. 3.4 includes final conclusions and remarks.

3.1 Linear response theory

In this section I will outline the theoretical background related to a star's response to the appearance of a small core. The method benefits from the fact that the creation of a condensed core induces a change in the star's density profile. If the size of the core is small, the aforementioned changes can be described within the linear approximation. In this approximation the properties of star's response depend on the EOS of matter in the N phase – the core properties are parametrized only by its radius (Haensel et al., 1986b; Zdunik et al., 1987), as the combination of two independent solutions of the linearly perturbed equations of stellar structure. In other words, the presence of a denser phase in the core changes the boundary condition at the phase transition pressure $P_{\rm N}^{(\rm m)}$ (see Fig. 3.1 and Fig. 3.2). For the central pressure $P_{\rm c} = P_{\rm crit}$ the nucleation of the S phase (in the super-compressed meta-stable core of radius $r_{\rm N}$ created in the center of the corresponding star configuration C) triggers the transition and formation of the mixed-phase core of radius $r_{\rm m}$ in a new mixed-phase configuration C*. Global baryon number is conserved during the transition.

Because of the increase of *mean* density, the mixed phase is softer than the pure one in realistic EOSs – the mixed phase arises partly via conversion of a less dense N phase into a denser S phase, and so it requires less pressure than in the case of a pure N phase. Therefore, the appearance of a new phase is associated with a substantial drop of the adiabatic index of matter, from $\gamma_{\rm N}$ in the N phase to $\gamma_{\rm m}$ in the mixed phase ($\gamma_{\rm m} < \gamma_{\rm N}$).

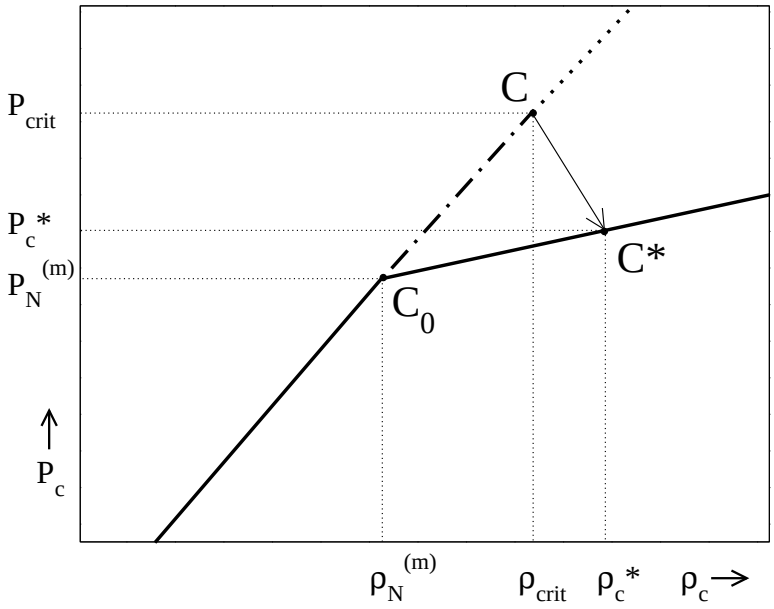

Figure 3.1: Schematic plot of central pressure $P_{\rm c}$ versus central matter density $\rho_{\rm c}$ for configurations based on a pure N phase EOS and an EOS with a mixed-phase segment. The solid line denotes stable states, the dashed line – the states which are meta-stable with respect to the transition to a mixed-phase state. For a critical central density $\rho_{\rm crit}$ the S phase nucleates in the super-compressed core of configuration C, which results in the transition into a stable configuration C* with a mixed-phase core and a central density $\rho_{\rm c}^*$. Configurations C and C* have the same baryon number $A_{\rm B}$.

Similarly to the case of a phase transition between two pure phases, where the leading term in the perturbation of the boundary condition at the edge of a new phase results from the mass excess due to the density jump (as shown by, e.g., Zdunik et al. 1987), in the present case of a mixed phase transition the mass excess results from the lower stiffness and higher density of the new phase as compared to their values in the N phase. As far as global properties of stars are concerned, the hydrostatic stars' equilibria corresponding to EOSs with and without the phase transition must be compared (Fig. 3.2). EOSs are constructed in a fashion similar to that presented in Sect. B.2. The models are non-rotating, spherically symmetric solutions of Einstein's equations, usually called Tolman-Oppenheimer-Volkoff (TOV) equations (Tolman, 1939; Oppenheimer and Volkoff, 1939) – see Appendix C for the details of the TOV equation, and Appendix D for the method of calculating the moment of inertia I. Hydrostatic solutions are labeled by their central density $\rho_{\rm c}$. The configurations based on the two EOSs are identical up to $\rho_{\rm c} = \rho_{\rm N}^{\rm (m)}$; the configuration with such central density will be denoted by $\rm C_0$ and will be called

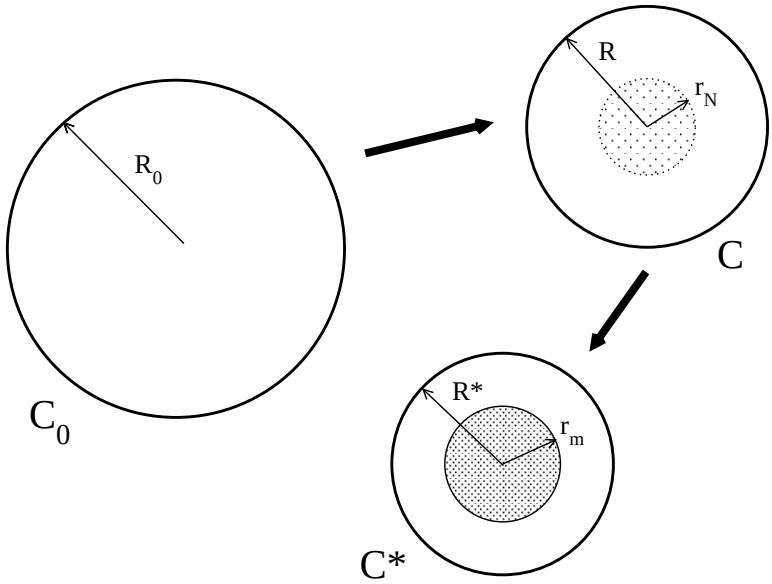

Figure 3.2: Transition from an one-phase configuration C with a meta-stable core of radius $r_{\rm N}$ to a two-phase configuration C* with a mixed-phase core with a radius $r_{\rm m}$. Global numbers of baryons in both configurations are the same.

a "reference configuration".

As will be advocated below, the leading stellar parameter changes due to the phase transition are proportional to the fifth power (for the radius R and moment of inertia I) and seventh power (for gravitational mass-energy $E = Mc^2$) of the mixed-core radius $r_{\rm m}$ (for constant-pressure pure phases transitions, studied by Zdunik et al. (1987) the powers of the pure phase core radius $r_{\rm S}$ were equal to three and five, respectively). During the calculations, we will assume constant $\gamma_{\rm m}$ in the mixed-phase by replacing the mixed-phase segment of the EOS for densities greater than $n_{\rm N}^{\rm (m)} \equiv n_{\rm m}$ by a polytropic EOS with $\gamma_{\rm m} < \gamma_{\rm N}$. This is equivalent to neglecting the density (radius) dependence on γ in the mixed-phase core. Such treatment does not change the leading terms of the small $r_{\rm m}$ expansions and, as shown in Figs. 3.3, this approximation is excellent for a not too large mixed-phase core. In principle, the inclusion of $r_{\rm m}$ dependent $\gamma_{\rm m}$ will contribute to higher-order terms, but as pictured on Figs. 3.3 the contribution is small in the case of realistic EOSs.

The examples presented here are given by Glendenning (1997, Table 9.1) and Pons et al. (2000) – for other examples, see e.g. Glendenning and Schaffner-Bielich (1998, 1999). In all those cases, the logarithm of pressure depends

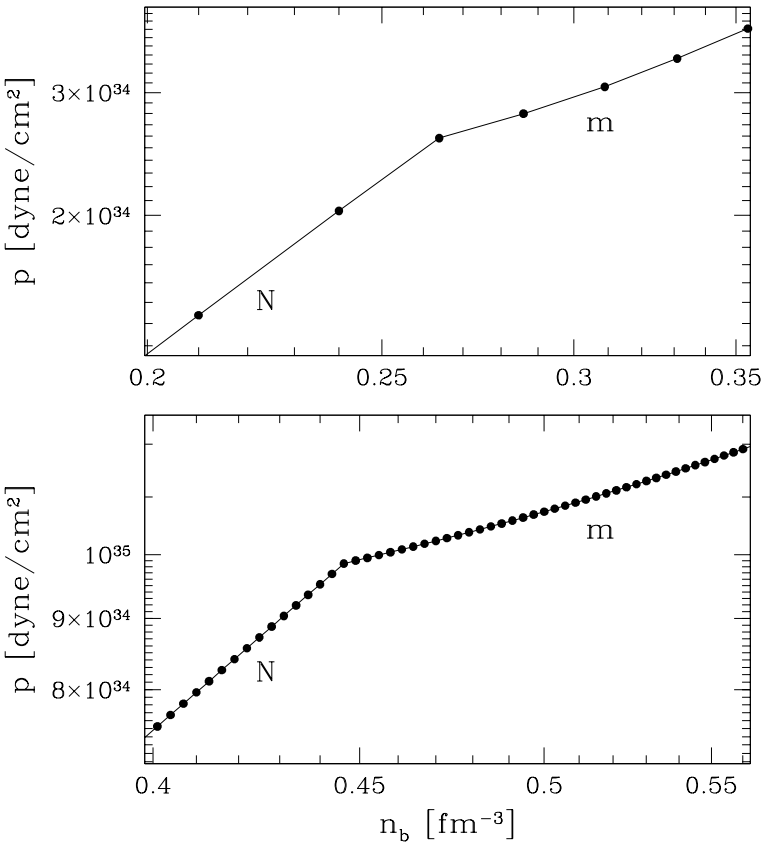

Figure 3.3: The logarithm of pressure P as a function of logarithm of baryon density $n_{\rm b}$ for a sample mixed-phase EOS. Dots correspond to the tabulated points. The sudden drop of $\gamma = {\rm d}\ln P/{\rm d}\ln n_{\rm b}$ at the N-m interface is clearly seen. Note that the mixed-phase segment in the $\log(n_{\rm b}) - \log P$ plane can be well approximated by a straight line. This means, that within the considered density interval, the polytropic approximation for the mixed phase is good. Upper panel: quark matter – baryon matter transition from Glendenning (1997, Table 9.1). Lower panel: similar transition for the GM-GS-120 model with kaon optical potential $U_K^{\rm lin} = -120$ MeV; kaon-condensate—baryon matter transition obtained by Pons et al. (2000).

linearly on the logarithm of baryon density near the boundary of phases; it clearly indicates that the polytropic approximation of mixed phase is valid in the small mixed-phase core regime. The power expansion of the small core radius $r_{\rm m}$ will therefore be used to describe the changes in stellar parameters. When the central density exceeds $\rho_{\rm N}^{\rm (m)}$ the C and C* models begin to differ due to the appearance of a softer mixed-phase core for configurations corresponding to the mixed-phase EOS. For a fixed baryon number $A_{\rm B}$, greater than the baryon number of the reference configuration $A_{\rm B}({\rm C}_0)$, one compares the global parameters – the mass-energy $E = Mc^2$, radius R and the moment of inertia

I. Their difference corresponds to the changes implied by the phase transition in the stellar core.

I will now compare the expressions corresponding to the case when the new core consists of a pure S phase, considered by (Zdunik et al., 1987; Haensel et al., 1986b), and the case of a mixed-phase core.

We recall that the TOV equation (Appendix C) is the familiar Newtonian hydrostatic balance equation

$$\frac{\mathrm{d}P}{\mathrm{d}r} = -\frac{Gm\rho}{r^2} \ , \tag{3.1}$$

modified by relativistic terms. For simplicity, we will currently focus on the Newtonian example; the relativistic terms do not qualitatively modify the analysis – they will reappear in the final expressions.

For a pure S phase core, the density jump $\rho_{\rm N} \to \rho_{\rm S}$ leads to the following core-mass excess (with respect to the pure N phase configuration),

$$\delta m_{\rm core} = \frac{4}{3}\pi(\rho_{\rm S} - \rho_{\rm N})r_{\rm S}^3 + \mathcal{O}(r_{\rm S}^5) \ . \tag{3.2}$$

The powers $r_{\rm S}^l$, for $l \geqslant 5$ have been neglected.

In the case of a mixed-phase core there is no density jump at the core boundary (radius $r_{\rm m}$). Let the density and pressure at the core boundary $r_{\rm m}$ be equal $\rho_{\rm N}^{\rm (m)} \equiv \rho_{\rm m}$ and $P_{\rm N}^{\rm (m)} \equiv P_{\rm m}$ according to Fig. 3.1. The mass excess in the mixed-phase case results from the difference in stiffness, i.e. the difference in the adiabatic index of the matter in N phase and mixed phase – the adiabatic index changes from $\gamma_{\rm N}$ on the N-side to a lower value $\gamma_{\rm m}$ on the m-side.

The pressure gradient is related to the density gradient through the sound propagation velocity v by

$$\frac{\mathrm{d}P}{\mathrm{d}r} = v^2\frac{\mathrm{d}\rho}{\mathrm{d}r} \ . \tag{3.3}$$

Therefore the density profile is equal

$$\frac{\mathrm{d}\rho}{\mathrm{d}r} = -\frac{Gm\rho}{r^2v^2} \ . \tag{3.4}$$

We also define two additional parameters

$$\kappa_{\rm N}^2 = 4\pi G\rho_{\rm m}/v_{\rm N}^2 \ , \quad \kappa_{\rm m}^2 = 4\pi G\rho_{\rm m}/v_{\rm m}^2 \ , \tag{3.5}$$

which are related to sound propagation velocities in both phases, $v_{\rm N}$ and $v_{\rm m}$. We will use the fact that that the mass of the mixed-phase core $m_{\rm core}$ can be approximated by

$$m_{\rm core} = \frac{4}{3}\pi r_{\rm m}^3 \rho \ , \tag{3.6}$$

where the density ρ is constant. Integration of Eq. (3.4), along with the recovery of the relativistic parts dropped at the beginning of our considerations, results in the expressions for the density in the meta-stable and mixed-phase core, which are quadratic in r

$$\rho(r) = \rho_{\rm m}\left[1 + \frac{1}{6}\kappa_{\rm N}(1+x)(1+3x)(r_{\rm m}^2 - r^2)\right] + \mathcal{O}(r_{\rm m}^4) \ , \tag{3.7}$$

$$\rho^*(r) = \rho_{\rm m}\left[1 + \frac{1}{6}\kappa_{\rm m}(1+x)(1+3x)(r_{\rm m}^2 - r^2)\right] + \mathcal{O}(r_{\rm m}^4) \ , \tag{3.8}$$

where x is equal $P_{\rm m}/\rho_{\rm m}c^2$, a factor measuring the "relativity" of the EOS. Note also, that the factor $(1+x)(1+3x)$ is the brackets part of TOV equation, Eq. (C.6), in the limit of a small core. The excess of the mixed core mass over the non-perturbed profile is equal

$$\begin{aligned} &\delta m_{\rm core} = m^*_{\rm core} - m_{\rm core} = \textstyle\int^{r_{\rm m}} 4\pi r^2(\rho^*(r) - \rho(r))\mathrm{d}r = \\ &\tfrac{2}{3}\textstyle\int^{r_{\rm m}} \pi r^2 \rho_{\rm m}\left[(r_{\rm m}^2 - r^2)(\kappa_{\rm m}^2 - \kappa_{\rm N}^2)(1+x)(1+3x)\right]\mathrm{d}r \ . \end{aligned} \tag{3.9}$$

As a result one has

$$\delta m_{\rm core} = \frac{4\pi\rho_{\rm m}}{45}(1+x)(1+3x)(\kappa_{\rm m}^2 - \kappa_{\rm N}^2)r_{\rm m}^5 + \mathcal{O}(r_{\rm m}^7) \ . \tag{3.10}$$

Combining the above equation with Eq. (3.5) and taking into account the fact that the sound velocity v is related to the adiabatic index by $v^2 = \gamma P/(\rho + P/c^2)$ we finally obtain

$$\delta m_{\rm core} = \frac{16\pi^2 G\rho_{\rm m}^3}{45\gamma_{\rm N}P_{\rm m}}(1+x)^2(1+3x)(\gamma_{\rm N}/\gamma_{\rm m} - 1)r_{\rm m}^5 + \mathcal{O}(r_{\rm m}^7) \ . \tag{3.11}$$

The fact that in our case the density is continuous suggests that the new phase influences the boundary conditions by the presence of the prefactor $(\gamma_{\rm N}/\gamma_{\rm m} - 1)$, which is qualitatively the same as $(\rho_{\rm S}/\rho_{\rm N} - 1)$ in the case of a density jump from pure N phase to pure S phase (Haensel et al., 1986b; Zdunik et al., 1987). Moreover, the mass excess from Eq. (3.11) compared with Eq. (3.2) indicate

that linear response effects should be proportional to the core radius power greater by two than in the case of the transition between pure phases.

It should be therefore expected that the relative changes in some stellar parameter Q ($Q = R,\ I$ or $E = Mc^2$) contain a prefactor $(\gamma_{\rm N}/\gamma_{\rm m} - 1)$, i.e. we expect the following form of the lowest-order expressions:

$$\delta\bar{Q} \equiv \frac{Q^* - Q}{Q_0} \simeq -\beta_Q(\gamma_{\rm N}/\gamma_{\rm m} - 1)(\bar{r}_{\rm m})^l \ , \tag{3.12}$$

where $\bar{r}_{\rm m} \equiv r_{\rm m}/R_0$, β_Q denotes the response coefficient, $l = 5$ for radius R and moment of inertia I and $l = 7$ for the energy $E = Mc^2$. The coefficients β_Q are functionals of the reference configuration, $\beta_Q = \beta_Q(\mathrm{C}_0)$. I will confirm the validity of the above statements in the next sections by means of numerical calculations.

3.2 Results for polytropic EOSs

In order to test the predictions and to obtain quantitative results I will use the polytropic EOSs for the N and mixed phases. The main reason for choosing parametric EOSs is the precision of numerical calculation and simplicity during the exploration of the parameter space. Discussion of the polytropic EOSs and their application to relativistic stellar structure calculations was presented by e.g. Tooper (1965); see Appendix B for details needed in calculations.

The form of the expressions for the changes of the stellar parameters obtained in the linear approximation was predicted in the previous section, starting from analytical considerations. According to Eq. (3.12), the expressions split into two factors, the first depending on the mixed phase via $\gamma_{\rm m}$ and the second, β_Q, being a functional of the reference configuration C_0. It is a complicated task to write an analytical form of the functional $\beta_Q(\mathrm{C}_0)$ even in the case of polytropic EOS; in order to obtain fairly general results I will therefore restrict myself to the derivation of approximate, but accurate, fitting formulae based on a large set of precise numerical calculations.

The β_I, β_R and β_E coefficients versus the mass of the reference configuration $M_0 \equiv M(\mathrm{C}_0)$ are plotted for an example configuration in Fig. 3.4. Despite the fact that we are now dealing with the parametric polytropic EOSs, the

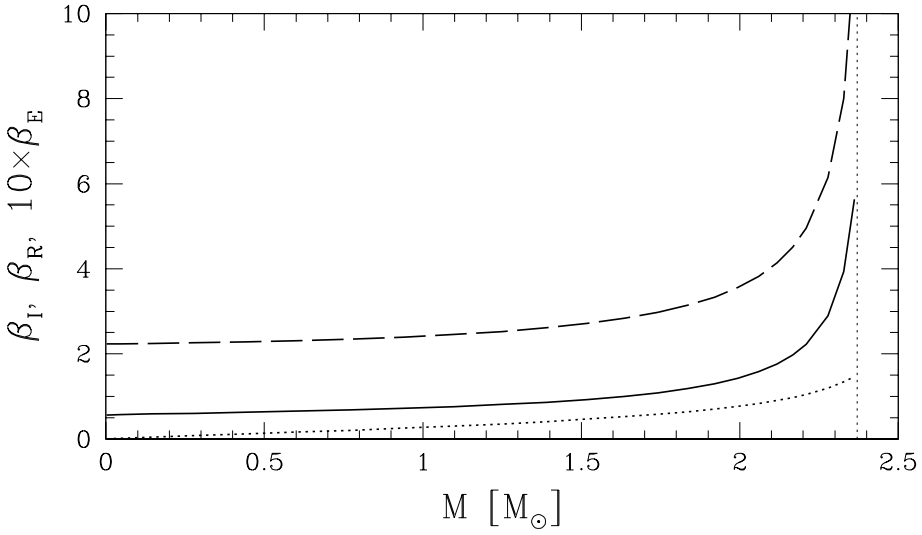

Figure 3.4: The response coefficients β_I, β_R, β_E (dashed, solid and dotted line; the value of β_E was multiplied by a factor of 10) plotted against the stellar mass M_0 for a polytropic EOS, in this example computation $\gamma_{\rm N} = 2.5$, $\gamma_{\rm m} = 1.5$, $K_{\rm N} = 0.025$ (see Appendix B for details). The vertical dotted line denotes the maximal mass of the star, 2.37 $M_\odot$.

whole range of masses of the reference configuration is presented, on account of our ignorance about the density at which the phase transition takes place in realistic EOSs of dense matter. Results were obtained for specific choices of $\gamma_{\rm N}$ and $\gamma_{\rm m}$. In the particular example from Fig. 3.4, the values of $\gamma_{\rm N}$ and $K_{\rm N}$ were chosen in such a way that the EOS of the N phase produced massive compact star models similar to those obtained for realistic stiff EOSs of dense matter. Specifically, this EOS yields $M_{\rm max} = 2.37$ M$_\odot$ and $R_{M_{\rm max}} = 12.52$ km. Note, however, that while the polytrope is a reasonable representation of the EOS of matter with $\rho > 2\rho_{\rm nuc}$, it is completely unrealistic at sub-nuclear densities and for masses much smaller than one solar mass.

One notices the characteristic behavior of β_R and β_I. It turns out that regardless of the fact that one *does not know* the precise density of onset of the new phase, this information is not essential to predict the star's response. The β_R and β_I coefficients are almost constant for a wide range of masses.

The "plateau" values of the coefficients β_I and β_R do not depend on the pressure coefficient $K_{\rm N}$, but only on $\gamma_{\rm N}$. Formulae which accurately describe

those response parameters read

$$\beta_R(\mathrm{C}_0) \simeq \frac{0.015 \times {\gamma_\mathrm{N}}^{9.4}}{({\gamma_\mathrm{N}}^{1.13} - 1)^{8.2}} , \qquad \beta_I(\mathrm{C}_0) \simeq \frac{0.12 \times {\gamma_\mathrm{N}}^{9.1}}{({\gamma_\mathrm{N}}^{1.22} - 1)^{7.5}} , \tag{3.13}$$

for β_R and β_I, respectively.

The case of the mass-energy parameter β_E is different, as Fig. 3.4 shows. Sufficiently far from the maximal mass, $M \lesssim 0.8 M_{\max}$, β_E is proportional to $M(\mathrm{C}_0)$. I have approximated the value of $\beta_E(\mathrm{C}_0)$ as follows:

$$\beta_E(\mathrm{C}_0) \simeq \frac{0.085}{{\gamma_\mathrm{N}}^{2.56} {K_\mathrm{N}}^{0.5(\gamma_\mathrm{N}-1)}} \times \left(\frac{M}{M_\odot}\right) . \tag{3.14}$$

It has to be mentioned that the fitting formulae from Eqs. (3.13–3.14) have been checked against the adiabatic indices in the range 5/3 to 3.5. The fitted expressions are fairly accurate within a wide range of masses, to within few per-cent compared to the exact numerical calculations.

The response coefficients underestimate the magnitude of the linear response for configurations near the maximum allowable mass, $M_{\max}$. The increase of β_Q for $M(\mathrm{C}_0) \longrightarrow M_{\max}$ is due to a "softening" of the reference configuration by the effects of General Relativity (similar to the case presented by Zdunik et al. 1987; Haensel et al. 1986b). Thus the linear approximation and, what follows, the approximate expressions presented above cease to be valid in this region.

It should be also expected, as far as the realistic EOS of the crust is concerned, that the assumption of constant γ in the crust is an over-simplification of the problem. Therefore, the region of small masses (smaller than 0.5 $M_\odot$) is affected by this unrealistic type of crust. In the case of realistic NSs, the behavior of the β_Q coefficients near the star's minimum mass should, due to the softening of matter, be generally similar to those near the maximal mass (such calculations for the case of realistic EOSs are presented in Sect. 3.3)

The fitting formulae for β_Q in the region of validity of the linear-response approximation allow us to compute the change of the interesting stellar parameters for every pair of the parameters γ_N and γ_m. For example, the 1.4 $M_\odot$ C_0 configuration from Fig. 3.4 has radius $R_0 = 15.18$ km and moment of inertia $I_0 = 2.27 \times 10^{45}$ g $\cdot$ cm^2. The response coefficients are then equal $\beta_R = 0.62$, $\beta_I = 2.23$ and $\beta_E = 0.03$. The appearance of $r_\mathrm{m} = 1$ km core

with $\gamma_{\rm m} = 1.5$ adiabatic index inside the $\gamma_{\rm N} = 2.5$ polytrope star changes the radius by $\sim$ 1 cm, a number which can be related to the change of radius during macro-glitches in pulsar timing. A relative change of the moment of inertia ($\Delta I/I = -\Delta\Omega/\Omega$) implies speed-up of the order of 10^{-6}, again a value common to pulsar macro-glitches. The released energy equals 3×10^{44} erg. If the core radius is 4 km (still well described by the linear response theory) the change in radius is 8 m, an impressive number even in view of the size of terrestrial earthquakes. The value of $\Delta\Omega/\Omega$ will be equal approximately 10^{-3}, three orders of magnitude larger than in biggest macro-glitches. Finally, the creation of a 4 km "mixed-phase" core produces $\sim 5 \times 10^{48}$ erg of energy.

For examples of astrophysical phenomena releasing comparable amounts of energy see the last paragraph of Sect. 3.3.

3.3 Results for realistic EOSs

In order to study the linear response theory in the case of realistic EOSs of dense matter and to explore how a realistic NS will respond to the creation of a mixed phase core two EOSs, I have used the recent SLy EOS of Douchin and Haensel (2000) and a slightly older FPS EOS of Pandharipande and Ravenhall (1989). These EOSs assume that the star's central part is built from neutrons, protons, electrons and muons only, and from this point of view they are perfect for simulations of exotic core appearance. The two EOSs were designed to describe both the crust and the core of NS in a unified way, starting from a single effective nuclear Hamiltonian. The important difference between them is in the construction of the inner crust and the existence, in the case of the FPS EOS, of nuclei of non-spherical shapes (bubbles, rods and plates) in the ground state of matter just before the crust-core transition (the nuclei have always spherical shapes in the case of the SLy EOS). In both cases the EOSs of crust and core are connected with a very weak first order density jump phase transition. As will be demonstrated below, the core parts of the EOS ($\rho > \rho_{\rm nuc}$) are also different, e.g. in stiffness. Below I will show how these differences influence the change of stellar parameters.

Similar to calculations from the previous section, a large set of EOSs with a realistic outer part and a "mixed-phase" polytropic segment was constructed

EOS	β_R	β_I	β_E
SLy	0.8	2.0	0.05
FPS	1.0	2.4	0.05

Table 3.1: Response coefficients for SLy and FPS EOS (the "plateau" values)

– such a procedure is perfectly valid for small sizes $r_{\rm m}$ of the mixed-phase core, as displayed in Fig. 3.3. I have used many values of the phase-transition density and several values of $\gamma_{\rm m}$ from the range typically occurring in realistic EOSs. In this way it was possible to study the linear response of NS to the appearance of a small mixed-phase core for a wide choice of the mixed-phase parameters and star masses, even without precise knowledge of the details of the mixed phase.

Again, the coefficients β_Q depend only on the properties of the reference configuration C_0 – the EOS of the mixed-phase (here approximated by a polytrope) influences the results by the presence of the factor $(\gamma_{\rm N}/\gamma_{\rm m} - 1)$ (Eq. 3.12).

For each EOS, a family of reference configurations C_0 was obtained by changing the central density $\rho_{\rm c}$, thus spanning the available mass range. The comparison of C and C* configurations provides us with the values of the linear response coefficients $\beta_Q(\mathrm{C}_0)$. As can be seen in Fig. 3.5, for a wide, astrophysically interesting, range of NS masses the values of the functionals $\beta_Q(C_0)$ stay almost constant. Their "plateau" values are collected in Table 3.1.

The values of β_Q increase rapidly with decreasing mass below 0.4 $\mathrm{M}_\odot$. This behavior is due to the specific generic features of the realistic EOS of NS crust (Haensel, 2001) which results in the existence of the minimum NS mass $M_{\rm min}$ (see Haensel et al. 2002, and references therein). For $M \longrightarrow M_{\rm min}$, NSs become increasingly "soft" with respect to the fundamental mode of radial perturbations. Therefore, at the same value of mass-excess $\delta m_{\rm core}$ the NS radius decreases further due to the increased gravitational pull created by the mixed-phase core growth, and soon the star's response enters the non-linear regime, where higher-order effects become important. In the relevant stellar mass range, the FPS stars are generally less bound and, when the configuration mass decreases, the β_Q coefficients increase earlier than for the SLy EOS. The "softness" of hydrostatic equilibrium at M close to $M_{\rm max}$ with

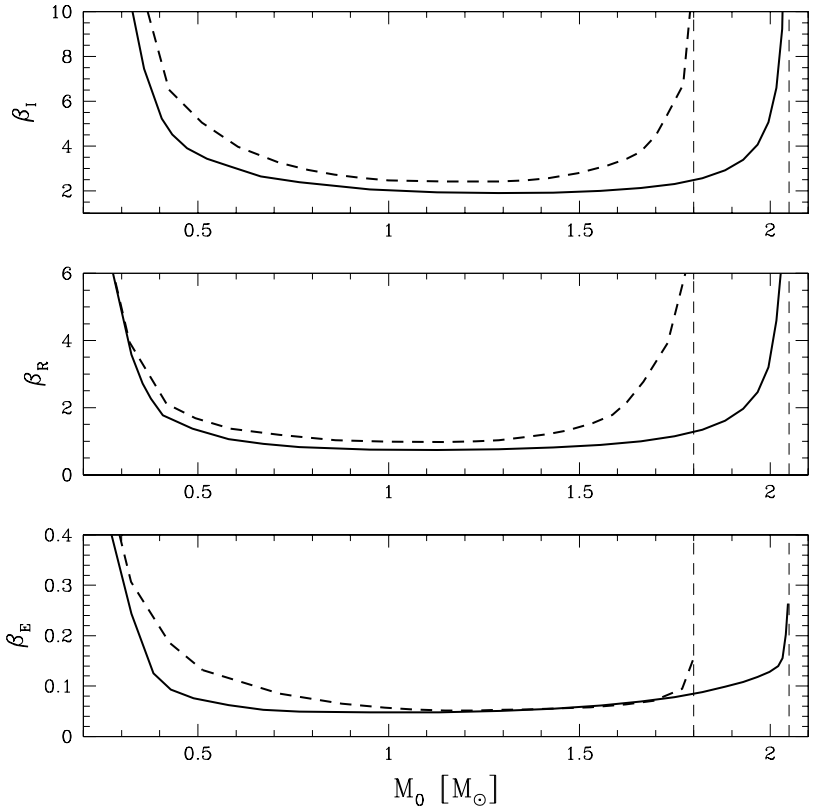

Figure 3.5: The linear response parameters β_Q versus the mass M_0 of the reference configuration C_0. The N phase is described by the SLy EOS (solid lines) and by FPS EOS (thick dashed lines). The vertical thin dashed lines denote the maximum allowable masses – $M_{\rm max}^{\rm SLy} = 2.05\ M_\odot$ for SLy EOS, and $M_{\rm max}^{\rm FPS} = 1.79\ M_\odot$ in the case of FPS EOS.

respect to radial perturbations is a general-relativistic feature, and does not depend on the N phase EOS, analogous to the very same effect in the case of Sect. 3.2.

An important parameter, relevant for evaluations of linear response to a perturbation of equilibrium configuration, is the adiabatic index of the N phase EOS – in Fig. 3.6 the respective values for SLy and FPS EOSs are shown, calculated at the centers of the reference configurations C_0 as functions of the configuration mass $M(C_0)$ as well its central baryon number density.

As we can see, the response coefficients depend rather weakly on the EOS of the N phase (assuming it is realistic). The M_0 range of the "plateau" region, $(0.6 - 1.6)\ M_\odot$, is narrower for FPS EOS than for the SLy EOS. The difference results from the fact that the maximum allowable masses are

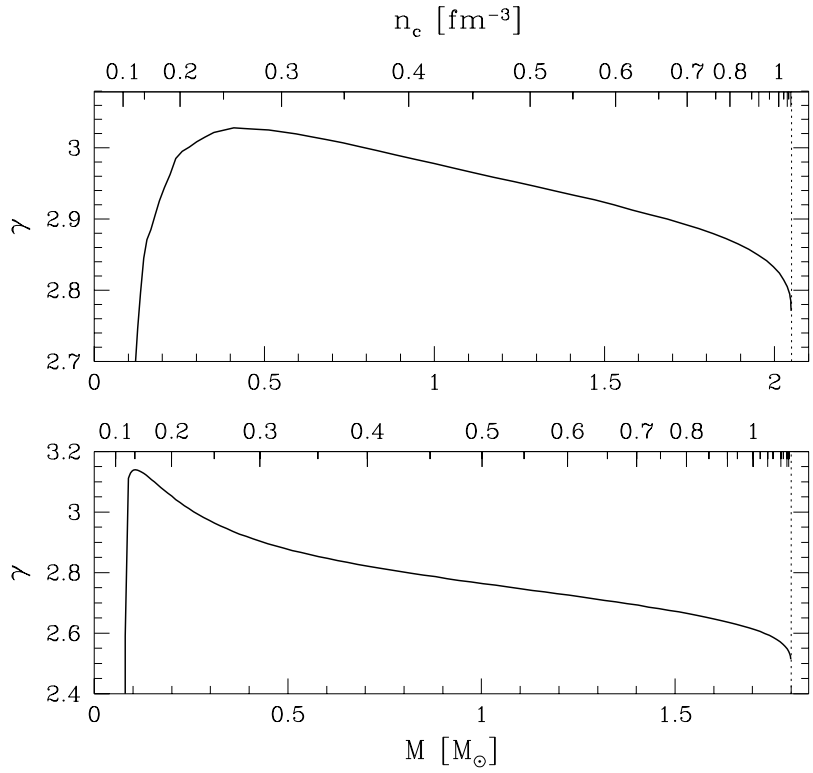

Figure 3.6: The value of the adiabatic index at the center of the non-rotating configuration for the SLy EOS (upper panel) and FPS EOS (lower panel), plotted against the gravitational mass (bottom horizontal axis), and the baryon number density n_c at the star center (upper horizontal axis). The vertical dotted lines mark the maximum allowable mass ($M_{\rm max}^{\rm SLy} = 2.05\ {\rm M}_\odot$ for the SLy EOS, and $M_{\rm max}^{\rm FPS} = 1.79\ {\rm M}_\odot$ for the FPS EOS).

different, $M_{\rm max}^{\rm FPS} = 1.79\ M_\odot$ in the case of FPS EOS to be compared with $M_{\rm max}^{\rm SLy} = 2.05\ M_\odot$ in the case of SLy EOS. Otherwise, the plateau quasi-constancy is valid up to about $0.8 - 0.9\ M_{\rm max}$, a feature which seems to be generic. On the low-mass side, the difference in the β_Q behaviour reflects the differences between the EOSs at sub-nuclear densities, as presented by Haensel et al. (2002).

Let us consider C_0 configuration with the mass 1.4 $M_\odot$ calculated for the SLy EOS. The star has radius $R_0 = 11.73$ km, moment of inertia $I_0 = 1.37 \times 10^{45}\ {\rm g \cdot cm^2}$, and central adiabatic index $\gamma_{\rm N} \simeq 2.94$. Using the "plateau" values of the β_Q coefficients from the Table 3.1, the adjusted formulae for the changes in NS parameters take a form more suitable for numerical estimates, similar to the ones in the polytropic case from Sect. 3.3.

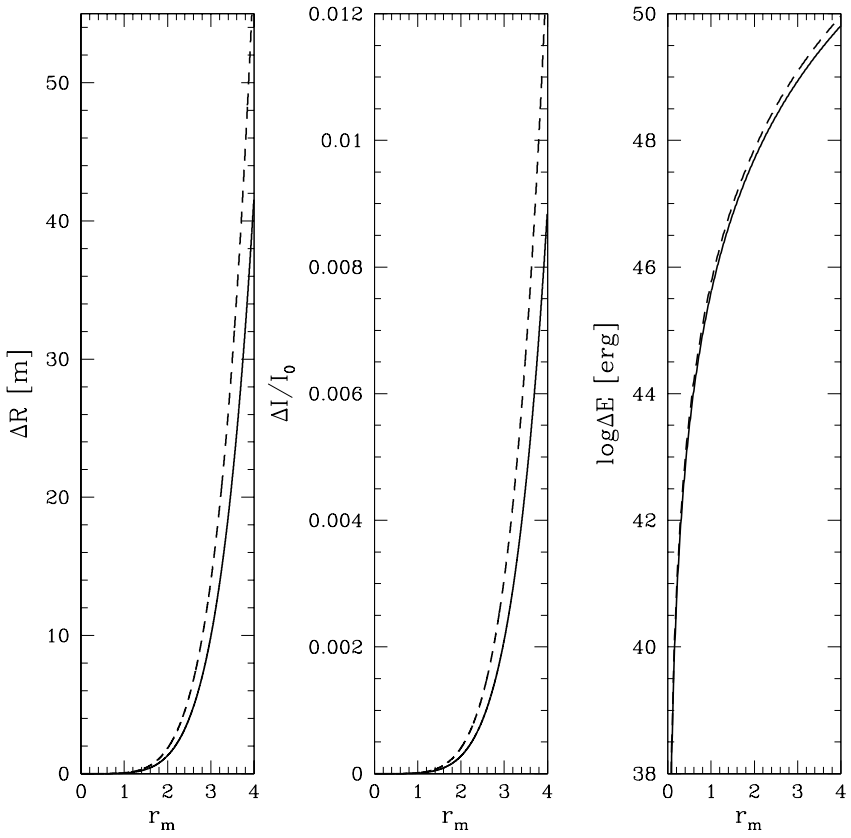

Figure 3.7: Changes of stellar parameters – relative change of the radius ΔR, fractional change of the moment of inertia $\Delta I/I_0$ and the logarithm of energy released ΔE as a function of the core radius, $r_{\rm m}$ for SLy EOS (solid line) and FPS EOS (dashed line).

The change in stellar radius R, fractional change in the moment of inertia I and the energy release ΔE read

$$\Delta R \simeq -4.23 \cdot 10^{-5} \times \left(\frac{\gamma_{\rm N}}{\gamma_{\rm m}} - 1\right) \left(\frac{r_{\rm m}}{1\ {\rm km}}\right)^5 \ {\rm km}\ , \tag{3.15}$$

$$\frac{\Delta I}{I_0} \simeq -9 \cdot 10^{-6} \times \left(\frac{\gamma_{\rm N}}{\gamma_{\rm m}} - 1\right) \left(\frac{r_{\rm m}}{1\ {\rm km}}\right)^5 \ , \tag{3.16}$$

$$\Delta E \simeq 4.1 \cdot 10^{45} \times \left(\frac{\gamma_{\rm N}}{\gamma_{\rm m}} - 1\right) \left(\frac{r_{\rm m}}{1\ {\rm km}}\right)^7 \ {\rm erg}\ , \tag{3.17}$$

respectively.

With the assumption of a mixed phase with $\gamma_{\rm m} = 1.5$, and the C_0 configuration $\gamma_{\rm N} \simeq 2.94$ the appearance of a 1 km core implies a relative change in radius ΔR of about 4 cm, a value which is perhaps small by terrestrial standards,

but is more than an order of magnitude than that which can be associated with macro-glitches in pulsar timing. The rise of the star-quake amplitude with $r_{\rm m}$ is very steep – for $r_{\rm m} = 2$ km we have $\simeq \Delta R = 32$ cm, for $r_{\rm m} = 3$ km $\simeq \Delta R = 2.5$ m, and for $r_{\rm m} = 4$ km $\simeq \Delta R = 42$ m, a truly impressive number.

The creation of a 1 km core implies speed-up of the NS rotation by $\Delta\Omega/\Omega \simeq 10^{-5}$, one order of magnitude larger than in the biggest pulsar macro-glitches. If $r_{\rm m} = 2$ km, we have $\Delta\Omega/\Omega \simeq 3 \times 10^{-4}$, whereas $r_{\rm m} = 4$ km implies $\Delta\Omega/\Omega \simeq 10^{-2}$, an extreme occurrence in pulsar timing.

Finally, a 1 km core with $\gamma_{\rm m} = 1.5$ releases a total energy of 4×10^{45} erg. The corresponding amounts of released energy for cores with $r_{\rm m} = 2$ km, $r_{\rm m} = 3$ km and $r_{\rm m} = 4$ km is 5×10^{47} erg, 9×10^{48} and 6.4×10^{49} erg, respectively.

The FPS EOS 1.4 $M_\odot$ configuration C_0 has radius $R_0 = 10.84$ km, moment of inertia $I_0 = 1.2 \times 10^{45}$ g cm^2 and central adiabatic index $\gamma_{\rm N} \simeq 2.68$. The numerical prefactors in Eqs. (3.15–3.17) for ΔR, $\Delta I/I_0$ and ΔE are equal to -7.24×10^{-5}, -1.6×10^{-5} and -7.1×10^{45}, respectively. The corresponding changes are thus comparable with those originating from the SLy EOS. In Fig. 3.7 I present the changes of the global parameters as a function of the radius of the core $r_{\rm m}$.

One can of course compare the derived released energy with energies associated with known astrophysical processes involving NSs: the energy associated with Soft Gamma Repeaters outbursts, caused by an extremely strong magnetic field, equals approximately $10^{44} - 10^{45}$ erg. The thermonuclear Type I X-ray bursts release energies in the range $10^{38} - 10^{40}$ erg, but in the case of the so-called super-bursts the released energy can reach 10^{43} erg. Estimates of energy involved in pulsar macro-glitches are around 10^{41} erg. As one can see, the released energies, as well as the changes of other parameters associated with core-quakes, are similar and sometimes much larger than those in observed astrophysical phenomena involving NSs.

3.4 Conclusions and remarks

The appearance of a mixed phase in the center of a star was analyzed by means of the linear response theory applied to the star's parameters. First,

a simple model of a polytropic star with a soft "mixed-phase" core provided set of precise formulae, useful for estimating the change of stellar parameters (such as radius, moment of inertia and released energy) for a given stiffness i.e. the adiabatic index γ of a star's mixed-phase core and its radius (the size of which is *a priori* unknown).

The resulting parameter changes turn out to be of the order of those associated with observed astrophysical phenomena involving NS. The analysis was repeated for a pair of recent realistic EOSs. It was shown that the inclusion of varying adiabatic index in the outer part of the star modifies the value of the response coefficients, but not dramatically – the orders of magnitude of the resulting changes of parameters stayed approximately the same.

The more-or-less constant values of β_Q far from maximum and minimum mass (i.e. extending within $0.5\ M_\odot \leqslant M(\mathrm{C}_0) \leqslant 0.9\ M_{\max}$ in case of realistic EOSs) are a few times smaller than the response coefficients for the pure S phase core, α_Q, calculated for a medium-stiff EOS of the N phase by Haensel et al. (1986b). The linear response coefficients depend weakly on the nature of the new-phase core, which enters either by $(\rho_{\mathrm{S}}/\rho_{\mathrm{N}}-1)(\bar{r}_{\mathrm{S}})^l$ in the case of a density jump phase transition to a pure S phase, or by $(\gamma_{\mathrm{N}}/\gamma_{\mathrm{m}}-1)(\bar{r}_{\mathrm{m}})^l$ in the case of structured mixed-phase transition.

To the lowest order, the change of stellar parameters Q depends on the mass excess in the core via

$$\delta Q \simeq \frac{\partial Q}{\partial m} \times \delta m_{\mathrm{core}}\ . \tag{3.18}$$

Numerical factors multiplying

$$(\gamma_{\mathrm{N}}/\gamma_{\mathrm{m}}-1)\left(\frac{r_{\mathrm{m}}}{R_0}\right)^5 \quad \text{or} \quad (\rho_{\mathrm{S}}/\rho_{\mathrm{N}}-1)\left(\frac{r_{\mathrm{S}}}{R_0}\right)^3$$

in Eq. (3.2) or Eq. (3.11), respectively, differ by $\frac{1}{15}\kappa_{\mathrm{N}}^2 R_0^2$. This quantity is approximately the difference ratio between the β_Q and α_Q values mentioned above. We can estimate the value of $\frac{1}{15}\kappa^2 R_0^2$ from the special case of a $\gamma = 2$ Newtonian polytrope. Assuming $P = k\rho^2$ EOS one has from the Lane-Emden equation (see e.q., Glendenning 1997, Sect. 3.9.4) the constant radius $R_0 = \sqrt{k\pi/2G}$. The coefficient κ from Eq. (3.5) will be equal $\sqrt{2\pi G/k}$, because the sound velocity equals $v = \sqrt{2k\rho}$. Thus $\kappa^2 R_0^2 = \pi^2$, and one has $\frac{1}{15}\kappa^2 R_0^2 \simeq 2/3$. Relativistic corrections and the fact that γ is not necessarily equal to 2 put this value closer to 1/3.

It should be also stressed that the core radius is not a *free* parameter, because in principle it is determined by the physical properties of the EOS, i.e. by the range of metastability possible in the considered physical situation. This range is however rather poorly known. The mixed phase core radius $r_{\rm m}$ is related to the range of metastability in the following way: the difference between $\rho_{\rm crit}$ and $\rho_{\rm N}^{\rm (m)}$ which can be sustained by the N phase is, according to Zdunik et al. (1987), given by:

$$\Delta\bar{\rho}_{\rm crit} = \frac{\rho_{\rm crit} - \rho_{\rm N}^{\rm (m)}}{\rho_{\rm N}^{\rm (m)}} = \frac{1}{6}\kappa_{\rm N}^2(1+x)(1+3x)r_{\rm m}^2 \ . \tag{3.19}$$

On the basis of the above considerations with a Newtonian $\gamma = 2$ polytrope for the core radius $r_{\rm m} = 1$ km and the canonical radius of the NS $R_0 \simeq 10$ km we have $\kappa^2 r_{\rm m}^2 \simeq 0.1$. Thus, the leading terms in Eqs. (3.15–3.17) correspond to the degree of metastability (also called over-compression) of the order of 1% i.e. $\Delta\bar{\rho}_{\rm crit} \simeq 0.01$. Creation of mixed-phase in realistic matter demands presumably much higher over-compression, e.g. of the order of 10% ($\Delta\bar{\rho}_{\rm crit} \simeq 0.1$). This value corresponds to the appearance of a 3 km mixed-phase core which is perfectly well described by linear theory.

Chapter 4

Phase transitions in rotating stars

This chapter contains the results of extensive numerical calculations of rotating axisymmetric stars within the framework of General Relativity. Special attention is placed on the influence of phase transitions on the observational properties of NSs.

Glendenning et al. (1997) proposed a particularly interesting method of finding an EOS dependence on the behavior of pulsar observables, such as the spin frequency Ω and its derivatives, like the braking index $n(\Omega) = \Omega\ddot{\Omega}/\dot{\Omega}^2$.

Solitary pulsars increase their spin periods due to magnetic dipole braking. During this spin-down era, the central density of the star increases as a result of decreasing centrifugal force. At a certain density a new phase of matter can appear (in an example considered by Glendenning et al., the new phase consisted of de-confined quarks). As the star becomes more and more dense in its interior, its global parameters, e.g. the moment of inertia I, gradually change. It has been suggested that the softening of the EOS induced by the creation of a new phase leads to the *temporary spin-up era* while still losing angular momentum – a phenomenon called *back-bending* (BB). The name comes from nuclear physics; the feature was observed for the first time in an excited nuclei (see, e.g., Ring and Schuck 1980). Glendenning et al. held the BB feature to be a signature of hadron-quark de-confinement (see Fig. 4.1 for original plots). Their calculations were, however, performed within the *slow-rotation approximation*, called Hartle's perturbation theory (Hartle, 1967; Hartle and Thorne, 1968), improved by considering the rotational stretching and frame-dragging effects (Weber and Glendenning, 1991, 1992). Several other authors

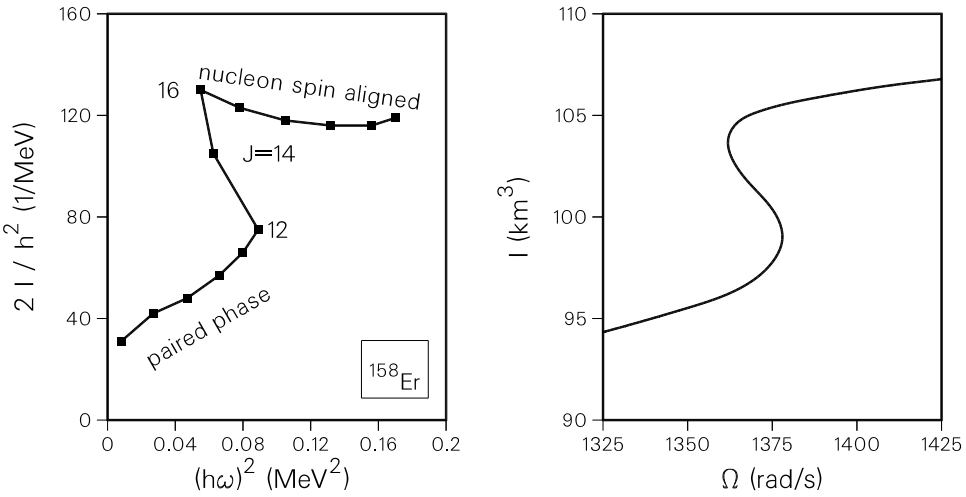

Figure 4.1: The back-bending phenomenon as proposed by Glendenning et al. (1997). Left panel: back-bending in nuclear physics. Nuclear moment of inertia I as a function of squared frequency ω (defined as $\omega = \mathrm{d}E/\mathrm{d}J$, where E is the excitation energy, and J is the angular momentum number; h denotes here the Planck constant) for ^{158}Er. Right panel: back-bending in the astrophysical case. Ω is the angular frequency; the evolution proceeds from high to low I (figures were taken from Glendenning et al. 1997, and Glendenning and Weber 2001a)

(Heiselberg and Hjorth-Jensen, 1998; Chubarian et al., 2000) performed their calculations using similar approximate methods. The comparison with *exact* (i.e., non-perturbative) numerical methods reveals dramatic a break-down of the slow-rotation approximation for angular velocities close to the Keplerian limit, as advocated in Chapter 2. I will show in subsequent sections that the problem of BB requires careful and precise calculations.

The first calculations concerning BB which were based on *exact* methods were performed by Cheng et al. (2002). The authors used a version of the KEH code (Komatsu et al., 1989a,b) improved by Stergioulas and Friedman (1995). In their work, Cheng et al. focused on the influence of the stellar crust on the final existence of BB. Indeed, as they show, even the slight change in the physical state of the crust (for example, change in the crust-core transition pressure) significantly affects the results.

Another computation based on SF code by Stergioulas and Friedman (1995) was published by Spyrou and Stergioulas (2002). The authors show that the results by Glendenning et al. (1997) are biased by huge numerical uncertainties; in fact, the very same EOS used by Glendenning et al. (EOS from Table 9.2

by Glendenning 1997) presented in Fig. 4.1 did not yield the BB phenomenon at all! My own work confirms this result of Spyrou and Stergioulas – during numerical runs it was impossible to obtain BB feature using this EOS in its original form. Also, some errors in previous papers were pointed out; for example, the method of calculating the braking index $n(\Omega)$ basing on numerical results was corrected for full compatibility with General Relativity (Sect. 6 in the article by Spyrou and Stergioulas 2002). Recently Banik et al. (2004) also produced a set of EOSs softened by the appearance of hyperons, kaon condensates and quarks, where the BB features were present.

It must be mentioned that, at the beginning of this work, it was not entirely clear if BB can be obtained by means of *exact* calculations. The problem turned out to be much more subtle than that considered by other authors, it requires careful handling, high-precision computations, as well as strict preservation of the thermodynamical consistency of the EOS. I believe that the approach presented here satisfies these conditions. To solve the BB conundrum I have searched the parameter space for parametric polytropic EOSs (described in Appendix B) in order to understand the principles of the BB phenomenon. I used both "constant-pressure" (density jump) and "structured mixed-phase segment" phase transitions. The calculations were performed by means of the methods outlined in Sect. 2.1 – the numerical implementation of the method, the `rotstar` code for simulations of axisymmetric rotating stars is a part of the `LORENE` scientific library. In order to achieve a numerical accuracy of 10^{-7} measured by the values of the virial errors (Gourgoulhon and Bonazzola, 1994; Bonazzola and Gourgoulhon, 1994) I have mostly used 65 collocation points in the radial r direction and 33 in the θ direction for a star composed of 3 domains and a polytropic EOSs. The results for realistic EOSs were somewhat less precise, with a mean virial error accuracy of 10^{-5}.

For simplicity, I will assume that the phase transition occurs quasi-statically (or equivalently, that the transition from the meta-stable core to the new phase core is negligible). The considerations in the case of a spinning down pulsar are contained in Sect. 4.1. As an example, a realistic EOS will also be presented – it will be shown that BB is not necessarily a signature of exotic phases, like the hadron-quark de-confinement in the center of NS (in the provided example the EOS is softened by the appearance of hyperons). I will also take into account

accreting stars with phase transitions, and study the interplay of accretion and BB – the case of polytropic EOSs is presented in Sect. 4.2, along with an example of a realistic EOS (the same as in Sect. 4.1). Sect. 4.3 contains conclusions and remarks.

4.1 Back-bending in spinning-down pulsars

The back-bending phenomenon was studied on a large sample of parametric EOSs – both constant-pressure and "mixed-phase" transitions were used in order to reveal its main properties. For the purpose of this discussion I will present three different "structured mixed-phase" EOSs, each of them showing different features of spin-up by angular momentum loss. I want to emphasize the correspondence between the EOS and the global parameters of stellar configurations based on this EOS. Therefore, the EOSs were selected according to their stability properties against axisymmetric perturbations of stellar configurations. The chosen EOSs are labelled according to the stability properties of non-rotating stars near the point of phase transition: MSt (stable), MUn (unstable) and MM (marginally stable). The parameters of the EOSs are collected in Table 4.1. The relation between the pressure P and the mass density ρ, as well as the baryon mass M_{B} and the radius R for non-rotating configurations, is presented in Fig. 4.2. The presence of a "mixed-phase" segment strongly decreases the maximum allowable mass – extended softening in the case of realistic EOSs will result in their inconsistency with observational data. The onset and length of the "mixed phase" were chosen to be more-or-less compatible with the values from realistic EOSs.

Concerning the stability of rotating axisymmetric configurations, one should always use appropriate variables so as to immediately know if a given star is stable against the axisymmetric perturbations in our case. Unstable configurations are not observed astrophysically, because their lifetime is too short – one can say that those states are not realized in nature. Unlike other authors concerned with the BB phenomenon, I will not use the moment of inertia I to study the properties of a star's spin-up. Instead of I a more basic variable, namely the angular momentum J as a function of spin frequency Ω, will be used. There are many reasons to do so: the definition of the moment of inertia

EOS	$\gamma_{\rm N}$	$n_{\rm Nm}$ [fm^{-3}]	$\gamma_{\rm m}$	$n_{\rm mS}$ [fm^{-3}]	$M_{\rm B}^{\rm stat}$ ($M^{\rm stat}$) [$M_\odot$]
MSt	2	0.35	1.5	0.8	1.508 (1.393)
MUn	2.5	0.2	1.3	0.65	1.586 (1.453)
MM	2.25	0.25	1.25	0.57	1.685 (1.534)

Table 4.1: Main parameters of the polytropic EOSs with mixed-phase transition segment. Below the mixed-phase transition point $n_{\rm Nm}$ – polytropic EOS with $\gamma_{\rm N}$, mixed phase: $n_{\rm Nm} < n_{\rm b} < n_{\rm mS}$ – polytrope with adiabatic index $\gamma_{\rm m}$. Above the density $n_{\rm mS}$ – quarks with linear EOS. In all cases the polytropic pressure coefficient K was equal to 0.025 (see Appendix B for details). $M_{\rm B}^{\rm stat}$ and $M^{\rm stat}$ denote the maximum allowable baryon and gravitational mass of the non-rotating star. The EOSs are labelled are as follows: MSt denotes the stable BB, MUn – the unstable BB, and MM is the marginally stable case (see text for details).

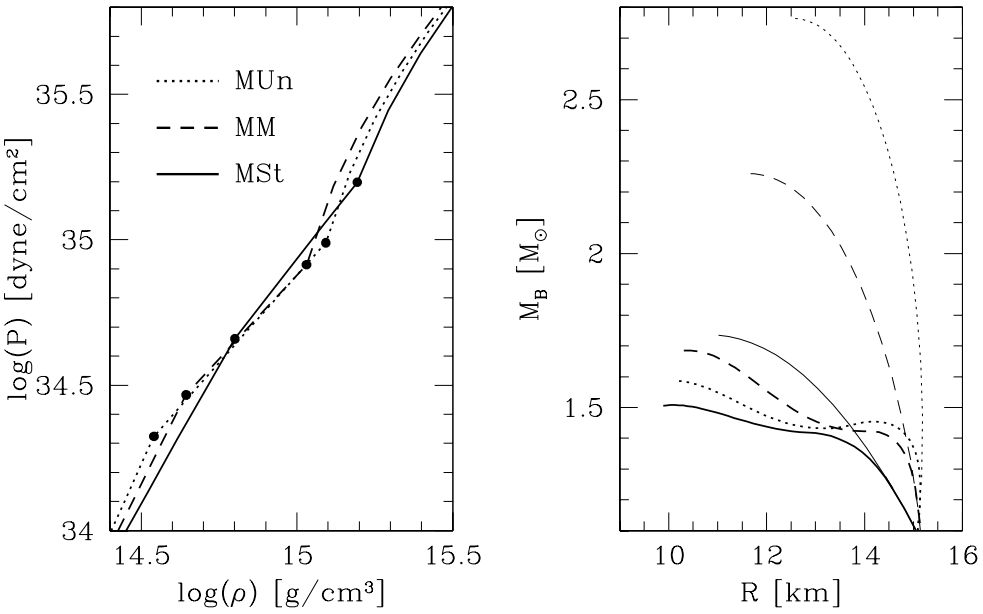

Figure 4.2: Left panel: Pressure P as a function of the mass density ρ on logarithmic scales for three sample EOSs with the "mixed-phase" segments: solid lines – MSt EOS, dotted – MUn EOS, dashed – MM EOS. Black dots denote the beginning and the end of the "structured mixed phase". Right panel: The baryon mass $M_{\rm B}$ as a function of the radius R for the non-rotating MSt, MUn and MM configurations (thick lines) and their corresponding configurations without "mixed-phase" segment (thin lines).

$I = J/\Omega$ used by previous authors is valid in the slow rotation approximation only. In the general case, the relation between the infinitesimal change of the angular momentum J and the change of the frequency Ω should be defined as $I = {\rm d}J/{\rm d}\Omega$; both definitions agree in slow rotation regime. Moreover, although J is not directly related to observables, and is not directly measurable,

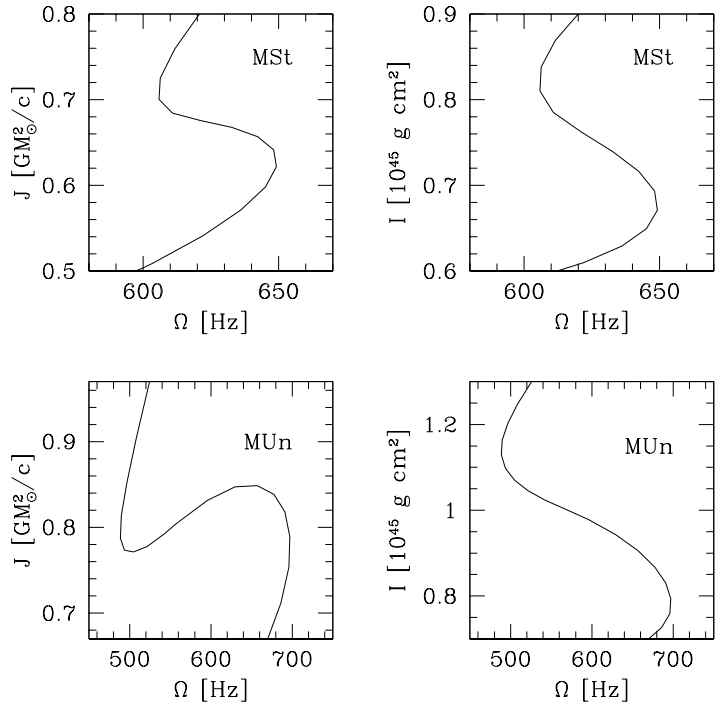

Figure 4.3: The back-bending phenomena in $J(\Omega)$ and $I(\Omega)$ variables – for stable BB (MSt EOS, upper panels) both $J(\Omega)$ and $I(\Omega)$ plots look qualitatively the same. In the case of MUn EOS (lower panels) the unstable branch visible in $J(\Omega)$ plot is not visible when one uses $I(\Omega)$.

it is a well-defined quantity which describes the state of the rotating star. The change of stability corresponds to the extremum of the gravitational mass M or the baryon mass $M_{\rm B}$ at fixed J. If the sequence is parametrized by the parameter α (e.g., central density or pressure), we have

$$\left(\frac{\partial M}{\partial \alpha}\right)_J = 0 \ , \quad \left(\frac{\partial M_{\rm B}}{\partial \alpha}\right)_J = 0 \ . \tag{4.1}$$

These conditions are equivalent to

$$\left(\frac{\partial J}{\partial \alpha}\right)_M = 0 \ , \quad \left(\frac{\partial J}{\partial \alpha}\right)_{M_{\rm B}} = 0 \ . \tag{4.2}$$

The configurations which have maxima of $M_{\rm B}$ and M for a fixed angular momentum J coincide, as was shown by Friedman et al. (1988) for uniformly rotating configurations. The advantage of using J and not I during the exploration of BB features is clearly visible in Fig. 4.3. One can easily confuse stable spin-up during the angular momentum loss (upper panel) with its unsta-

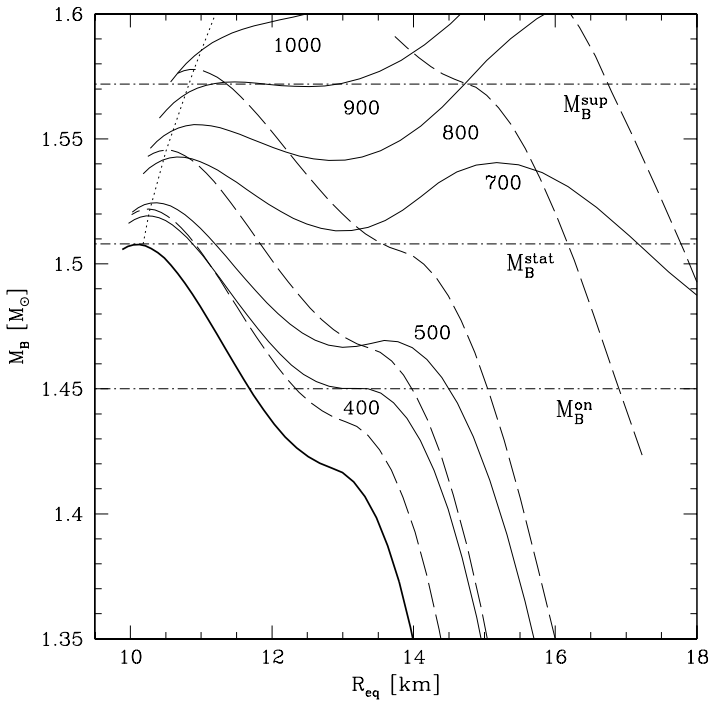

Figure 4.4: The baryon mass $M_{\rm B}$ as a function of the stellar equatorial radius $R_{\rm eq}$ for the MSt EOS featuring stable BB phenomenon. Solid lines correspond to a fixed angular frequency, whereas dashed lines to a fixed angular momentum. As shown, the curves have no extrema, except the maximum allowable mass point – i.e. they show no instabilities due to the phase transition – the dotted line represents the instability line corresponding to the maximum allowable mass. Labels denote constant spin frequency tracks. The lowest horizontal dash-dotted line marks the onset of BB – the inflection point in $M_{\rm B}(R_{\rm eq})$ curve – $M_{\rm B}^{\rm on} = 1.45\ M_\odot$ and $\Omega_{\rm on} \simeq$ 400 Hz, the line in the middle denotes the maximum mass of a static configuration: $M_{\rm B}^{\rm stat} = 1.508\ M_\odot$ and the upper line separates the curves with and without local minimum in $M_{\rm B}$, $M_{\rm B}^{\rm sup} = 1.572\ M_\odot$.

ble analogue (lower panel), because in the $I(\Omega)$ plane they look qualitatively the same.

Let us now focus on the properties of stable spin-up during angular momentum loss which, as was mentioned, corresponds to the case of a solitary pulsar losing J by magnetic dipole braking. First, the properties of the mass-radius relation for the MSt EOS will be outlined. Fig. 4.4 shows the relation between the baryon mass $M_{\rm B}$ (a suitable parameter, as its value stays constant during the lifetime of a solitary pulsar) and the equatorial radius $R_{\rm eq}$ for fixed spin frequency Ω (solid lines) and fixed angular momentum J (dashed lines). The BB phenomenon is directly related to the existence of a local minimum of

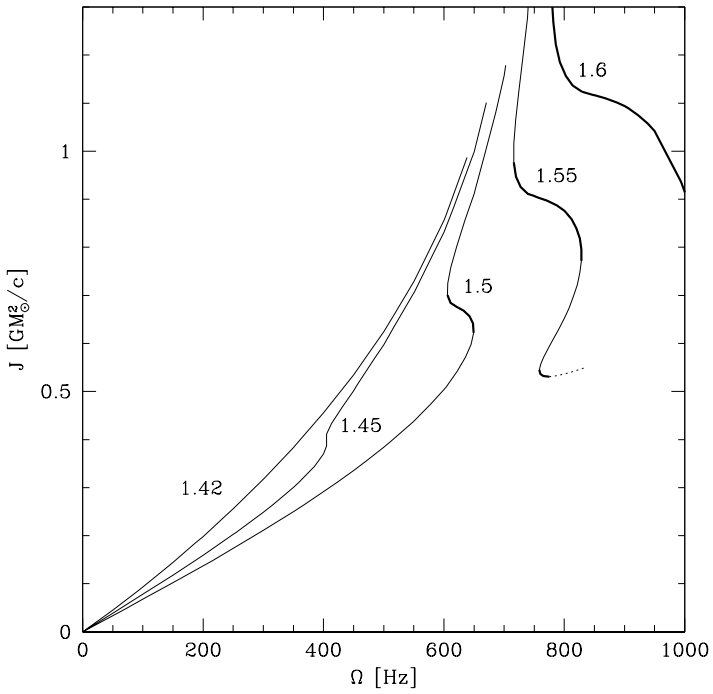

Figure 4.5: The angular momentum loss evolution for solitary pulsar with MSt EOS (stable BB). Labels denote constant baryon mass tracks. The BB onset mass is $M_{\rm B}^{\rm on} = 1.45\ M_\odot$. For the larger masses BB is present – thick solid lines denote those parts of a lifetime where during losses of J the stars spin up. The small spin-up feature at the end of the supra-massive 1.55 $M_\odot$ sequence is described in the text. Dotted segments denote unstable configurations.

$M_{\rm B}$ for a given constant Ω. Likewise, we suspect that the stability properties will be visible in the behavior of the curves related to the constant angular momentum – as shown, all configurations with $M_{\rm B}$ smaller than the maximum allowable value are stable. For a certain frequency $\Omega_{\rm on}$, in this case $\simeq 400$ Hz (denoted by a dash-dotted line), a segment of the $M_{\rm B}(R_{\rm eq})$ curve becomes horizontal. It means that the first and second derivatives of $M_{\rm B}$ with respect to (for example) central density vanish at some point – the curve suffers an inflection. This effect is due to the phase transition softening. The frequency $\Omega_{\rm on}$ marks the *onset* of BB. Curves corresponding to higher frequencies develop a *local maximum* of $M_{\rm B}$. The evolution of a solitary pulsar proceeds along the constant baryon mass from right to left-hand side of the Fig. 4.4. It is clear that above $M_{\rm B}^{\rm on} = 1.45\ M_\odot$ the spinning down configuration must cross the local maximum, and thus it will temporarily enter the region of spin up. For those

configurations the BB is present. It should be clearly stated that the minimum of $M_{\rm B}(R_{\rm eq})$ for a given frequency is not equivalent to the instability, but only to the appearance of BB. The second horizontal dash-dotted line marks the value of the maximum baryon mass $M_{\rm B}^{\rm stat}$ of the static configuration. This is important from the point of view of the existence of BB for normal (below the maximum mass) and supra-massive (above the maximum mass) configurations – if $M_{\rm B}^{\rm on} < M_{\rm B}^{\rm stat}$ we will have BB for normal configurations. The third line, denoted by $M_{\rm B}^{\rm sup}$, separates the configurations which are able to spin-up only, while still losing angular momentum. In this region of high Ω values there is no longer a local minimum of $M_{\rm B}$ with respect to $R_{\rm eq}$.

The same EOS is presented in Fig. 4.5, this time in J and Ω variables. The curves represent the loss of angular momentum and corresponding spin-down (or spin-up) of a star. Above the BB onset mass $M_{\rm B}^{\rm on} = 1.45\ M_\odot$ the BB phenomenon is present (segments where the configurations temporarily spin up are marked with thicker lines). Normal configurations with $M_{\rm B} < M_{\rm B}^{\rm stat}$ after a possible BB end their life in the zero angular momentum state. The case of supra-massive configurations is different: a star with $M_{\rm B} > M_{\rm B}^{\rm stat}$ cannot lose all its angular momentum without dramatic consequences – it will eventually collapse to a black hole. The onset of collapse is also accompanied by spin-up, like in the case of a supra-massive $1.55\ M_\odot$ sequence in Fig. 4.5 – before the instability line (dotted line in Fig. 4.4) the supra-massive star must cross the spin-up region. A proof for this statement follows from the turning-point method developed by Sorkin (1981, 1982) and applied by Friedman et al. (1988) for the case of axisymmetric rotating stars. The authors state that for a continuous sequence of rotating configurations labelled by some parameter α, and with the assumption of $\mathrm{d}M_{\rm B}/\mathrm{d}\alpha \equiv 0$, the *unstable* region corresponds to a part of a sequence for which

$$\frac{\mathrm{d}J}{\mathrm{d}\alpha}\frac{\mathrm{d}\Omega}{\mathrm{d}\alpha} > 0\ . \tag{4.3}$$

This is equivalent to the following condition:

$$\frac{\mathrm{d}J}{\mathrm{d}\Omega}\left(\frac{\mathrm{d}\Omega}{\mathrm{d}\alpha}\right)^2 > 0 \Longrightarrow \frac{\mathrm{d}J}{\mathrm{d}\Omega} > 0\ , \tag{4.4}$$

thus just before the instability one should have $\mathrm{d}J/\mathrm{d}\Omega < 0$ – spin-up by angular momentum loss. Note that this type of a spin-up is a feature of

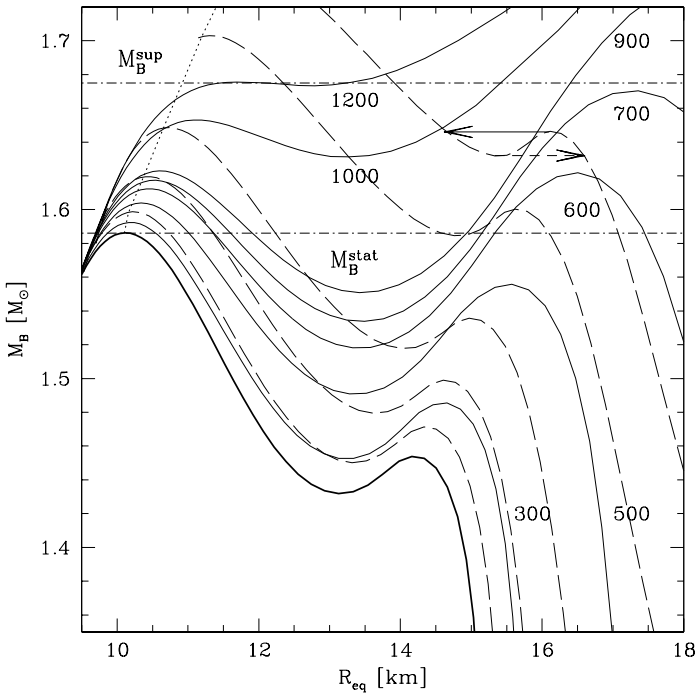

Figure 4.6: The baryon mass $M_{\rm B}$ as a function of the stellar equatorial radius $R_{\rm eq}$ for the MUn EOS featuring unstable BB phenomenon. Notation of lines is the same as in Fig. 4.4. Labels denote constant spin frequency tracks, $M_{\rm B}^{\rm stat} = 1.586\ M_\odot$ and $M_{\rm B}^{\rm sup} = 1.675\ M_\odot$. The region between the minima and local maxima on fixed-J curves is prohibited for axisymmetric rigidly rotating configurations. Arrows are related to energetically favorable transitions (collapses) - see Figs. 4.7 and 4.8 as well as text for details.

any sufficiently stiff EOS. In contrast, a most interesting phenomenon exists for configurations with a non-trivial behavior of the $M_{\rm B}(R_{\rm eq})$ relation near the phase transition point at a certain rotation rate. Finally, there also exist configurations above the $M_{\rm B}^{\rm sup} = 1.572\ M_\odot$ mass – they reveal permanent spin-up during angular momentum loss, with a termination point at the instability line where a rotating configuration collapses to a black-hole. Note that these features demand a delicate balance between the stiffness of a mixed phase and its extent in the density. If the mixed phase is too stiff compared to a normal N phase, or if it leads too quickly to a pure S phase, the EOS will not have sufficient influence on the global parameters of the star, and the BB feature will not be present. Also, the S phase should be sufficiently stiff to protect the star against entering the instability region.

An example demonstrating the case of the BB phenomenon with an unstable

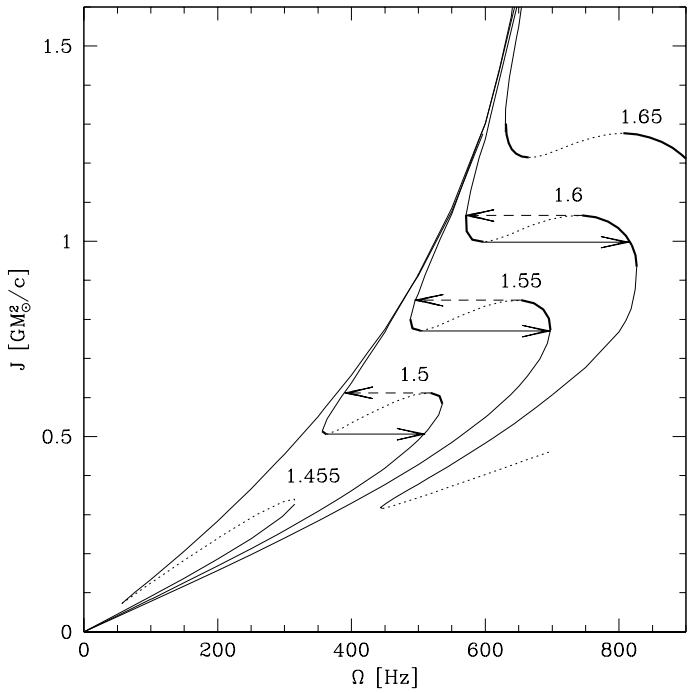

Figure 4.7: The angular momentum loss evolution for solitary pulsars with the MUn EOS (unstable BB). The region of unstable configurations propagates for all frequencies – for $J = 0$ EOS is unstable against axisymmetric perturbations. Thick lines denote the spin-up by angular momentum loss, whereas dotted lines correspond to the region of unstable configurations. Labels denote constant baryon mass tracks. Arrows represent transitions of an unstable star to energetically favorable "twin" with the same baryon mass: solid – during spin-down, dashed – in non-physical example of spinning up without adding mass (see text for details).

EOS, corresponding to stellar configurations which are unstable against the axisymmetric perturbations, is presented in $M_{\rm B}(R_{\rm eq})$ plane in Fig. 4.6 (configurations built with the use of the MUn EOS). Even for the non-rotating configurations (which correspond to constant angular momentum $J = 0$) the mass-radius relation exhibits a local maximum near the transition point. This means that the configurations between the extrema on which $M_{\rm B}$ decreases with decreasing $R_{\rm eq}$ are unstable. The EOS was specially prepared to be too soft in the "mixed-phase" region and to destabilize the star. All of the dashed curves denoting $M_{\rm B}(R_{\rm eq})$ relation for fixed J also show the minimum, i.e. the presence of an instability region. The situation does not change with increasing Ω – the spin-up BB phenomenon is even more pronounced (as it was in the stable case). The increase of J does not alter the stability of the system.

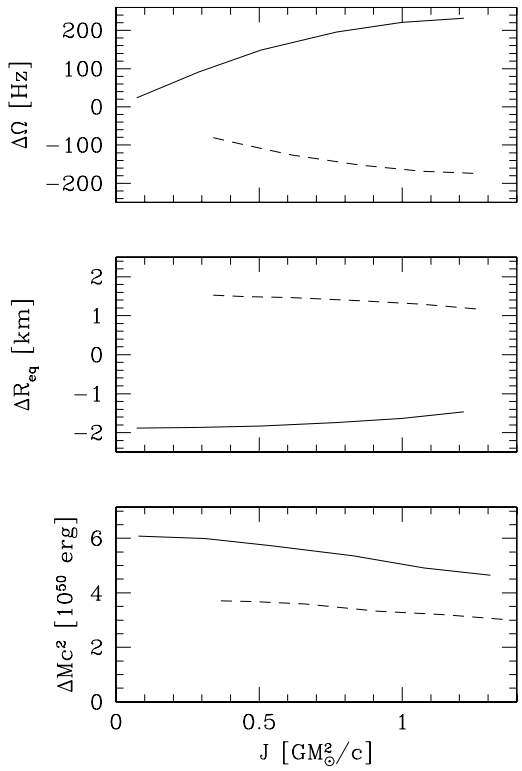

Figure 4.8: Changes in the frequency Ω, the radius $R_{\rm eq}$ and the total energy $E = Mc^2$ of a rotating star due to collapse to another configuration in the case of unstable back-bending (MUn EOS). Notation of solid and dashed lines is related to arrows in Figs. 4.6 and 4.7.

Other features of BB are essentially the same as previously shown. An interesting question arises, however – what will be the observational signatures if the star enters the instability region? Solid and dashed arrows correspond to the transition from an unstable star to its more energetically favorable "twin" – this very transition is presented more clearly in Fig. 4.7 in the $J(\Omega)$ plane.

The instability region (dotted segments) persists from low to high masses – it cannot be penetrated by axisymmetric rigidly rotating stars. Solid arrows shows the collapse from the instability point (minimum in J) for a spinning down star to a more compact "twin" configuration (the same baryon mass $M_{\rm B}$ and angular momentum J), whereas dashed arrows are related to the somewhat non-physical case of spinning up without acquiring the mass (moreover, this transition increases the radius of a star). For both cases, the changes in the spin frequency $\Delta\Omega$, the radius $\Delta\ R_{\rm eq}$ as well as the released energy (change

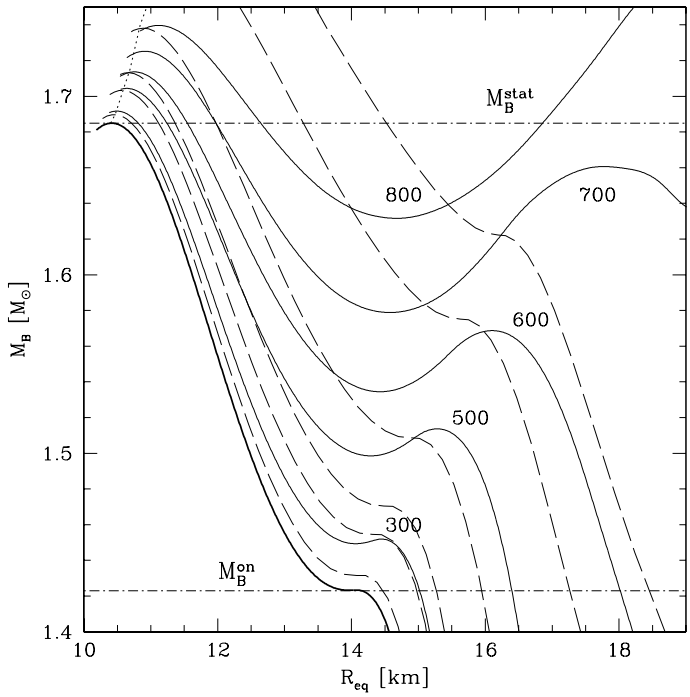

Figure 4.9: The baryon mass $M_{\rm B}$ as a function of the stellar equatorial radius $R_{\rm eq}$ for the MM EOS featuring marginally stable BB phenomenon. Lines are denoted in the same way as in previous figures. The lowest horizontal dash-dotted line marks the onset of BB (inflection point in $M_{\rm B}(R_{\rm eq})$ curve) – in this case the onset frequency $\Omega_{\rm on} = 0$ Hz, and the marginal onset mass $M_{\rm B}^{\rm on,cr} = 1.423\ M_\odot$. $M_{\rm B}^{\rm stat}$ equals 1.685 $M_\odot$.

in the total mass-energy $\Delta E = \Delta M c^2$) are plotted as a functions of the angular momentum J in Fig. 4.8. As we can see, both transitions are energetically favorable – the released energy $\Delta M c^2$ is quite large ($\sim 10^{50}$ erg), and depends weakly on J. Also, the changes of the radius and corresponding spin-up (or spin-down) are not small for massive stars with large J. Note however, that these presented results follow from a simple comparison of two configurations, and do not take into account possible physical processes occurring during the collapse. All those processes will most certainly influence the assumption of constant J. Therefore, this result should be treated as a kind of idealization and an estimation of the upper bound for the changes in stellar parameters.

In order to explore the conditions for appearance or disappearance of the instability region, yet another EOS (called the MM EOS – the marginally stable EOS) was employed, as Fig. 4.9 indicates. Its name comes from the fact that the $M_{\rm B}(R_{\rm eq})$ curve for non-rotating configurations near the phase transition

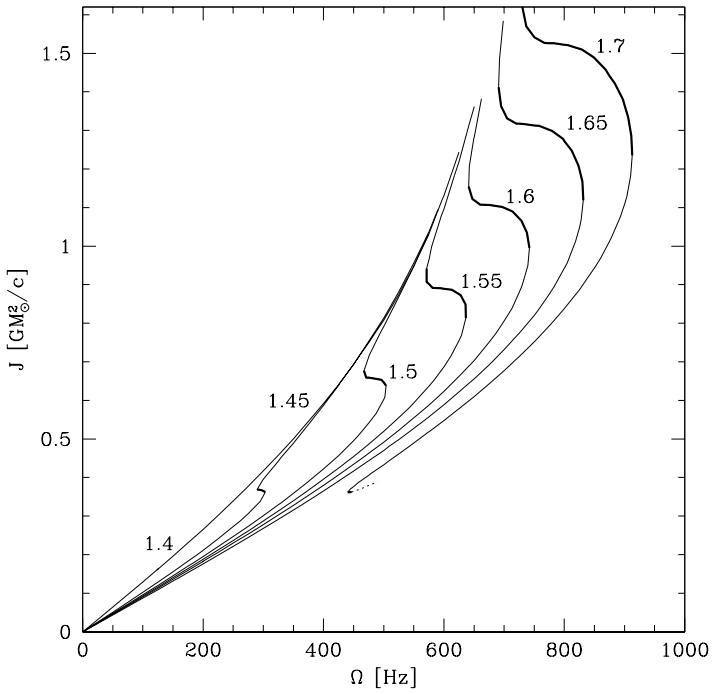

Figure 4.10: The angular momentum loss evolution for solitary pulsars built with the use of the MM EOS (marginally stable BB). Labels denote constant baryon mass tracks. Horizontal spin-up segments correspond to similar features in Fig. 4.10 on the constant angular momentum J sequences.

point (around $R_{\rm eq} = 14$ km and $M_{\rm B} = 1.42\ M_\odot$) exhibits an inflection point, so that BB appears at negligible spin frequency. We can define the marginal BB onset mass as $M_{\rm B}^{\rm on,cr} = M_{\rm B}^{\rm on}(\Omega = 0) = 1.423\ M_\odot$. What is remarkable, though, is that the "flat segment" near the inflection point of $M_{\rm B}(R_{\rm eq})$ curve persists for fixed-J tracks, and there is no sign of a loss of stability! (one cannot see the change in the character of dashed curves.) This fact is also presented in Fig. 4.10 – the spin-up (BB) parts of $J(\Omega)$ curves marked with bold lines are always horizontal without any firm trend one way or another.

Based on detailed and comprehensive numerical calculations, I have reached the conclusion that it is nearly impossible to decide whether the rotation *stabilizes* or *destabilizes* a given configuration. The plot of the energy release against the angular momentum J in Fig. 4.8 may serve as a partial answer – the energy-angular momentum dependence is too weak to change the stability state of a rotating star, i.e. to cause a sign change of ΔMc^2 at some J. Still, the

above statement is not a strict theorem. In one case, namely an incompressible EOS with a density jump between two "phases", I have obtained the onset of instability at a non-zero spin frequency, although the non-rotating star was stable (for a density jump very close to the critical parameter, for which a non-rotating star is unstable). It should be stressed that from an astrophysical point of view the "changing of stability" effect is marginal and irrelevant, in the sense that it requires serious fine-tuning of the EOS in order to occur. It seems that up to the level of numerical accuracy *the state of the non-rotating configuration decides about the stability of the rotating configurations* – if there exists an instability region, it occurs for all frequencies (i.e. it propagates for higher rotation rates and angular momenta).

I have also performed calculations on a large sample of polytropic *constant-pressure phase transition EOSs* in order to test the influence of rotation on the appearance of BB and, especially, to check how the spin frequency influences the parameters related to BB. The transition between pure phases was approximated by a density jump between polytropes of adiabatic indices $\gamma_{\rm N}$ and $\gamma_{\rm S}$ ($\gamma_{\rm N} \leqslant \gamma_{\rm S}$). The important parameter here is the value of the density jump, defined as $\lambda = n_{\rm S}/n_{\rm N}$, similar to the case studied by Zdunik et al. (1987): the authors showed that the appearance of a new dense phase destabilizes the non-rotating configuration if $\lambda_\rho = \rho_{\rm S}/\rho_{\rm N} > \frac{3}{2}(1 + x_{\rm N})$, where $x_{\rm N}$ is the ratio of pressure P to the energy-density $\rho_{\rm N}c^2$ at the transition point. However, the condition $\rho_{\rm S}/\rho_{\rm N} < \frac{3}{2}(1+x_{\rm N})$ determines the stability only in the vicinity of the transition. The correspondence between λ and λ_ρ follows from the equality of chemical potentials: $\lambda = \lambda_\rho(1 + x_{\rm S})/(1 + x_{\rm N})$; $x_{\rm S} = P/\rho_{\rm S}c^2$.

Let us define $\lambda_{\rm cr}$ as the baryon density jump for which the $M_{\rm B}(R_{\rm eq})$ relation for a non-rotating star has an inflection point at $\Omega = 0$ Hz, similarly to the case of the marginally stable MM EOS presented above. EOSs with $\lambda > \lambda_{\rm cr}$ display the instability region in their $M_{\rm B}(R_{\rm eq})$ and $J(\Omega)$ relations. In the left panel of Fig. 4.11, I show the difference between $\lambda_{\rm cr} - \lambda$ for stable BB EOSs as a function of the spin frequency $\Omega_{\rm on}$ at which the onset of BB occurs. The plot was produced for three different polytropes $\gamma_{\rm N} = 2,\ 2.25$ and 2.5, $\gamma_{\rm S} \geqslant \gamma_{\rm N}$ (e.g. for $\gamma_{\rm N} = 2$ I have chosen $\gamma_{\rm S} = 2,\ 2.25$ and 2.5), and many λ parameters ($\lambda < \lambda_{\rm cr}$). The relation presented here can be parametrized as function of $\Omega^2_{\rm on}$. The right panel in Fig. 4.11 shows the $M_{\rm B}^{\rm on,cr} - M_{\rm B}^{\rm on}$ difference

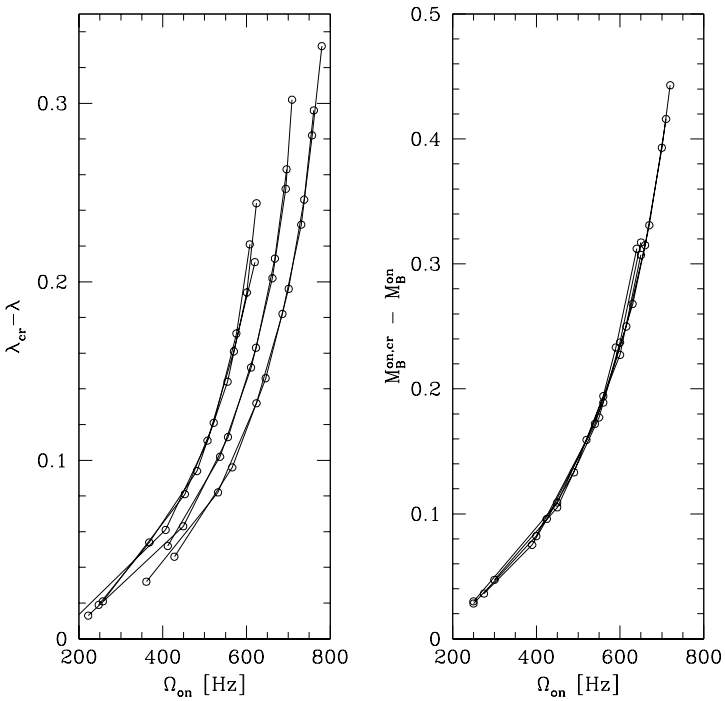

Figure 4.11: Left panel: departure from the critical density jump $\lambda_{\rm cr} - \lambda$ as a function of BB onset spin frequency $\Omega_{\rm on}$ for a set of constant-pressure phase transition EOSs. Different branches correspond to polytropic EOSs with $\gamma_{\rm N} = 2,\ 2.25,\ 2.5$ (from left to right) connected by a λ density-jump with $\gamma_{\rm S}$ polytropes ($\gamma_{\rm N} \leqslant \gamma_{\rm S}$ e.g. for $\gamma_{\rm N} = 2$ $\gamma_{\rm S}$ was equal 2, 2.25 and 2.5). The $\lambda_{\rm cr}$ parameter corresponds to the marginally stable BB. Right panel: mass increase $M_{\rm B}^{\rm on,cr} - M_{\rm B}^{\rm on}$ needed for the onset of BB versus the onset frequency $\Omega_{\rm on}$ ($M_{\rm B}^{\rm on,cr} = M_{\rm B}^{\rm on}(\Omega = 0)$ i.e. for the marginally stable BB).

for different density jumps λ as a function of $\Omega_{\rm on}$. The critical onset mass $M_{\rm B}^{\rm on,cr}$ correspond to the marginally stable EOS for which BB occurs at any spin frequency. Again, the increase of mass can be described by polynomial function of $\Omega_{\rm on}^2$.

As an example of a realistic EOS showing the BB phenomenon for spinning down pulsars, I will consider an EOS softened by the appearance of hyperons. The EOS was calculated by Balberg and Gal (1997) and discussed by Balberg et al. (1999) (EoS 2 $N\Lambda\Xi$ in their notation). In Fig. 4.12 this EOS (denoted by NH) is presented, along with the purely nucleon EOS (denoted by N), for which the appearance of hyperons was suppressed. The NH EOS is based on phenomenological effective interactions between nucleons and hyperons – as we see, the presence of hyperons around $\sim 7 \times 10^{14}$ g/cm^3 softens the

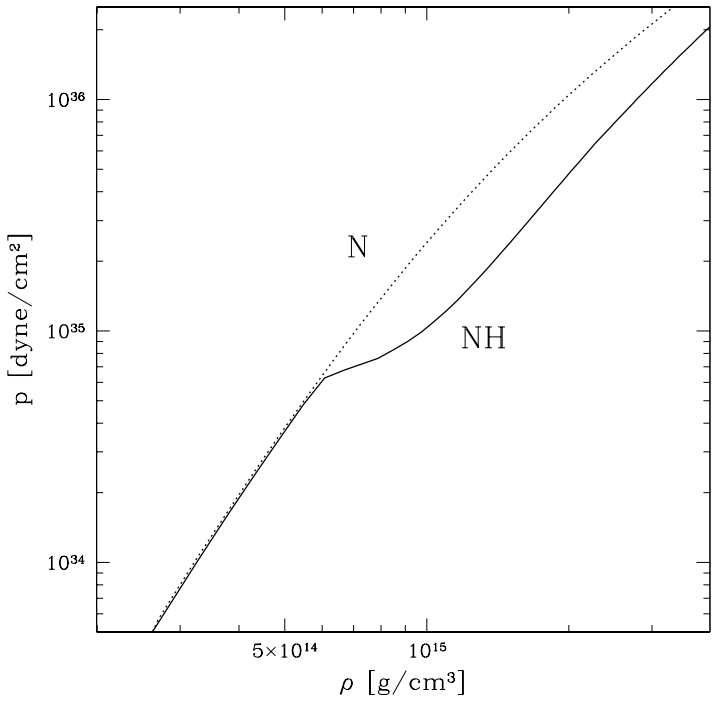

Figure 4.12: Pressure P versus mass density ρ for the NH EOS (EoS2 $N\Lambda\Xi$ of Balberg et al. 1999), denoted by a solid line, softened around $\rho \sim 7 \times 10^{14}$ g/cm^3 by the presence of hyperons, and purely nucleon dense matter N EOS (EoS2 N of Balberg et al. 1999) obtained by the suppression of hyperons (dotted line).

N EOS considerably. The value of the maximal mass for the non-rotating NH EOS configuration is equal to $M_{\rm B}^{\rm stat} = 2.05\ M_\odot$, to be compared with $M_{\rm B}^{\rm stat} = 3.01\ M_\odot$ in the case of N EOS (maximal allowable gravitational masses are equal to $M^{\rm stat} = 1.82\ M_\odot$ and $M^{\rm stat} = 2.48\ M_\odot$, respectively).

Figs. 4.13 show the $M_{\rm B}(R_{\rm eq})$ and $J(\Omega)$ relations. The BB feature appears for stars with baryon mass greater than $M_{\rm B}^{\rm on} = 1.91\ M_\odot$ and for $\Omega \geqslant \Omega_{\rm on} = 800$ Hz (unfortunately, for spin frequencies which had still not been observed at the time of writing this text). All other features, i.e. spin-up before the instability point or a continuous spin-up for stars with masses greater than $M_{\rm B}^{\rm sup}$ (here $M_{\rm B}^{\rm sup} = 2.17\ M_\odot$ and corresponding $\Omega_{\rm sup} = 1320$ Hz), are qualitatively the same as for the polytropic EOSs examples presented before.

As the examples presented above show, the BB phenomenon is not necessarily a signature of a specific phase transition, or an appearance of specific form of dense matter, but a feature of *any* suitably softened EOS. Moreover, the

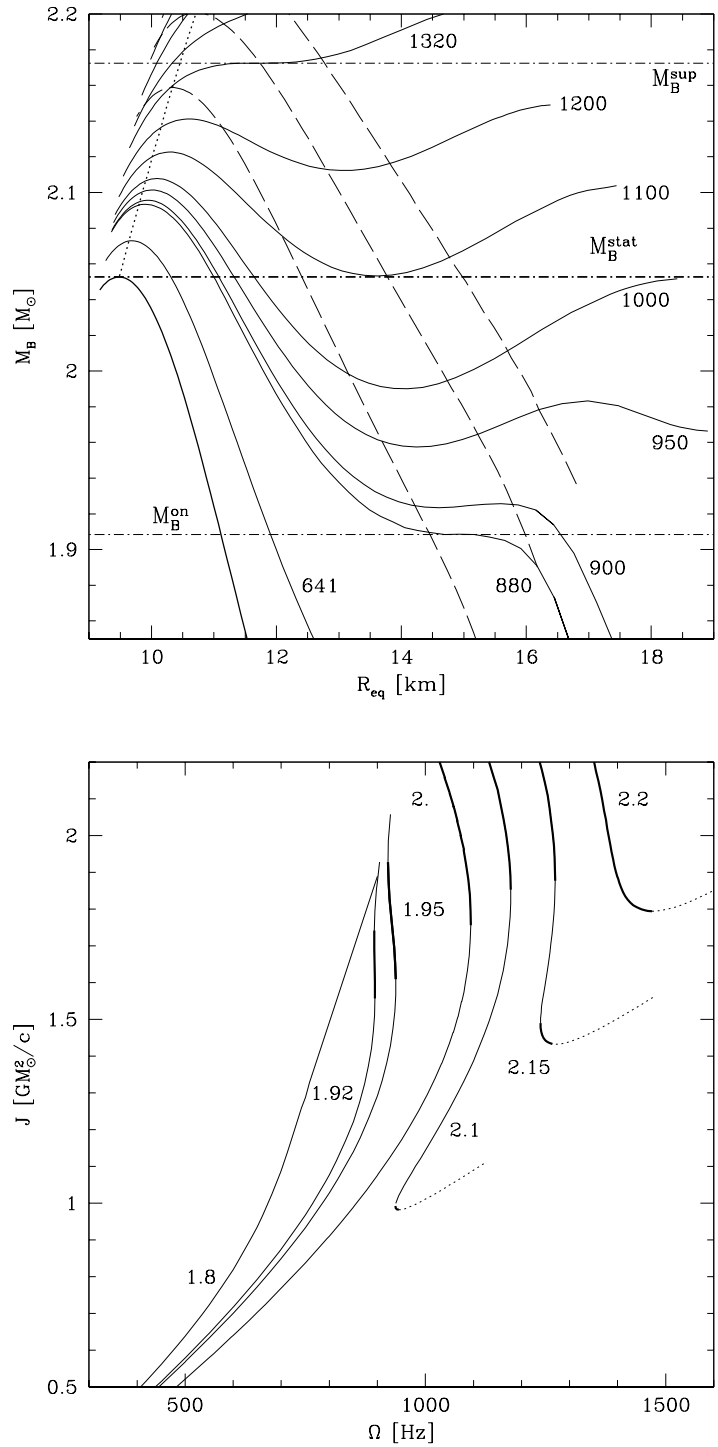

Figure 4.13: Spin-down and back-bending phenomenon for the NH EOS in the $M_{\rm B}(R_{\rm eq})$ (upper panel) and $J(\Omega)$ (lower panel) planes. Lines are marked as in previous plots. The BB phenomenon is present for $M_{\rm B} > M_{\rm B}^{\rm on} = 1.91\ M_\odot$ and for spin frequencies greater than $\Omega_{\rm on} > 800$ Hz (unfortunately, such spin frequencies have still not been observed at this time).

characteristic frequency range of BB strongly depends on the NS mass and EOS. Nevertheless, if observed in the future, the BB phenomenon will certainly influence on our knowledge of the dense matter physics.

4.2 Accreting stars with phase transitions

Phase transitions could occur in accreting NSs, because those stars can gain mass and thus may become sufficiently dense in their interior. A certain observational signature of the appearance of a new phase, called "spin-clustering" – the clustering of spin frequencies of accreting stars around some value of frequency, which should be noticeable in the observational data – was proposed by Glendenning and Weber (2001b,a). The problem is in some sense similar to the one discussed in the previous section, but instead of spin-down, spin-up will be studied here. The difference is introduced by the presence of accretion, that is the additional gain of mass during the transfer of angular momentum. Using the polytropic EOSs presented earlier, I will give examples of possible signatures of phase transitions in spinning up accreting NSs, and thus outline the differences between them and the characteristic features in the case of spinning down pulsars.

We shall assume that the evolution of an accreting NS can be well represented by a sequence of stationary rotating configurations with increasing $M_{\rm B}$. The assumptions are as follows: accreting matter orbiting on circular orbits falls from an accretion disk onto the equator of a NS and transfers its mass and angular momentum to the NS. The influence of the magnetic field on the disk itself will be neglected. I assume that the magnetic field is not very strong – smaller than 10^{10} G – and that it does not influence the inner edge of the accretion disk. Due to viscous processes in the disk, the particles lose their angular momentum and gradually approach the surface of the NS. Their motion is stable against small perturbations on circular orbits with radii larger than the marginally stable orbit (MSO) radius, $r_{\rm ms}$. If the NS equatorial radius $R_{\rm eq}$ is smaller than $r_{\rm ms}$, the particles fall dynamically from the inner edge of the disk ($r = r_{\rm ms}$) onto the surface of NS, according to the prescription by Zdunik et al. (2002). If, however, $r_{\rm ms} < R_{\rm eq}$, the inner edge of the accretion disk is defined by the surface of NS: viscous processes transport the particles

together with their angular momentum directly onto the star. Summarizing, in the first case the innermost stable circular orbit (ISCO) is $r_{\rm ms}$ and in the second case – $R_{\rm eq}$.

Using the equations of orbital motion derived by Zdunik et al. (2002), one can calculate the value of the specific angular momentum $l_{\rm IS}$ of a particle orbiting NS at the ISCO orbit, and then infalling onto the NS. The accretion of a small amount of mass $\mathrm{d}M_{\rm B}$ results in the following relation between NS mass $M_{\rm B}$ and angular momentum J:

$$\mathrm{d}J = x_l l_{\rm IS}\ \mathrm{d}M_{\rm B}\ , \tag{4.5}$$

where x_l denotes the fraction of the angular momentum of the matter element transferred to the star. The rest of the angular momentum, $1 - x_l$ is lost by various dissipative processes like radiation, interaction with magnetized plasma, or viscous processes in the case of $r_{\rm ISCO} = R_{\rm eq}$. The change of J is roughly proportional to the accreted mass, $\dot{M}_{\rm B} \times t$, because during accretion the value of $l_{\rm IS}$ is approximately constant (of course, provided that $\dot{M}_{\rm B} \times t \ll M_{\rm B}$).

The numerical simulations of accretion were performed as follows: initially non-rotating configurations with different masses were gaining mass and angular momentum according to Eq. (4.5), and their history was tracked up to the Keplerian velocity or the axisymmetric instability limit. During the calculations it became evident that the accretion *strongly suppresses* the BB phenomenon. To better visualize the effect of mass and angular momentum transfer, I will present examples of the MSt and MM EOS in the extreme case when *all* the angular momentum of the infalling particles is transfered onto the star without dissipation i.e. $x_l = 1$. This case is the most favorable situation for the appearance of BB. This setting is also most similar to the non-physical example of spinning up the star without the mass transfer from the previous section, because the amount of the angular momentum per accreted mass is the largest.

For the stable BB (MSt EOS) accretion of mass and angular momentum with 100% efficiency completely supresses the BB features – see Figs. 4.14 for the $M_{\rm B}(R_{\rm eq})$ and $J(\Omega)$ plots – this is because the increase of mass is too big compared to the increase of angular momentum. Stars end their spin-up period at the Keplerian velocity without the BB feature. We can imagine the non-

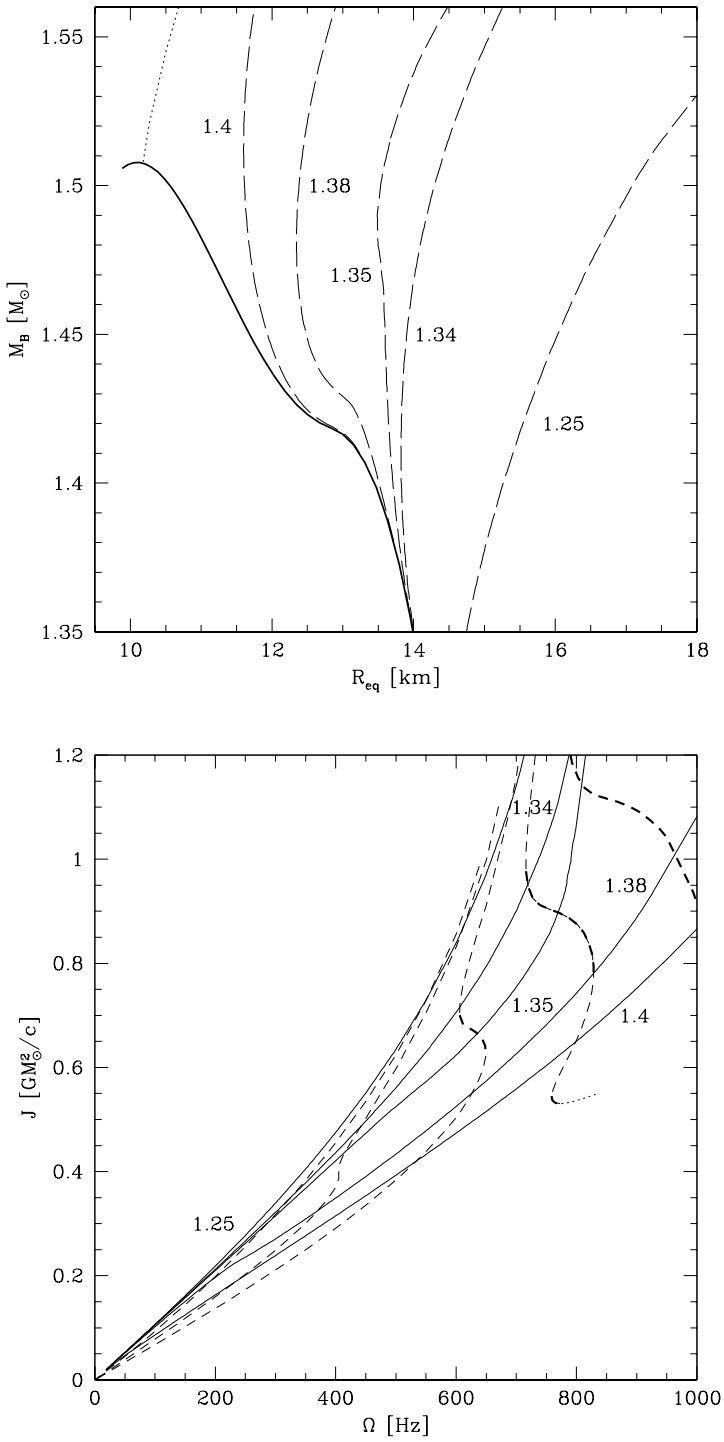

Figure 4.14: Spin-up of accreting NSs with MSt EOS. The upper panel presents the $M_{\rm B}(R_{\rm eq})$ relation – the solid curve denotes the non-rotating configuration (the same as in Fig. 4.4), whereas the dashed curves represent accreting sequences, with increasing mass and angular momentum. The labels denote baryon masses of non-rotating configurations. The lower panel shows the $J(\Omega)$ relation – as we see, the BB phenomenon is absent. All presented configurations are spun up to the Keplerian velocity. Labels denote starting baryon masses i.e. baryon masses at $\Omega = 0$. Dashed curves are taken from Fig. 4.5 for comparison.

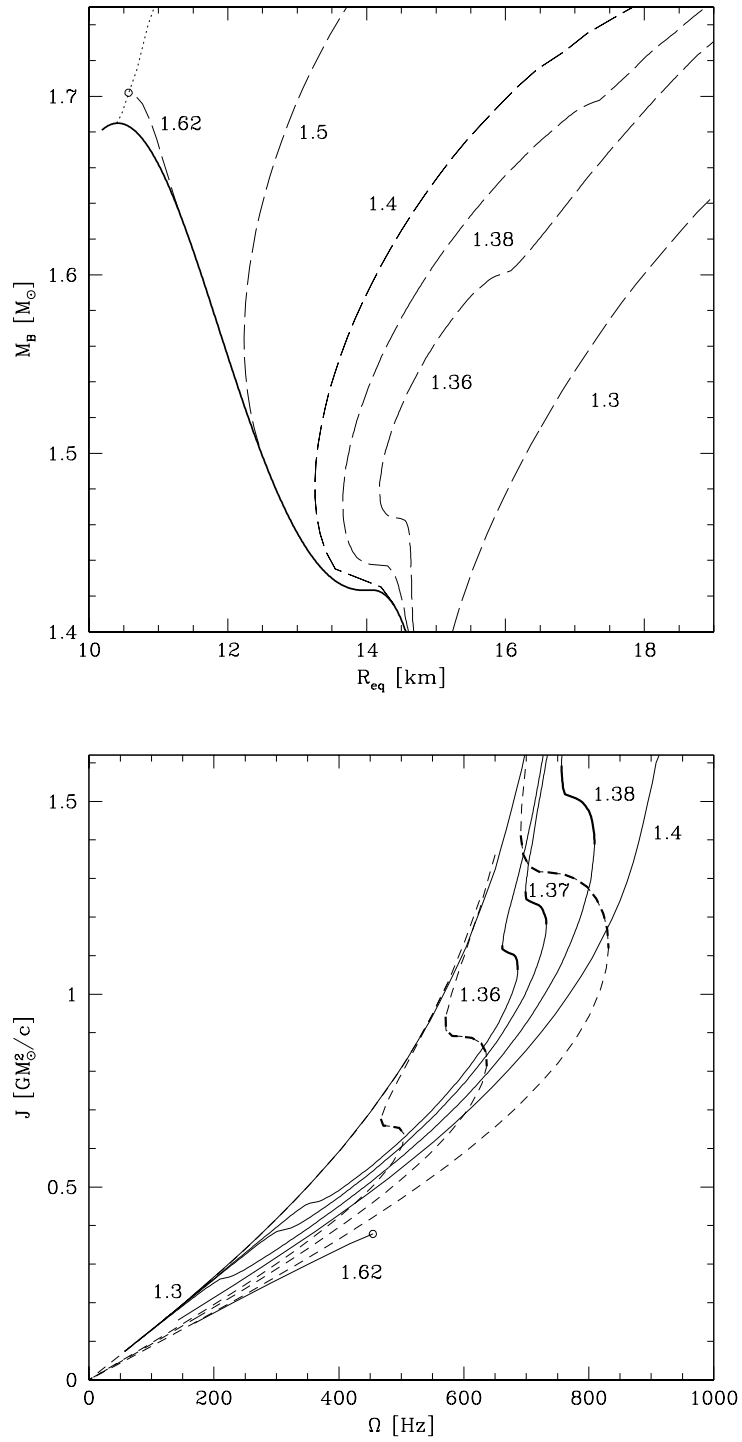

Figure 4.15: Spin-up of accreting NSs with MM EOS. The lines are marked as in previous plots. Upper panel: the $M_{\rm B}(R_{\rm eq})$ relation (labels denote the baryon masses of non-rotating configurations). Lower panel: the $J(\Omega)$ relation. In this case we obtain the BB phenomenon, although strongly decreased as compared with a constant $M_{\rm B}$ cases (dashed lines were taken from Fig. 4.10).

physical situation when $x_l > 1$: with this assumption one is able to recover all the features of BB, while still using MSt EOS (of course, in the abstract situation where $x_l \to \infty$ – spinning up without accretion of matter – one recovers the results from Sect. 4.1).

In Fig. 4.15 the results for the marginally stable MM EOS are presented. As we see, the BB signature is present, although much suppressed compared to the case of a spin-down of isolated NSs. For higher starting masses (which on the upper panel in Fig. 4.15 correspond to dashed curves on the left-hand side) the evolution is more-or-less similar to the non-accreting case. If, however, the starting mass is small enough e.g. the 1.3 $M_\odot$ in Figs. 4.15, the star will never produce the BB phenomenon. The situation is in a sense similar to the spin-down results from the previous section: here the star will be spun up to the Keplerian velocity without going through the central densities corresponding to BB.

The results for the unstable MUn EOS are qualitatively the same as during spin down simulations – the region of instability persists during the accretion and we can expect "twin" transitions, as presented before. The case of the realistic NH EOS used as an example in the previous section demonstrates that the effect of accretion on the BB signatures is very strong, see Figs. 4.16 for the $M_{\rm B}(R_{\rm eq})$ and $J(\Omega)$ relations. No BB features are observed – stars are spun up to the Keplerian velocity for smaller starting masses, or to the axisymmetric perturbation instability limit in the case of larger starting masses.

Concluding, in the case of accreting NSs the increase of angular momentum J is necessarily accompanied with the transfer of mass and the increase of $M_{\rm B}$. This condition weakens the influence of rotation on the structure of a star due to the enhanced role of gravitation. Thus, accretion of mass and angular momentum strongly suppresses the BB phenomenon. It is however not impossible, that for an EOS with very strong softening the BB features would be visible, if not too large a fraction of the transfered angular momentum were lost due to various dissipative processes during accretion.

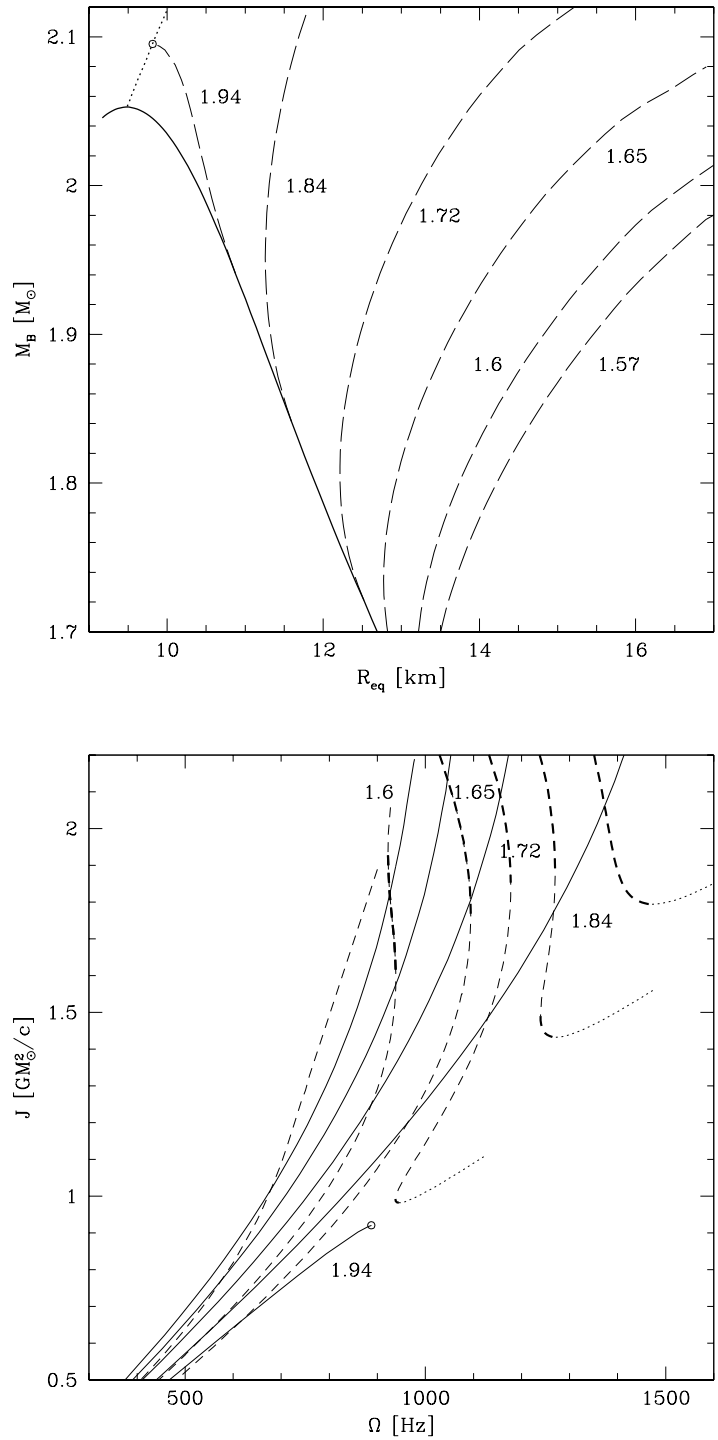

Figure 4.16: Spin-up of accreting NS with realistic NH EOS from previous section. The spin-up by accretion occurs at maximal efficiency: $x_l = 1$. Upper panel: $M_{\rm B}(R_{\rm eq})$ relation. Lower panel: $J(\Omega)$ relation. Open dot marks the end of sequence at the instability line. The numbers mark the starting baryon masses of configurations. As shown, the BB phenomenon is absent.

4.3 Conclusions and remarks

The back-bending phenomenon is a very subtle and non-trivial feature of rotating stars built with an EOS which exhibits the softening due to phase transition. I have shown that, in principle, with the use of parametric EOSs one is able to obtain BB for frequencies in the observable pulsar frequency range (i.e. up to $\simeq 641$ Hz). The mixed-phase segments and the density jumps between pure phases in my polytropic EOSs have parameters comparable with those exhibited by the realistic EOSs. Contrary to the polytropic EOSs however, the example realistic EOS softened by the appearance of hyperons reveals spin-up by angular momentum loss for spin frequencies higher than those ever observed in pulsar timing. Incorporation of accretion of matter into the calculations of the spinning up NSs strongly suppresses the BB features. At this time, it seems that putting constraints on dense matter physics from the observations of BB is a difficult task, because of the lack of direct observations of the BB features. From the point of view of the EOS, the attributes presented in previous sections demand a delicate balance between the stiffness of the appearing phase and its extent in the density. The new mixed phase cannot be too stiff compared to the already existing phase N, and should extend far enough in the density (in the case of constant-pressure phase transitions, the density jump cannot be too small), otherwise the influence of the EOS will not be sufficient to produce BB. Also, the S phase should in addition be sufficiently stiff to ensure that the configuration will not end at the instability limit immediately after the phase transition.

Fast-rotating pulsars can be created during their birth in supernova explosions – the famous Crab pulsar was born with ~ 19 ms period. Such pulsars strongly interact with the surrounding interstellar medium, so their spin frequency decreases fast. After about 1000 years, the Crab pulsar rotation rate is ~ 33 ms. As an example, I will present the relation between the spin frequency and time, which was calculated according to Spyrou and Stergioulas (2002) using the relation

$$c^2 \frac{\mathrm{d}M}{\mathrm{d}t} = \kappa \Omega^{\alpha} \ , \tag{4.6}$$

where M is the total mass-energy of the star and $\alpha = n + 1$ (braking index is equal $n = 3$ for magnetic dipole braking). We will assume that the κ parameter

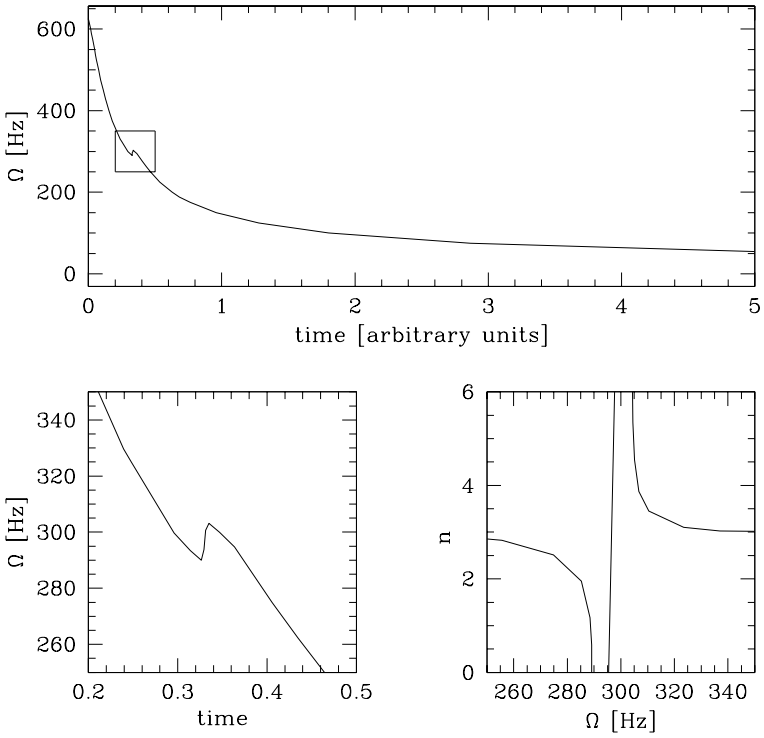

Figure 4.17: The BB phenomenon for a 1.45 $M_\odot$ MM EOS star. Upper panel: the spin frequency Ω as a function of time (in arbitrary units, which depends on the parameter κ from Eq. 4.6). The BB feature is placed at 300 Hz. Left lower panel: zoom of the small box presented above. Right lower panel: behavior of the braking index n as a function of the spin frequency Ω.

is constant during the evolution. As shown in Fig. 4.17 for a 1.45 $M_\odot$ MM EOS star the spin frequency decreases most rapidly at the beginning of pulsars life. When compared with $J(\Omega)$ plot (Fig. 4.10) the BB feature at around 300 Hz seems somewhat less pronounced. It is most probable for BB to occur at the beginning of a pulsar's life, when the central parameters, like the central pressure P_c or the central density ρ_c, increase faster and to a greater extent. The typical lifetime of such radio-pulsars is about 10^7 years. After this phase, its magnetic field is too weak to produce radio pulses – the NS becomes radio quiet. There is, however, the possibility of "recycling" such radio-quiet NSs – old NSs can become radio-pulsars again if spun up by accretion processes. Such revitalized millisecond pulsars are observed as single radio-pulsars and members of binary systems. Their lifetime, 10^9 years, is much longer than that of ordinary radio-pulsars. Their weak magnetic field ($10^8 - 10^9$ G) does not

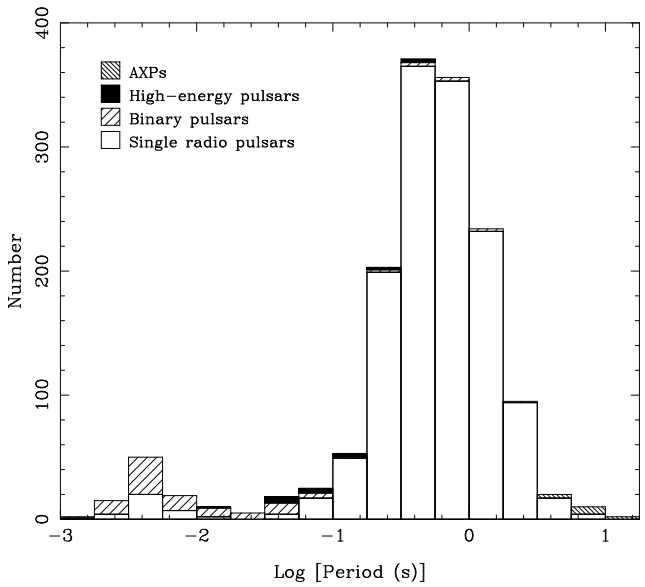

Figure 4.18: Histogram of spin periods for all known pulsars (from Manchester et al. 2004; AXP acronym means the Anomalous X-ray Pulsars).

interact strongly with interstellar matter, so the corresponding spin down rate is very small; thus the central parameters (the pressure $P_{\rm c}$, the density $\rho_{\rm c}$) also change slowly. We know now of about 100 millisecond pulsars, however the current observational evidence of BB is rather pessimistic. There are several pulsars with $\dot{\Omega} > 0$, but they are located in globular clusters and most probably the apparent spin-up effect is related to their motion in the gravitational field of the star cluster.

Nevertheless, several possible signatures of BB have been discussed in the literature: a drastic change of the frequency derivatives in the timing of a solitary pulsar ($\dot{\Omega} > 0$, or uncommonly high or low braking index), the "spin-clustering" of frequency spins around some value, as well as the discrepancies between the age of a young pulsar and its host supernova remnant.

The "spin-clustering" feature for accreting NSs was originally proposed by Glendenning and Weber (2001b,a). The authors obtained, for a sample EOS, the clustering of spin frequencies in a narrow band of spins around 200 Hz, whereas the observational data presented by them suggested that the peak is around 400 Hz. In Fig. 4.18 I reproduce the recent data on spin periods of all known pulsars (Manchester et al., 2004). As we see, in the millisecond range there is a small peak at about 300 Hz. As shown in Fig. 4.18 the

data from the Australia Telescope National Facility (ATNF), currently the biggest radio pulsar survey, have been supplied by a collection of spin frequencies from non radio-pulsars, e.g. those in low-mass X-ray binaries (LMXB). There are 18 LMXBs, in which one can in principle measure the spin frequency (Chakrabarty, 2004; Chakrabarty et al., 2003). Those spin frequencies obtained from the difference between the upper and lower quasi-periodic oscillations frequencies, or from the periodic modulation of X-ray bursts, seem to cluster around 300 Hz. It is, however, difficult to decide on the origin of this peak. Note also that the BB signature is very sensitive to the mass of the star – we should suspect that accreting NSs have a large spectrum of masses. The inclusion of different masses of the accreting stars will strongly smear the theoretical clustering peak.

Another proposed way of finding the signature of a phase transition in rotating NSs is to observe pulsars in supernova remnants, paying the special attention paid to the discrepancies between their ages, or peculiarities in the age of a pulsar. An example presented by Spyrou and Stergioulas (2002) is PSR J0537-6910, a 16 ms Crab-like pulsar discovered by Marshall et al. (1998) in the Large Magellanic Cloud. Its period and the period derivative suggest, that if the canonical magnetic dipole value $n = 3$ for the braking index is accepted, the pulsar should be born with a sub-millisecond period – a highly unlikely situation. The solution to the conundrum is a temporary spin-up era, in which the pulsar would spend some of its life while keeping its high spin frequency. Another solution is of course $n < 3$ – unfortunately, until now the braking index has not been measured, and one cannot judge whether the discrepancy is due to BB or a magnetic dipole braking mechanism other than the canonical $n = 3$.

In conclusion, the BB phenomenon seems to be difficult to detect in both spinning down solitary pulsars and accreting NSs. The characteristic frequencies, at which a particular star spends the BB stage, depend strongly on the EOS of dense matter. It was also demonstrated that the accretion processes suppress the BB features. Nevertheless, if BB was detected, it should provide us with important informations about the phase transitions occurring in matter at densities larger than the nuclear density.

Chapter 5

Influence of realistic EOS of dense matter on the last stage of NS binary inspiral

In the present chapter I will focus on those properties of NSs with realistic EOSs which can be detected through observations of gravitational waves using ground-based laser interferometers, such as VIRGO (Acernese et al., 2004), LIGO (Abbott et al., 2004), GEO600 (Hewitson et al., 2003) or TAMA300 (Ando et al., 2001). Those instruments will provide us, hopefully within the next few years, with gravitational wave (GW) data – information which will allow us to explore various astrophysical objects. Among the most promising sources to be observed by the ground-based interferometers in their operating range around $\simeq 1$ kHz are close NSs binary systems (NS–NS). I will present calculations for the canonical "binary NS system" of two 1.35 $M_\odot$ stars. If we assume that the distance between the stars' centers is twice the canonical radius, $r = 2R \sim 20$ km, and the canonical sum of masses is $M_1 + M_2 \sim 3\ M_\odot$, and recall that gravitational waves are emitted mostly at twice the orbital frequency, we can get the desired $\simeq 1$ kHz frequency from a simple estimation using Kepler's law:

$$\Omega^2 = G(M_1 + M_2)/r^3, \tag{5.1}$$

where Ω is the orbital frequency. Hopefully, a received signal will be rich in the signatures of the poorly known physics of NS interiors. Specifically, the susceptibility of the star to be tidal deformation in the gravitational field of a rotating system should depend on the EOS of dense matter, because the last

few orbits before the merger phase (also called the plunge) are dominated by strong tidal forces acting between the components. It was shown by Faber et al. (2002) and Taniguchi and Gourgoulhon (2003) that the final frequency at the last stable circular orbit is correlated with the compactness parameter $M/R \equiv GM/Rc^2$. Also, we know how to observationally resolve, using statistical techniques and post-Newtonian expansions, the masses of the system components. Measurement of M/R can then be used for estimation of the NS radii, and thus will provide us with strict constraints on the theory of matter above the nuclear saturation density. Moreover, the precise location of the last stable orbit is crucial for realistic computations of the dynamical merger phase (see e.g., Shibata et al., 2003) – such calculations require *initial data* sets in order to be successful. The present work provides such data.

The last orbits of the inspiral phase of binary NSs systems were studied using the so-called quasi-equilibrium approximation in the framework of the Isenberg-Wilson-Mathews (IWM) approximation of General Relativity. We will assume that the timescale of orbital evolution is much longer than the orbital period of the system. Therefore, the evolution of the system can be modeled by a sequence of *exactly circular* orbits. As was described in Chapter 2, the IWM approximation reduces the problem to a solution of only five of the ten Einstein equations, by demanding that the spatial metric be conformally flat. Within these approximations, two special cases are possible: the *corrotational* case, when the stars rotate in a synchronized manner like the Earth-Moon system, and the *irrotational* case, which is somewhat more realistic because, at the latest stages of inspiral, viscous forces are to weak to provide synchronization between the system components. The latter case will be presented.

The difficult part of the study is the proper treatment of the realistic EOS of matter. In the past, calculations were performed for polytropic EOSs only, by Bonazzola et al. (1999a); Gourgoulhon et al. (2001); Taniguchi and Gourgoulhon (2002a, 2003) with the use of the `LORENE` codes, and e.g. by Uryū and Eriguchi (2000); Uryū et al. (2000); Marronetti et al. (1999) using other methods. Recently, Oechslin et al. (2004) computed the quasi-equilibrium evolution of binary NSs composed of a pure nuclear matter EOS, based on a relativistic mean field model, as well as an EOS with a phase transition to quark matter

at high density. Unfortunately, those calculations cannot pretend to be *fully* realistic because of the crude treatment of the crust – at 2×10^{14} g/cm^{-3} the nuclear EOSs are matched with a polytrope with an adiabatic index $\gamma = 2.86$. As we know, in reality the EOS of the NS crust is much more complicated than a simple polytrope (see Fig. 1.2), in particular it is softer (its mean adiabatic index γ is much smaller), so in order to correctly determine the values of parameters at the last stable orbit of quasi-equilibrium evolution a realistic EOS of the crust must be employed.

As for the core, the binary NSs considered here will be composed of three *very different* dense matter EOSs: the BPAL12 EOS by Bombaci (1995) (see also Prakash et al. 1997), the APR EOS by Akmal et al. (1998) and the GNH3 EOS which was obtained by Glendenning (1985, model 3). Those EOSs, combined with the realistic EOS of the NS crust allowed me to obtain predictions for future observational analysis and *realistic initial data* for the merger calculations. It will be assumed that the matter behaves as an ideal degenerate fluid, described by a zero-temperature EOS. Despite the fact that the dissipative and thermal effects accompanying matter flow inside NSs lead to specific physical phenomena, e.g. breaking of the β-equilibrium between baryons and leptons, thus producing enhanced neutrino flux (Haensel, 1992), I will neglect these effects, as they are expected to be negligible for most of the inspiral stage.

This chapter contains the following sections: Sect. 5.1 presents the physical conditions and recalls the methods used to obtain the quasi-equilibrium orbital sequences (see also Sect. 2.2 for numerical methods), Sect. 5.2 describes the EOSs used in the calculations; whereas Sect. 5.3 contains the results. Sect. 5.4 contains conclusions and remarks.

5.1 Numerical methods

As mentioned in Sect. 2.2, the results can be obtained by numerically solving five coupled, nonlinear, elliptic equations for the gravitational field, supplemented by an elliptic equation for the velocity potential of irrotational flows. The method benefits from the assumption of a quasi-equilibrium state (helical Killing vector approximation) with the irrotational flow of the fluid, and a

conformally flat spatial 3-metric (the IWM approximation).

The numerical technique relies on a multi-domain spectral method with surface-fitted coordinates. One domain for each star's interior was used; for the surrounding space from 3 to 4 domains were assigned, depending on the stars' separation (a smaller number of domains in the case of a small separation). In each domain, the number of collocation points of the spectral method was chosen to be 25, 17 and 16 in radial r, polar θ and azimuthal ϕ directions, respectively. Sect. 2.2 contains a description of the modifications implemented in the code in order to properly treat the tabulated realistic EOSs in the irrotational approximation.

The accuracy of the computed relativistic models was measured using a general relativistic generalization of the virial theorem (Gourgoulhon and Bonazzola 1994, see also Friedman et al. 2002 and Sec. III.A of Taniguchi and Gourgoulhon 2003). During computations, the relative virial error was typically a few times 10^{-5}.

5.2 Equations of state of dense matter

For NSs of mass $M = 1.35\ \mathrm{M}_\odot$ considered here, the part of the star which has density lower than the nucleon saturation density ρ_{nuc} contains about 2% of the stellar mass. This region is, however, the subject of the most pronounced stresses during tidal interactions with the gravitational field produced by the companion star. As described by Haensel (2001), elastic shear terms in the stress tensor are two orders of magnitude smaller than the main diagonal pressure term (shear modulus is about hundred times smaller than the compression modulus). I will neglect the possible melting of the crust due to the tidal interactions (it may be important in the merger phase, however). Thermal effects during the flow of matter in the interior of NSs are expected to be small at the quasi-equilibrium evolution stage. In summary, it is not a large over-simplification of the problem to treat the crust layers in the tidal force field as an ideal degenerate fluid (zero-temperature EOS).

In the outer crust, where the pressure is determined by an ultra-relativistic electron gas, we have $\gamma = 4/3$. The inner crust is composed of a lattice of

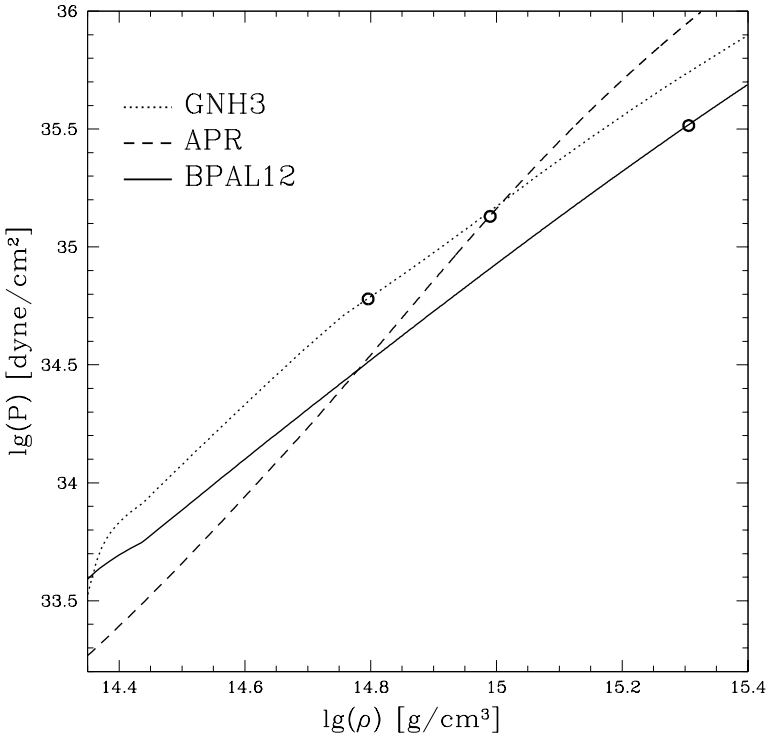

Figure 5.1: The pressure P as a function of the mass-energy density ρ for three EOSs of interest: APR (dashed line), GNH3 (dotted line), and BPAL12 (solid line). The circles correspond to the central parameters (the pressure and density) of a non-rotating stellar model with a gravitational mass equal to 1.35 $M_\odot$ (see Table 5.1).

heavy neutron-rich nuclei immersed in neutron and electron gas. The outer and inner crust consist of about 1% of the star's mass. The adiabatic index of such a mixture varies with density, from $\gamma \simeq 0.5$ near the neutron-drip point to $\gamma \simeq 1.6$ near $\rho_{\rm nuc}$ (Douchin and Haensel 2001, see Fig. 1.2 in Chapter 1 for details). The EOS of the crust used in calculations is composed of three segments. For densities smaller than 10^8 g/cm^3 the EOS by Baym et al. (1971) was used. For densities higher than 10^8 g/cm^3, but smaller than the neutron-drip density $\rho_{\rm nd}$, the EOS using the experimental masses of neutron-rich nuclei was employed (Haensel and Pichon, 1994). Finally, for densities larger than $\rho_{\rm nd}$, but smaller than $\rho_{\rm cc}$ (crust-core interface density), the EOS by Douchin and Haensel (2001) was used.

The EOS of matter denser than $\rho_{\rm nuc}$ is poorly known. There are several theories which use different approaches to the dense matter, some very exotic – they differ significantly at 10^{15} g/cm^3, characteristic of the central cores of

the NSs under study. Here I will concentrate on EOSs composed of nucleons (and in one case with the addition of hyperons). The interaction between nucleons are relatively well known from terrestrial experiments. Hyperons are much less studied, but the physics of their interaction with nucleons is certainly better understood than that of other exotic particles.

In order to demonstrate the freedom one has in choosing a description of the dense matter, three very different core EOSs will be considered. Two of them may be considered as soft and stiff extremes of the EOSs of matter composed of nucleons, electrons and muons. The first, the BPAL12 EOS by Bombaci (1995), is generally a very "soft" EOS, i.e. its adiabatic index γ is low; this EOS is based on a phenomenological model. The second, the APR EOS, is based on variational calculations and includes realistic two- and three-body nucleon interactions (Argonne A18 and Urbana UIX, respectively). The EOS was presented by Akmal et al. (1998). I also consider an EOS with a hyperonic degree of freedom by Glendenning (1985, model 3). In this EOS, hyperons are present at densities $\rho > 2\rho_{\rm nuc}$; it will be further called the GNH3 EOS. This EOS was obtained using the Relativistic Mean Field (RMF) model of baryonic matter. The nucleonic segment (for $\rho < 2\rho_{\rm nuc}$) is very stiff but the sound speed does not exceed the speed of light. The appearance of hyperons noticeably softens the EOS in comparison to the one composed only of nucleons.

The three EOSs are pictured in Fig. 5.1. They are indeed very different because of different strong interaction models at densities $\rho > \rho_{\rm nuc}$. The differences in stiffness reflect the characteristics of the nuclear model underlying each of the EOSs of the NS core. It is particularly easy to visualize these differences using the density-dependent adiabatic index γ, as pictured in Fig. 5.2. The strong drop (a softening) in γ above $\simeq 2\rho_{\rm nuc}$ is a clear sign of the appearance hyperons in the GNH3 EOS. For the APR EOS the value of the adiabatic index increases for densities higher than the crust-core interface density $\rho_{\rm cc}$, in contrast to the behavior of GNH3 EOS which softens close to this density. BPAL12 EOS has approximately constant adiabatic index in the core, $\gamma \simeq 2.2$, and because of that it is most similar to a polytropic EOS.

Since our main interest is oriented toward stars, it is worthwhile to compare the static configurations composed of these EOSs. Their features are shown in the form of mass-radius $M(R)$ relations in Fig. 5.3, where M is the gravitational

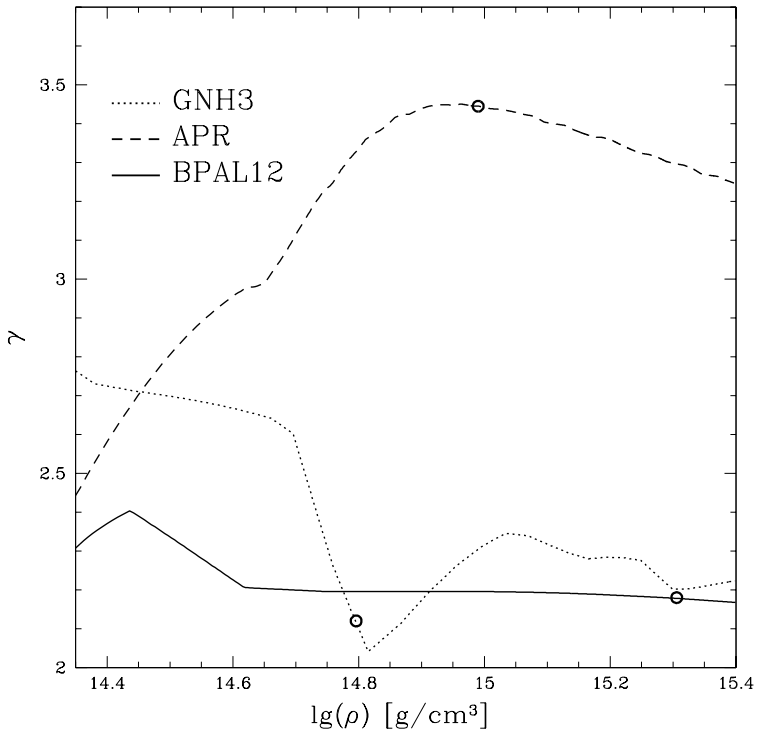

Figure 5.2: The adiabatic index γ against the energy density ρ for the EOSs used in computations: APR (dashed line), GNH3 (dotted line), and BPAL12 (solid line). Similar to Fig. 5.1 the circles correspond to the central parameters of a non-rotating stellar model with 1.35 $M_\odot$ gravitational mass.

mass and R is the coordinate radius of the star.

Because the BPAL12 EOS is relatively soft, it results in a very low maximum mass of $M_{\rm max} = 1.46$ M$_\odot$ (which is nevertheless marginally consistent with observations of the Hulse-Taylor pulsar). Due to its small radius it has the largest compactness parameter M/R. The APR EOS is stiffer, with much higher maximum mass, $M_{\rm max} = 2.2$ M$_\odot$. Although their $M(R)$ curves meet around $M \simeq 1.2\ M_\odot$, the physical properties of the two EOSs are then very different, as Fig. 5.2 shows. The GNH3 EOS has a maximum mass at $M \simeq 1.9$ M$_\odot$. At 1.35 $M_\odot$ its central density is slightly larger than the hyperon threshold density – the EOS at lower densities is is very stiff. Thus, the GNH3 EOS has the largest R and therefore the smallest M/R.

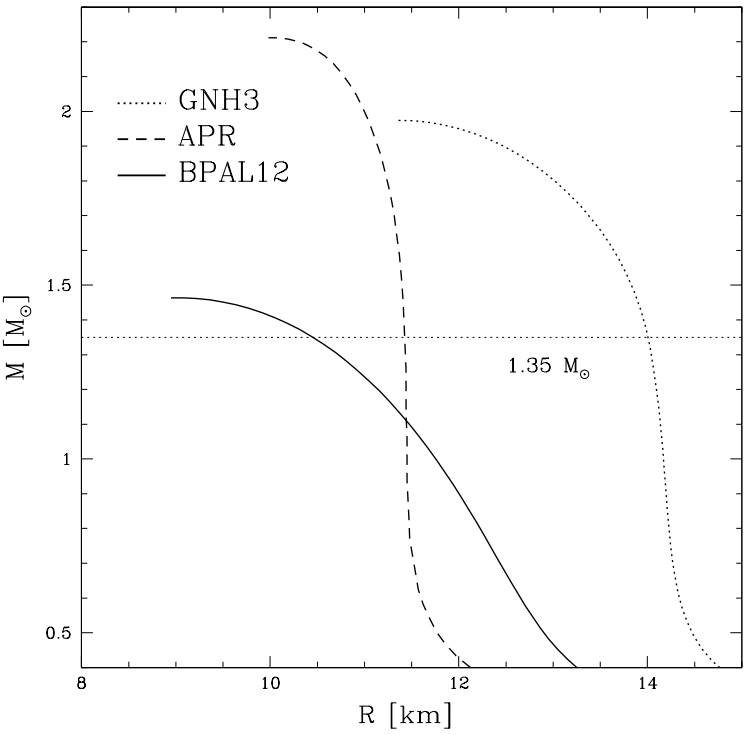

Figure 5.3: The gravitational mass M of static spherically symmetric isolated stars against its radius R for the APR (dashed line), GNH3 (dotted line) and BPAL12 (solid line) EOSs.

EOS	M/R	R [km]	$M_{\rm B}[M_\odot]$	ρ_c [10^{14} g/cm^3]
GNH3	0.140	14.262	1.45351	6.26
APR	0.176	11.350	1.49110	9.80
BPAL12	0.191	10.447	1.48472	20.22

Table 5.1: Properties of isolated non-rotating NSs of gravitational mass $M = 1.35\,M_\odot$ for the EOSs. The compactness parameter is denoted by $M/R \equiv GM/Rc^2$, R is the coordinate radius, $M_{\rm B}$ is the baryon mass and $\rho_{\rm c}$ is the central mass-energy density, respectively.

5.3 Results

A sequence of quasi-equilibrium configurations of decreasing separation d will approximate the evolution of the binary system driven by the loss of energy due to gravitational radiation. For each EOS, the binary system is composed of two equal-mass NSs with the baryon mass $M_{\rm B}$ corresponding to the gravitational mass $M = M_1 = M_2 = 1.35\ M_\odot$ for a static isolated star (or for the components of a binary system at infinite separation, see Table 5.1 for details).

The gravitational mass of $M = 1.35\ M_\odot$ was chosen for a reason: it agrees with very precisely measured "average NS mass" in relativistic NS–NS binary systems, in which an accurate timing of radio-pulsars is possible. Also, most of the calculations in the literature were obtained for this mass, therefore it seems suitable for future comparisons.

At infinite separation, the ADM mass of the system, Eqs. (2.45) and (2.46), is just a sum of the gravitational masses of isolated static stars; it will be denoted by M_∞:

$$\lim_{d\to\infty} M_{\rm ADM} = M_\infty := M_1 + M_2 = 2.7\ M_\odot\ . \tag{5.2}$$

The orbital binding energy will be then defined as

$$E_{\rm bind} := M_{\rm ADM} - M_\infty\ . \tag{5.3}$$

The variation of $E_{\rm bind}$ along an evolutionary sequence corresponds to the loss of energy via gravitational waves. Gravitational waves are emitted *mostly* as quadrupole radiation (this fact can be quantitatively explained by following the Newtonian mass-energy and angular momentum conservation laws for a binary point-mass system) at twice the orbital frequency, $\Omega_{\rm GW} = 2\Omega$. Each evolutionary sequence terminates either by a mass-shedding point (Roche lobe overflow), or by the instability point – a turning point (minimum) of $E_{\rm bind}$, which indicates an orbital instability (Friedman et al., 2002). This situation is also called the quasi-equilibrium innermost stable circular orbit (ISCO). The instability is a result of both relativistic effects and hydrodynamics: for sufficiently stiff EOS the instability exists also in the Newtonian regime (Taniguchi et al., 2001; Lai et al., 1994, 1993) in both corrotational and irrotational regimes. From the point of view of the EOS's stiffness, the turning point occurs for corrotational binaries with smaller γ, because of the additional energy term related to the degree of synchronization which increases the total equilibrium energy of the system. The instability is secular for corrotational systems and dynamical for irrotational ones, such as those considered here. One of those two scenarios, a mass-shedding or an instability turning point, marks the end of the existence of quasi-equilibrium configurations: in all cases considered here the sequences were terminated by mass-shedding. Dynamical calculations (Shibata and Uryū, 2001; Marronetti et al., 2004) prove that the

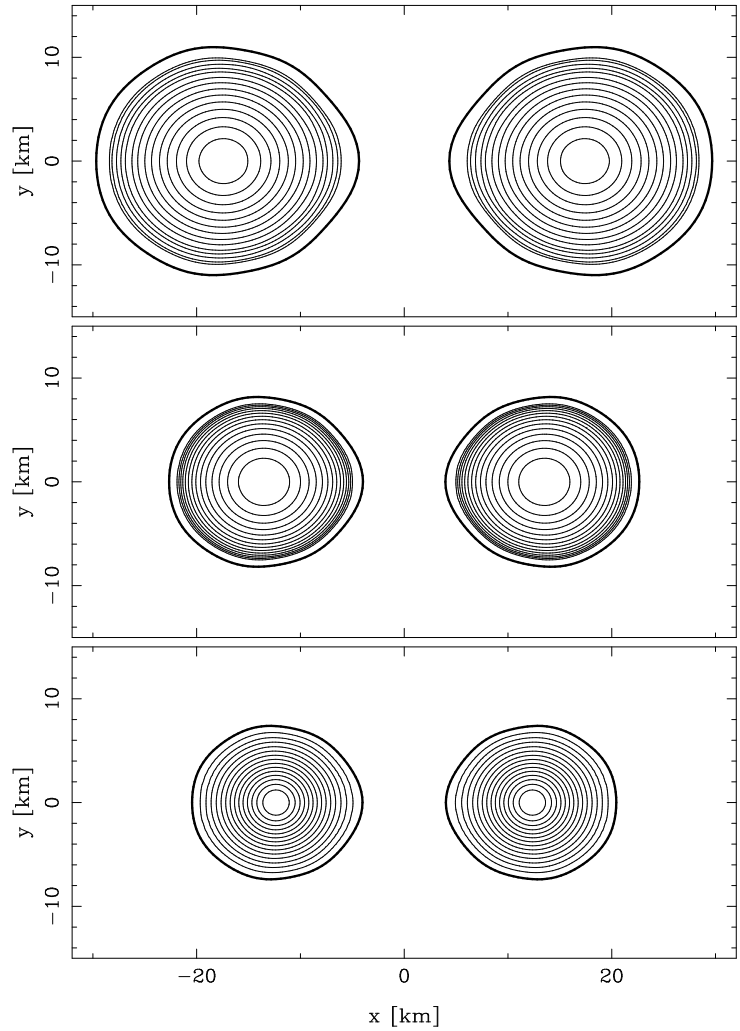

Figure 5.4: Baryon number density isocontours in the coordinate plane $z = 0$ (orbital plane) for configurations close to the mass-shedding limit. The upper (resp. middle, lower) panels correspond to the GNH3 (resp. APR, BPAL12) EOS. Thick solid lines denote stellar surfaces.

timescale to the final plunge is shorter than one orbital period for the configurations at the mass-shedding limit (the simulations were obtained for a polytropic EOS with $\gamma = 2$). The mass-shedding limit is therefore a true end of the inspiral phase, even if there is no turning point of $E_{\rm bind}$.

The mass-shedding is revealed by the formation of a cusp at the stellar surface in the direction of the companion NS. Because of the chosen numerical approach (spectral methods), it is impossible to produce a discontinuity at the surface – a "hint" of a cusp is visible in Fig. 5.4, where the star shapes in the orbital plane are presented at their last stable orbits, i.e. for the smallest

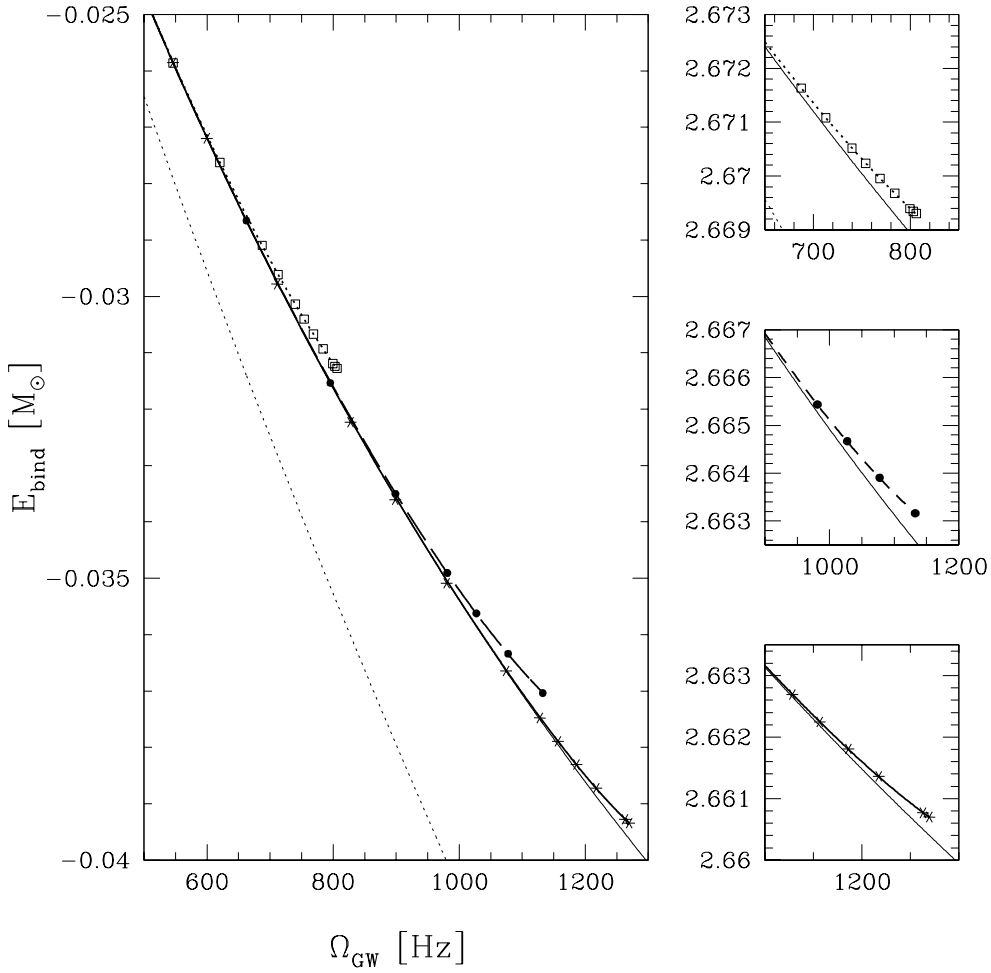

Figure 5.5: Large panel: the orbital binding energy $E_{\rm bind} = M_{\rm ADM} - M_\infty$ of the binary system versus the frequency of gravitational waves along three irrotational quasi-equilibrium sequences. The lines (dotted – GNH3, dashed – APR, solid – BPAL12) were plotted using fitted expressions (see text). The points represent actual data. The thin solid line is the 3PN post-Newtonian approximation for point masses by Blanchet (2002). The lower thin dotted curve corresponds to the Newtonian limit for point masses. Small panels: $M_{\rm ADM}$ versus the gravitational wave frequency for the GNH3, APR and BPAL12 EOSs (from top to bottom).

separations computed. The variation of the orbital binding energy along evolutionary sequences is presented in Fig. 5.5, where the points correspond to the equilibrium binary configurations calculated in numerical simulations (the last points for each EOS correspond to configurations presented in Fig. 5.4). The lines present the best fits (described below), as well as the expressions obtained for both Newtonian theory and the 3PN *post-Newtonian approxima-*

tion for point masses. The post-Newtonian expansions of General Relativity assume that the internal gravity of a source is small, and that relevant velocities v are much smaller than the speed of light, c. The expansion is performed in the powers of the small parameter, typically $(v/c)^2$; asymptotically, in the infinite order of expansion, the post-Newtonian approach should give the same results as General Relativity, while at the same time providing a "Newtonian intuition" and a better control of the underlying physics. The ISCO obtained for 3PN expansions is approximately at 2 kHz, much higher than the mass-shedding limits calculated here, which is obviously an artifact of the point-mass approach. The 3PN formula i.e., the expansion up to $(v/c)^6$ obtained by Blanchet (2002) for $E_{\rm bind}$ reads, in our case

$$\begin{aligned}\frac{E_{\rm bind}^{\rm 3PN}}{M_\infty} &= -\frac{1}{8}\,{\Omega_*}^{2/3} + \frac{37}{384}\,{\Omega_*}^{4/3} + \frac{1069}{3072}\,{\Omega_*}^{2} \\ &\quad + \frac{5}{3072}\left(41\pi^2 - \frac{285473}{864}\right){\Omega_*}^{8/3}\ ,\end{aligned} \tag{5.4}$$

where Ω_* is the orbital angular frequency written in geometrical units:

$$\Omega_* := 2\pi\frac{GM_\infty}{c^3}\Omega = 2\pi\frac{GM}{c^3}\Omega_{\rm GW}\ .$$

The prefactors of ${\Omega_*}^{2/3}$, ${\Omega_*}^{4/3}$, ${\Omega_*}^{2}$ and ${\Omega_*}^{8/3}$ in Eq. (5.4) are the Newtonian quadrupole, the 1PN, 2PN and 3PN term, respectively. Fig. 5.5 clearly shows that no turning point of $E_{\rm bind}$ occurs along the evolutionary sequences – there is no orbital instability prior to the mass-shedding limit. It is also shown, that when the purely Newtonian approach fails to reproduce the calculated results, the 3PN approximation reconstructs the data fairly well up to the frequency where the non-point mass effects start to be important. As was said earlier, the ISCOs are given here by the mass-shedding limit.

Two different approaches were used to fit the data for further computation of the GW energy spectrum. The first, similar to that presented by Faber et al. (2002), is based on quadratic approximation. The fitting was performed on the $E_{\rm bind} + k_{\rm N}\Omega_{\rm GW}^{2/3}$ function which constitutes the difference between the exact results obtained for $M_{\rm ADM}$ from Eq. (2.45), and the prediction of Newtonian theory, where $k_{\rm N} = (G\pi/4)^{2/3}M^{5/3} = 4.06\times10^{-4}\ M_\odot{\rm Hz}^{-2/3}$. It was sufficient to fit the results with a second order polynomial without the linear term

$$E_{\rm bind} = -k_{\rm N}\Omega_{\rm GW}^{2/3} + k_2\Omega_{\rm GW}^2, \tag{5.5}$$

EOS	k_2 $[10^{-9} M_\odot \, \mathrm{s}^2]$	a $[M_\odot]$	n
GNH3	6.23	$2.745\,10^{-3}$	8
APR	5.38	$1.912\,10^{-4}$	9
BPAL12	4.59	$6.519\,10^{-6}$	16

Table 5.2: Parameters of polynomial fits from Eq. (5.5) and Eq. (5.6).

contrary to Faber et al. (2002) – the linear term in their equation did not have a clear physical meaning, and was dropped.

The fitted coefficients k_2 responsible for the non-point mass hydrodynamical and tidal interactions are collected in Table 5.2. As was said, an accurate formula was needed for gravitational radiation in the region where it is effectively emitted – the fitting procedure was executed for frequencies higher than 500 Hz. This approximation works quite well for high frequencies, i.e. a small distance between the stars, without any need to introduce an additional linear term, as Faber et al. (2002) did.

It is possible to find a better approximation if one takes into account the higher order post-Newtonian expansions for the binding energy of point-mass systems. The effects of General Relativity and of finite sizes are pictured in Fig. 5.6. One can see that binary NS–NS systems are far from the Newtonian and 1PN approximations. On the contrary, the 2PN and 3PN results by Blanchet (2002) and the similar 3PN Effective One Body theory (EOB) results by Damour et al. (2000) are very close to our numerical results for a wide range of frequencies, even despite the fact that these theories were constructed for point-mass systems. Fig. 5.7 shows the difference between numerical points and the 3PN approximation given by Eq. (5.4) – the obtained fits approximate the behavior of a binary system of realistic NSs for a very large range of binary periods. They are represented by a power-law dependence on the Ω_{GW} frequency:

$$E_{\mathrm{bind}} - E_{\mathrm{bind}}^{\mathrm{3PN}} = a \left(\frac{\Omega_{\mathrm{GW}}}{1000 \text{ Hz}} \right)^n \tag{5.6}$$

The fits provide us with information about the frequencies Ω_{npm} at which the deviation from point-mass behavior becomes important. Approximate values of $\Omega_{\mathrm{npm}} \pm 50$ Hz for the three considered EOSs are given in Table 5.2. Due to the steep rise of $E_{\mathrm{bind}} - E_{\mathrm{bind}}^{\mathrm{3PN}}$ the power n is quite large. An integer value

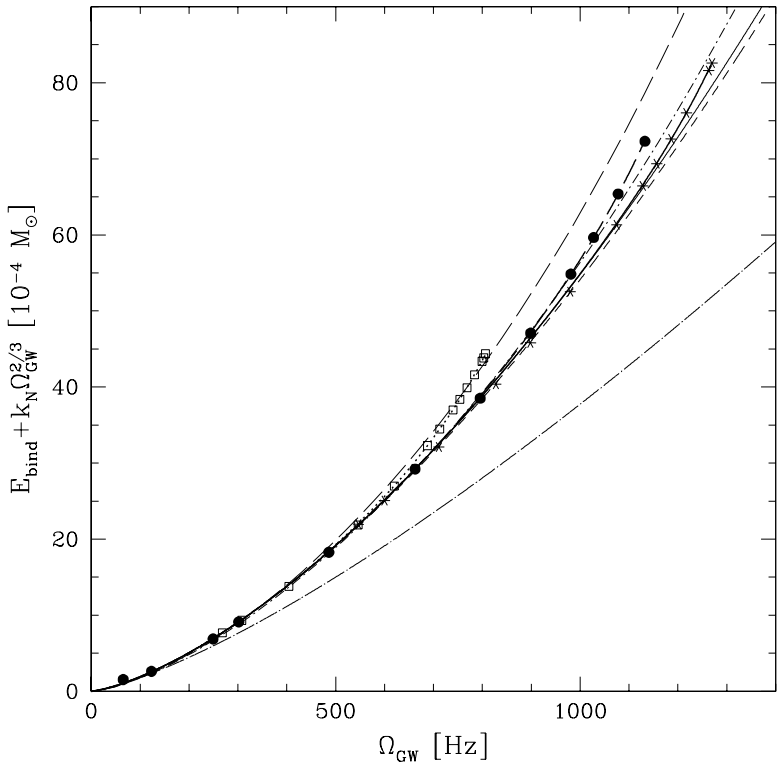

Figure 5.6: The orbital binding energy of the binary system decreased by the (point mass) Newtonian term $-k_N\Omega_{\rm GW}^{2/3}$ as a function of the GW frequency (twice the orbital frequency) along three irrotational quasi-equilibrium sequences. The thin solid line shows the 3PN approximation for point masses by Blanchet (2002). Slightly below there is the 2PN line (thin, dashed) and the 1PN one (thin, long dash-dotted). For comparison the post-Newtonian EOB approximation by Damour et al. (2000) – the 3PN (dashed-dotted thin line) and the 2PN (thin, long dashed) lines – are plotted.

of the power n was assumed. A more careful and refined treatment of such type of approximation is not needed to see its main feature – the departure from a point-mass-like system in favor of more complicated hydrodynamical behavior – that sort of conclusion can be drawn from these results and their comparison with approximations for binary point masses. We can expect that taking into account the next orders in a post-Newtonian approximation does not change the energy by an amount larger than the difference between the 2PN and 3PN models. As a consequence, the large deviation of the numerical results from the 3PN approximation is caused by the effect of the finite size of the star (e.g. hydrodynamical interaction, tidal forces). A very high power of n in Eq. (5.6) indicates that, even for small departures from a point mass

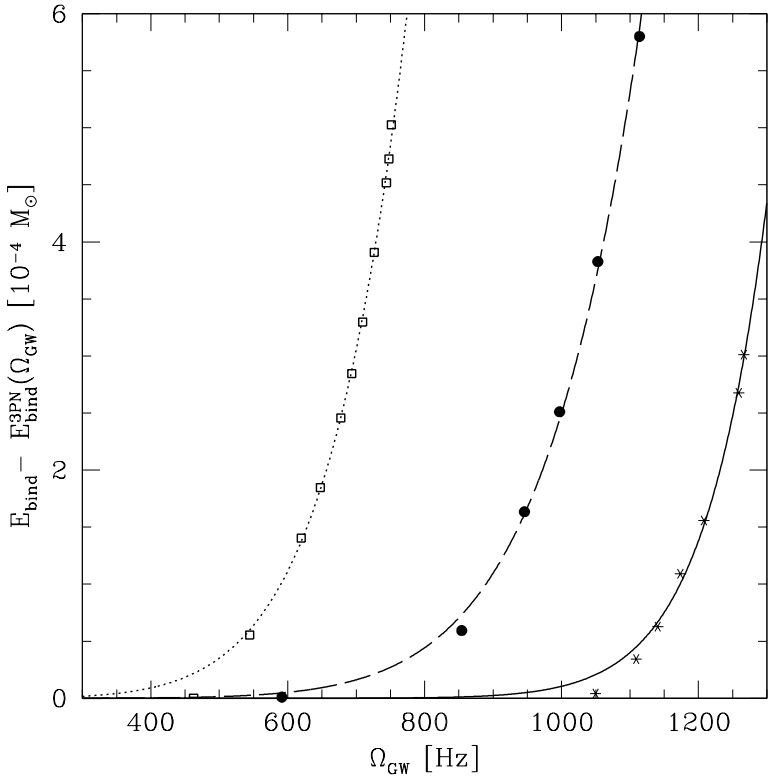

Figure 5.7: Difference $E_{\rm bind} - E^{\rm 3PN}_{\rm bind}$ between the binding energy of irrotational binary NSs built upon a realistic equation of state and the binding energy in the case of binary point-mass systems in the 3PN approximation of Blanchet (2002). The dots correspond to numerical results and the lines to polynomial fits to them (see details in the text).

approximation, the high-order tidal effects are very important and may be visible in detectors – they dominate the relation $E_{\rm bind}(\Omega_{\rm GW})$ for high $\Omega_{\rm GW}$. The lowest order tidal term is equal to $n = 4$, as shown by Lai et al. (1994); the values obtained here are well above this.

Finally, the energy spectrum of gravitational waves was computed. I used both Eq. (5.5) and Eq. (5.6) to calculate their first derivatives and therefore the GW energy spectrum. The relation between $\mathrm{d}E_{\rm bind}/\mathrm{d}\Omega$ and the GW frequency $\Omega_{\rm GW}$ is presented in Fig. 5.8. The straight lines correspond to the Newtonian $\sim \Omega^{2/3}_{\rm GW}$ formula – intersections with the fitted lines mark the *break frequencies* at which the energy spectrum has dropped by 20%, 25%, 35%, 40% and 50%, respectively. The break frequency values shown in Table 5.3, together with the final frequency $\Omega_{\rm end}$, are important from the practical point of view of future detections: they indicate the difference between an amplitude of the real signal

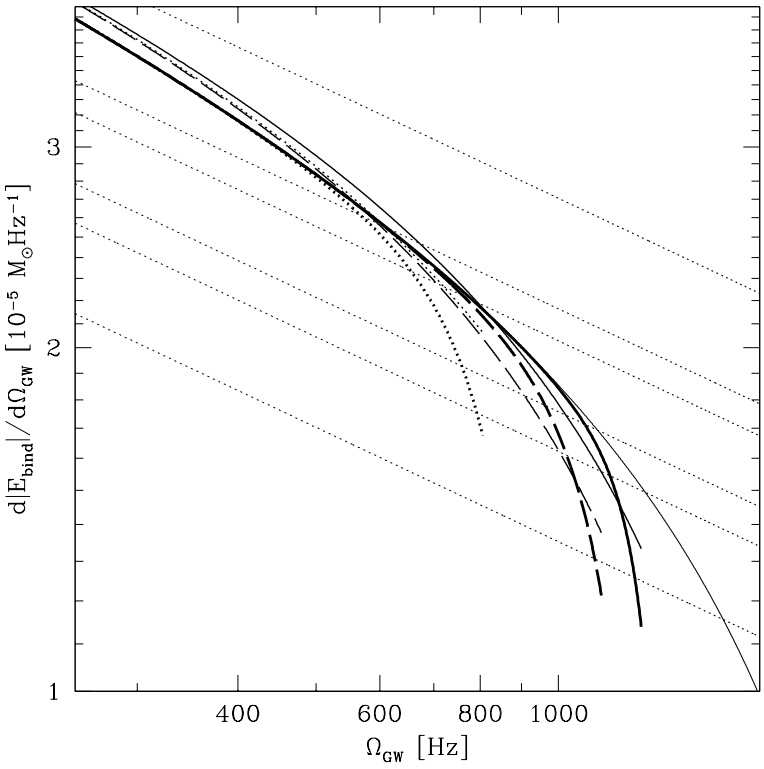

Figure 5.8: Energy spectrum of GW waves emitted by the binary NS system versus the frequency of gravitational waves $\Omega_{\rm GW}$ along three irrotational quasi-equilibrium sequences (thick dotted curve – GNH3, dashed – APR, solid – BPAL12) obtained with the use of Eq. (5.6). The thiner dotted, dashed and solid lines represent energy spectrum computed from Eq. (5.5). The thin solid line is the 3PN point-mass approximation. Straight thin dotted lines correspond to the Newtonian point-mass dependence on the energy multiplied by 1, 0.8, 0.75, 0.65, 0.6 and 0.5 (see Table 5.3 for the frequency values).

and the Newtonian template used in the detector for a given frequency. It will (hopefully) allow us to recover the real wave-form amplitude from the detector noise. As we can see, there are differences between results obtained by means of Eq. (5.5) and (5.6) – the latter approach seems to be more precise, as it is manifestly converging to 3PN formulae for smaller GW frequencies. The results can be also compared to the analogous case for a polytropic EOS by Faber et al. (2002). There is no drastic difference between the models for different EOSs at the break frequency level of 10% (the case considered by Faber et al. 2002) in both approximations – the results are then well described by post-Newtonian formulae.

Ω	GNH3	APR	BPAL12
Ω_{20}	567 (606)	615 (597)	615 (671)
Ω_{25}	657 (720)	762 (705)	785 (784)
Ω_{35}	759	963 (906)	1081 (1022)
Ω_{40}	792	1025 (1000)	1160 (1130)
Ω_{50}	-	1111	1244
$\Omega_{\rm npm}$	500	700	1050
$\Omega_{\rm end}$	806	1132	1270

Table 5.3: Characteristic gravitational wave frequencies (in Hz) for the GNH3, APR and BPAL12 EOSs: the values of Ω_{20}, Ω_{25}, Ω_{35}, Ω_{40} and Ω_{50} are the so-called break frequencies at which the energy spectrum drops 20%, 25%, 35% , 40% and 50% below the Newtonian point-mass template computed with the use of Eq. (5.6); if available, the values obtained from Eq. (5.5) are given in brackets for comparison (see Fig. 5.8). The value $\Omega_{\rm npm}$ denotes the approximate frequency at which non-point-mass hydrodynamical effects start to be important, whereas $\Omega_{\rm end}$ is the GW frequency at the last stable orbit.

5.4 Conclusions and remarks

I have presented a set of the evolutionary sequences of irrotational NS binaries. The stars' baryon masses corresponded to the values of individual gravitational masses of $1.35\,M_\odot$ at infinite separation, and were kept constant during calculations. The stars were based on three selected realistic nuclear EOSs (core EOSs) which were joined with a recent EOS of the NS crust, thus creating three different models of the NS interior. The analysis was restricted to models of NS cores without such exotic phases as quark matter or kaon condensates to make sure that the results are not spoiled by inclusion of *too hypothetical* phases or particles – only those constituents of dense matter were included which have been studied in the laboratories. The initial condition data sets can be found at `ftp://moscou.obspm.fr/BinaryNS/GR/Realistic/`.

The results can be summarized as follows: for most of the evolution of the binary system its binding energy $E_{\rm bind}$ is very accurately given by the 3PN post-Newtonian formula for a point-mass system. However, at the last stages of the inspiral phase, there is a sudden departure from the 3PN approximation due to high order tidal effects (as shown by e.g. Lai et al. 1994). All sequences presented here end at the mass-shedding limit, when a cusp forms at the surfaces of the stars. This point is a terminal point for the irrotational quasi-equilibrium binaries employed here – it defines the ISCO, since no turn-

ing (instability) point on the binding energy-frequency relation has been found (Kochanek, 1992; Bildsten and Cutler, 1992; Lai et al., 1993). The gravitational wave frequency $\Omega_{\rm end}$ at the ISCO equals 806 Hz, 1132 Hz and 1270 Hz, for the GNH3, APR and BPAL12 EOSs, respectively. This final frequency is strongly correlated with the compactness parameter, M/R. Combined measurements of $\Omega_{\rm end}$ and additional precise informations about NSs masses from the detection of the "chirp" mass, $\mathcal{M} = (M_1 M_2)^{3/5}(M_1 + M_2)^{-1/5}$, as well as the relativistic effects like the periastron advance and orbit decrease can yield the measurement of NSs radii (Faber et al., 2002), and thus put constraints on the EOS of dense matter.

It should be stressed that, in contrast to results presented here, calculations obtained by Oechslin et al. (2004) for an EOS with a compaction parameter M/R similar to the GNH3 EOS, reveal an instability point in the binding energy and a quasi-equilibrium ISCO, i.e. the situation where the surfaces of the stars touch. The difference originates from the EOS of matter. Oechslin et al. (2004) used nuclear and quark EOSs connected with a $\gamma = 2.86$ polytrope representing the star's crust. Such a crust EOS is, however, very unrealistic and far too stiff (the real γ can be as low as 0.5 near the neutron-drip point). For polytropic irrotational binaries a turning point ISCO exists only if $\gamma > 2.5$ (Uryū et al., 2000; Taniguchi and Gourgoulhon, 2003) and most certainly this is the reason for the appearance of the quasi-equilibrium ISCO in the results of Oechslin et al.

Recently, Marronetti et al. (2004) have located the ISCO with a full set of time-dependent Einstein equations by analyzing the time evolution of quasi-equilibrium initial data at various separations. Their calculations can be compared with the polytropic $\gamma = 2$ EOS results obtained by Taniguchi and Gourgoulhon (2002a), who used methods similar to those employed here. The difference in the location of the last sequence point in frequency is about 15%. Therefore, from the point of view of initial data for hydrodynamical merger one can, in principle, be sure that the values of gravitational wave frequencies calculated here are close to those corresponding to the true end of the inspiral.

Chapter 6

Summary

In the present work I have performed numerical calculations concerning various properties of NSs in order to obtain observational signatures of the unknown EOS of dense matter. The available parameter space was searched using simple parametric EOSs; moreover, I have also demonstrated that the presented effects also exist in realistic cases, with the use of example realistic EOSs. I have studied star-quakes induced by the phase transitions from a meta-stable core to a stable mixed-phase core, and the influence of such transitions on the global parameters of stellar configuration. The released energy, and the changes in radius and moment of inertia can be compared with the changes related to the observed astrophysical phenomena – they are of similar order (and sometimes even more pronounced), which leaves hope for successful detections in the future.

I also present the results of extensive studies concerning the influence of phase transitions on the observational properties of rotating NSs. The feature in question, called back-bending, denotes a temporal change of a rotation rate due to the softening of EOS by the newly created phase. I focus on the solitary spinning down pulsars, as well as the accreting spinning up NSs, and study the signatures in the timing properties. The characteristic frequency at which back-bending occurs depends very strongly on the EOS properties and the NS mass. In the case of accreting NSs the transfer of angular momentum is strictly connected to the transfer of mass – as the numerical calculations show, the features of back-bending are then strongly suppressed. In that case EOS must be very soft near the phase transition point to obtain the desired

back-bending results. At present, it is not easy to reveal the properties of the dense matter EOS using the presented theoretical results because of the lack of reliable direct observations. If, however, the back-bending phenomenon were to be confirmed by future observations, it would constitute a concrete and quantitative sign of phase transitions occurring in the NSs centers.

Models of close binary NS systems were constructed in order to compute the value of the orbital frequency just before the final merger phase. As it stems from the numerical simulations, the last stable orbit frequency (and what follows, the frequency of emitted gravitational waves) is strongly related to NS mass to radius ratio, i.e., to the compactness parameter M/R. The gravitational wave frequency spans from $\simeq$ 800 Hz to about $\simeq$ 1300 Hz in the case of 1.35 $M_{\odot}$ NSs for different realistic EOSs. The measurement of the gravitational wave frequency at the last stable orbit of a binary NS system combined with the measurements of the component NSs masses can therefore yield the stellar radius, and in this way can put constraints on the dense matter EOS. Also, the presented calculations will serve in the future as the initial data conditions for simulations of realistic EOS hydrodynamical mergers.

The field of theoretical and observational neutron-star astrophysics has been developing rapidly over the last few years. Many realistic EOSs used as examples in this work will be certainly ruled out i.e. the BPAL12 EOS from Chapter 5 gives a maximum allowable mass much too low to resist the observational data of massive NSs in binary systems (Stairs, 2004; Nice et al., 2004). It is an excellent and promising trend: we expect continual improvement of our knowledge in many domains related to NSs – the composition and physics of their interiors, as well as their influence on many astrophysical phenomena observed in the future with electromagnetic and gravitational waves and neutrinos.

I hope that the results and conclusions presented here will contribute to future progress in this interesting scientific field. In the future I plan to further investigate the physics of NSs with the use of numerical methods employing a time-dependent evolution, e.g., to dynamically simulate NSs phase transitions and to explore the physical processes at the last stages of binary NSs inspiral.

Appendix A

Simple fluid thermodynamics

Let us define the thermodynamical quantities in the local inertial frame co-moving with the fluid i.e. in the Lorentz local frame. In particular, the baryon number density $n_{\rm b}$ is very useful, because we can define a "per baryon" quantities, while the baryon number is conserved.

We will assume that the fluid element is in thermodynamic equilibrium at all times. The mass-energy density of such fluid is denoted by $\mathcal{E}$, and thus the first law of thermodynamics takes a form

$$\begin{aligned} \frac{\mathcal{E}}{n_{\rm b}} &= -\frac{P}{n_{\rm b}} + Ts + \sum_i \mu_i \left(\frac{n_i}{n_{\rm b}}\right) \ , \\ {\rm d}\left(\frac{\mathcal{E}}{n_{\rm b}}\right) &= -P{\rm d}\left(\frac{1}{n_{\rm b}}\right) + T{\rm d}s + \sum_i \mu_i {\rm d}\left(\frac{n_i}{n_{\rm b}}\right) \ , \end{aligned} \tag{A.1}$$

where $\mathcal{E}$ is the mass-energy density, P the fluid pressure, T its temperature and s the entropy per baryon. The summation extends on all species of particles, with corresponding number densities n_i and chemical potentials μ_i. From the thermodynamical identity one easily obtains the formulae for pressure

$$P = -\left(\frac{\partial(\mathcal{E}/n_{\rm b})}{\partial(1/n_{\rm b})}\right)_{s,n_i} = n_{\rm b}^2 \left(\frac{\partial(\mathcal{E}/n_{\rm b})}{\partial n_{\rm b}}\right)_{s,n_i} \ , \tag{A.2}$$

temperature

$$T = \left(\frac{\partial(\mathcal{E}/n_{\rm b})}{\partial s}\right)_{n_i,n_{\rm b}} \ , \tag{A.3}$$

and chemical potentials

$$\mu_i = \left(\frac{\partial(\mathcal{E}/n_{\rm b})}{\partial(n_i/n_{\rm b})}\right)_{s,n_{\rm b}} = \left(\frac{\partial \mathcal{E}}{\partial n_i}\right)_{s,n_{\rm b}} \ . \tag{A.4}$$

The chemical potential has an interpretation of the change in the energy density under a unit change in the number density of species i, with the entropy and volume constant. When the system is infinitesimally close to the equilibrium state and assuming that no work is done on the system, we have

$$\sum_i \mu_i \mathrm{d}\left(\frac{n_i}{n_\mathrm{b}}\right) = 0 \ . \tag{A.5}$$

because according to the second law of thermodynamics, the entropy is extremal in equilibrium, we have $\mathrm{d}s = 0$. This relation is very important during computation of the equilibrium states of mixtures of different particles.

The definition of the chemical potential stems also from the Eq. (A.1). For one-component system and for $T = 0$, the chemical potential is equal

$$\mu = \frac{\mathcal{E} + P}{n_\mathrm{b}} \ . \tag{A.6}$$

We define the dimensionless log-enthalpy (also called *pseudo-enthalpy*):

$$H(P) = \int_0^P \frac{\mathrm{d}P'}{\mathcal{E}(P') + P'} \ , \tag{A.7}$$

which can be rewritten in terms of the specific enthalpy

$$h(P) = \frac{\mathcal{E} + P}{m_0 c^2 n_\mathrm{b}} \tag{A.8}$$

as

$$H(P) = \ln h(P) = \ln\left(\frac{\mu}{\mu_0}\right) \ . \tag{A.9}$$

The quantity μ_0 denotes the chemical potential at vanishing pressure (condition met at stellar surface): $\mu_0 = (\mathcal{E}/n_\mathrm{b})(P = 0) = m_0 c^2$. For stationary, axisymmetric, rigidly rotating ideal fluids the first integral of motion is closely related to the log-enthalpy – see Eq. (2.20), as well as Eq. (2.38) in the case of binary systems.

The Gibbs free energy per baryon is defined as

$$g = \frac{\mathcal{E}}{n_\mathrm{b}} - Ts + \frac{P}{n_\mathrm{b}} = \sum_i \frac{n_i}{n_\mathrm{b}} \mu_i \ . \tag{A.10}$$

Comparison of the derivatives of both sides of Eq. (A.10), with the assumption that $T = 0$ and Eq. (A.1) gives

$$\mathrm{d}P = \sum_i n_i \mathrm{d}\mu_i \ . \tag{A.11}$$

This equation is called the *Gibbs-Duhem relation*; along with Eqs. (A.6–A.9) it takes more useful form of

$$\frac{\mathrm{d}P}{\mathrm{d}H} = \mathcal{E} + P \ . \tag{A.12}$$

A.1 Treatment of the tabulated EOS

The Gibbs-Duhem relation is used frequently for constructing *strictly* thermodynamically consistent EOSs. Realistic EOSs are usually provided in a form of tabular data. From a numerical point of view, simple interpolation between the data points introduces unwelcome errors, which often result in the thermodynamical inconsistency (i.e. violation of the strict laws of thermodynamics). In the `LORENE` framework the data from tabulated EOSs are interpolated using Swesty (1996) type of method. First of all log-enthalpy, Eqs. (A.7–A.9), and its derivative, Eq. (A.12) are computed from tabulated data. Then, the values of pressure P and $\mathrm{d}P/\mathrm{d}H$ are interpolated from the data points by means of Hermite polynomials. The last step is to obtain the missing values of mass-energy $\mathcal{E}$ and baryon density n_{b}:

$$\begin{aligned} \mathcal{E} &= \frac{\mathrm{d}P}{\mathrm{d}H} - P \ , \\ n_{\mathrm{b}} &= (\mathcal{E} + P)e^{-H} \ . \end{aligned} \tag{A.13}$$

Resulting equation of state strictly fulfills the laws of thermodynamics.

Appendix B

Relativistic polytropes

The relativistic polytrope is defined as a power-law dependence between the pressure P and the baryon number density $n_{\rm b}$:

$$P(n_{\rm b}) = K n_{\rm b}^{\gamma} \ , \tag{B.1}$$

The quantity γ is the adiabatic index; its value for realistic dense matter models is density dependent and varies between 4/3 and 3.5. The second coefficient, K, is called the pressure coefficient[1].

We will further assume that matter is strongly degenerate, so that the $T = 0$ approximation is valid. From the simplified case of one-component system, with the use of Eq. (A.1) and (A.2) we conclude that the mass-energy density is equal

$$\mathcal{E}/n_{\rm b} = \int^{n_{\rm b}} K n^{\gamma-2} {\rm d}n = \frac{K n_{\rm b}^{\gamma-1}}{\gamma - 1} + \mathcal{C} \ , \tag{B.2}$$

where the constant $\mathcal{C}$ equals, for $n_{\rm b} = 0$, the rest-energy of the baryon particle[2] ($\mathcal{C} = m_0 c^2$). The mass-energy density $\mathcal{E}$ of is thus given by

$$\mathcal{E}(n_{\rm b}) = \frac{K}{\gamma - 1} n_{\rm b}^{\gamma} + m_0 c^2 n_{\rm b} \ . \tag{B.3}$$

Similarly, the chemical potential μ, Eq. (A.5), which is equal to the change of the energy of matter at constant P and $T = 0$ due to an increase of the

[1]Unless otherwise mentioned, the coefficient $K_{\rm N}$ will be expressed in $\hat{\rho}c^2/\hat{n}^{\gamma}$ units, where $\hat{\rho} := 1.66 \times 10^{14}$ g/cm^3, and $\hat{n} := 0.1$ fm^{-3}.

[2]Here, the unit baryon mass is equal 1.66×10^{-24} g [Mass(^{56}Fe crystal)/56 in the ground state at $T = 0$, $P = 0$]

baryon number by one, reads

$$\mu(n_{\rm b}) = \frac{P+\mathcal{E}}{n_{\rm b}} = \frac{{\rm d}\mathcal{E}}{{\rm d}n_{\rm b}} = \frac{\gamma K}{\gamma-1} n_{\rm b}^{\gamma-1} + m_0 c^2 \ . \tag{B.4}$$

Consequently, the chemical potential at zero pressure equals the rest energy of a constituent particle. Notice that above definitions differ from the traditional generalization of the Newtonian polytrope, i.e. $P = k\rho^\gamma$. Moreover, the value γ of the relativistic polytrope is equal to the adiabatic index $\Gamma_{\rm ad} = (P+\mathcal{E})/P \cdot {\rm d}P/{\rm d}\mathcal{E}$ of the relativistic iso-entropic fluid. For Newtonian polytrope $P = k\rho^\gamma$ we recover $\Gamma_{\rm ad} = \gamma$ only in the non-relativistic limit.

I will now present a few formulae concerning parametric EOSs based on the relativistic polytropes. Those EOSs proved to be extremely useful to imitate to some extent the realistic phase transitions, due to their flexibility and ease of manipulating in the parameter space.

B.1 Constant-pressure phase transition

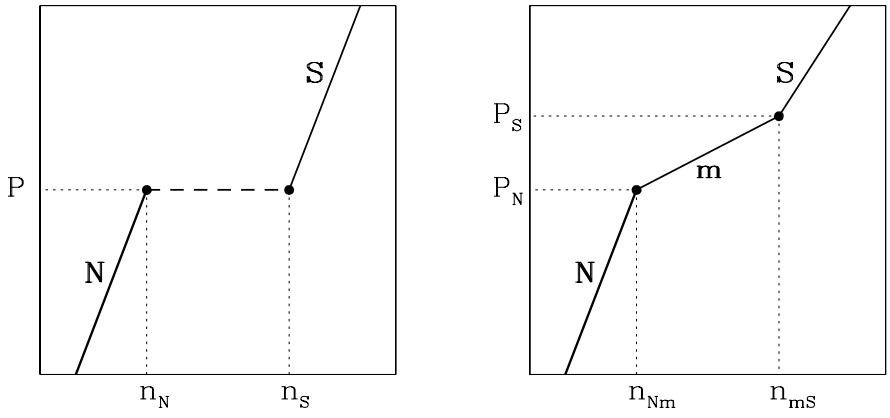

Figure B.1: Examples of an artificial "phase transitions" considered in the text; a constant-pressure phase transition (left), and a structured mixed-phase transition (right).

The phase transition should correspond to the thermodynamic equilibrium. In the most simple case the transition from a less dense pure phase N to a higher density pure phase S occurs at constant pressure (see Sect. 1.1 for details). Example of such transition is presented in Fig. B.1.

It will be assumed that the pure phases, N and S, are well approximated by polytropes with adiabatic indices $\gamma_{\rm N}$ and $\gamma_{\rm S}$, respectively. Let us also fix the baryon mass $m_{0\rm N}$ and the pressure coefficient $K_{\rm N}$ in the N phase, and demand that the phase transition occurs between the baryon densities $n_{\rm N}$ and $n_{\rm S}$, with the constant pressure P and continuous chemical potential μ. With these assumptions, the corresponding values of $K_{\rm S}$ and $m_{0\rm S}$ will be equal

$$K_{\rm S} = K_{\rm N}\frac{{n_{\rm N}}^{\gamma_{\rm N}}}{{n_{\rm S}}^{\gamma_{\rm S}}} , \tag{B.5}$$

$$m_{0\rm S} = m_{0\rm N} + P\left(\frac{\gamma_{\rm N}}{n_{\rm N}(\gamma_{\rm N}-1)} - \frac{\gamma_{\rm S}}{n_{\rm S}(\gamma_{\rm S}-1)}\right) . \tag{B.6}$$

B.2 Transition to a mixed phase

We will obtain the conditions for the transition from N phase to S phase through the region in which the two pure phases are mixed together, in this way constructing artificial "structured mixed-phase" EOS. It will be assumed that the N phase and the mixed phase m can be approximated by polytropes. Therefore, the $K_{\rm m}$, $\gamma_{\rm m}$, and $m_{\rm m}$ (the *mean* particle mass in the mixed phase) values must be related to those of the N phase in such a way that the pressure and the baryon chemical potential are continuous across the phase transition point $n_{\rm Nm}$,

$$K_{\rm m} = K_{\rm N}{n_{\rm Nm}}^{\gamma_{\rm N}-\gamma_{\rm m}} , \tag{B.7}$$

$$m_{\rm m} = m_{0\rm N} - \frac{P_{\rm N}}{n_{\rm Nm}c^2}\frac{\gamma_{\rm N}-\gamma_{\rm m}}{(\gamma_{\rm N}-1)(\gamma_{\rm m}-1)} . \tag{B.8}$$

Let us further assume that the dense phase S is composed of pure quarks. According to Zdunik (2000), the quark EOS can be approximated by a linear-type EOS of the following form:

$$P(\mathcal{E}) = \frac{1}{3}(\mathcal{E}-\mathcal{E}_0), \quad n_{\rm b}(P) = n_0(1+4P/\mathcal{E}_0)^{3/4} , \tag{B.9}$$

where $\mathcal{E}_0 = \rho_0 c^2$ is the mass-energy density and n_0 is the baryon density of the quark matter at zero pressure. The second equation is implied by the first law of thermodynamics (Eq. A.1).

The corresponding chemical potential is equal to

$$\mu(P) = \mu_0(1 + 4P/\mathcal{E}_0)^{1/4} \ , \tag{B.10}$$

where $\mu_0 = \mathcal{E}_0/n_0$.

From the equality of pressures and baryon densities in the phase transition point $n_{\rm mS}$, one has

$$\mathcal{E}_0 = \mathcal{E}(n_{\rm mS}) - 3P_{\rm S}, \quad n_0 = n_{\rm mS}/(1 + 4P_{\rm S}/\mathcal{E}_0)^{3/4} \ . \tag{B.11}$$

Appendix C

Spherically symmetric stars

The most general spherically symmetric metric can be written (in spherical coordinates) as

$$\mathrm{d}s^2 = -A(t,r)\mathrm{d}t^2 + B(t,r)\mathrm{d}r^2 + 2C(t,r)\mathrm{d}r\mathrm{d}t + D(t,r)\mathrm{d}\Omega^2 \ , \tag{C.1}$$

where r, θ and ϕ are the spatial coordinates and t is the coordinate time; $\mathrm{d}\Omega^2$ is the angular part of a line element – it depends on θ and ϕ only:

$$\mathrm{d}\Omega^2 = \mathrm{d}\theta^2 + \sin^2\theta\mathrm{d}\phi^2 \ . \tag{C.2}$$

One can in principle rearrange Eq. (C.1) by introducing the *new* time t and r coordinates to get an exponential form of the metric:

$$\mathrm{d}s^2 = -e^{2\Phi}\mathrm{d}t^2 + e^{2\lambda}\mathrm{d}r^2 + r^2\mathrm{d}\Omega^2 \ , \tag{C.3}$$

where Φ and λ are functions of t and r only.

Let us focus on the metric *inside* a spherical star. For simplicity, we will assume that the matter can be approximated by an one-parameter perfect fluid EOS:

$$P = P(\rho) \ , \tag{C.4}$$

where P is the pressure and ρ is the matter density, a quantity related to mass-energy density by $\mathcal{E} = \rho c^2$ (see Appendix A).

We also define a new metric function $m(r)$:

$$e^{2\lambda} \equiv \left(1 - \frac{2m}{r}\right)^{-1} \ . \tag{C.5}$$

In spherical symmetry the Einstein equations are called the Tolman-Oppenheimer-Volkoff (TOV) equations (Tolman, 1939; Oppenheimer and Volkoff, 1939):

$$\frac{\mathrm{d}P}{\mathrm{d}r} = -\frac{Gm(r)\rho(r)}{r^2}\left(1+\frac{P(r)}{\rho(r)c^2}\right)\left(1+\frac{4\pi r^3 P(r)}{m(r)c^2}\right)\left(1-\frac{2Gm(r)}{rc^2}\right)^{-1} \quad \text{(C.6)}$$

with the additional equation for the $m(r)$ function

$$\frac{\mathrm{d}m}{\mathrm{d}r} = 4\pi r^2 \rho \ , \quad \text{(C.7)}$$

and for the metric function $\Phi(r)$:

$$\frac{\mathrm{d}\Phi}{\mathrm{d}r} = -\frac{1}{\rho + P}\frac{\mathrm{dP}}{\mathrm{d}r} \ . \quad \text{(C.8)}$$

As we can see, the Eq. (C.6) is nothing else but the Newtonian hydrostatic balance equation modified by the relativistic terms in brackets. Additionally, the function $m(r)$ can be interpreted as stellar mass-energy inside the radius r.

The set of Eqs. (C.6–C.8) is likely to be solved analytically only in a limiting case of constant-density profile, $\rho(r) = const$. In a general case these equations should be solved numerically. Hydrostatic configurations form an one-parameter family which can be labelled by the central value of pressure, mass-energy density or baryon density, i.e. P_c, ρ_c or n_{bc}. This value is chosen to be the inner-boundary condition, along with the condition that $m(r=0)=0$. The outer-boundary of the star (the surface of the star) is defined as the surface at which the pressure vanishes, $P(r=R)=0$. When the pressure profile $P(r)$ is calculated, one can also obtain the mass-density profile $\rho(r)$ and, from Eq. (C.7), the mass of the configuration

$$M = m(R) = \int_0^R 4\pi\rho(r)r^2 dr \ . \quad \text{(C.9)}$$

In the thesis, the solutions for a given equation of state were obtained numerically with the use of 4th order Runge-Kutta integration method – to enhance the accuracy during the finite-difference integration from the center ($r=0$) to the surface ($P=0$) this method uses a sampling of slopes through a step interval and takes a weighted average to determine the right value at the end-point of the interval (see e.g. Press et al. 1992). Implementation of this method in a form of numerical codes is used by CAMK PAN neutron-star group.

Appendix D

Moment of inertia of a slowly rotating star

General line element for axisymmetric spacetime can be written as

$$\begin{aligned} \mathrm{d}s^2 &= -e^{2\nu(r,\theta)}\mathrm{d}t^2 + e^{2\beta(r,\theta)}\mathrm{d}r^2 + \\ &+ e^{2\gamma(r,\theta)}\left(r^2\mathrm{d}\theta^2 + r^2\sin^2\theta(\mathrm{d}\phi - L(r,\theta)\mathrm{d}t)^2\right) . \end{aligned} \tag{D.1}$$

The structure of such spacetime should not change under the reversal of time and the change of the sense of rotation ($\Omega \to -\Omega$). Therefore, the function $L(r,\theta)$ should depend on the odd powers of the angular frequency only. By defining the function $\omega(r,\theta) \sim \Omega$ we have

$$L(r,\theta) = \omega(r,\theta) + \mathcal{O}(\Omega^3) . \tag{D.2}$$

For a given θ function $\omega(r)$ is the angular frequency of local inertial frames; $\omega(r) = \mathrm{d}\phi/\mathrm{d}t$. At the infinity the spacetime is flat (no frame-dragging effect) which means that $\omega(r,\theta)$ should decay like $1/r^n$ ($n > 0$) and at the same time be proportional to the angular momentum J. From the dimensional analysis we got the relationship

$$\omega \propto \frac{GJ}{c^2 r^3} . \tag{D.3}$$

The angular velocity associated with the centrifugal force is proportional to the difference between the angular velocity of rotation and the angular frequency of inertial frames

$$\tilde{\omega}(r) = \Omega - \omega(r,\theta) . \tag{D.4}$$

We will now assume the slow rotation of a star as well as its spherical symmetry i.e. the TOV solution (see Appendix C), as it was proposed by Hartle (1967) who treated rotation as a perturbation of a spherically symmetric model. To remind his arguments I will quote his Eq. (46):

$$\frac{1}{r^4}\frac{\mathrm{d}}{\mathrm{d}r}\left(r^4 j\frac{\mathrm{d}\tilde{\omega}}{\mathrm{d}r}\right)+\tilde{\omega}\frac{4}{r}\frac{\mathrm{d}j}{\mathrm{d}r}=0\ , \tag{D.5}$$

where the function $j(r)$ is defined using the Schwarzschild metric, Eq. (C.3):

$$j(r)=\begin{cases} e^{-(\Phi+\lambda)}=e^{-\Phi}\sqrt{1-2Gm(r)/rc^2} & r<R \\ 1 & r\geqslant R \end{cases} \tag{D.6}$$

By differentiating the above equation we have

$$\frac{\mathrm{d}j}{\mathrm{d}r}=-4\frac{G}{c^4}\pi r e^{-\Phi}(P+\rho c^2)/\sqrt{1-2Gm(r)/rc^2}\ . \tag{D.7}$$

Integration of Eq. (D.5) from the center to the surface of the star gives

$$\left(r^4 j\frac{\mathrm{d}\tilde{\omega}}{\mathrm{d}r}\right)_R=-\int_0^R 4r^3\frac{\mathrm{d}j}{\mathrm{d}r}\tilde{\omega}\mathrm{d}r\ . \tag{D.8}$$

Recalling Eq. (D.3) and (D.4), one can write:

$$\frac{\mathrm{d}\tilde{\omega}}{\mathrm{d}r}\propto\frac{3GJ}{c^2r^4} \tag{D.9}$$

and

$$J\propto\frac{c^2}{3G}\left(r^4 j\frac{\mathrm{d}\tilde{\omega}}{\mathrm{d}r}\right)_R\propto-\frac{c^2}{3G}\int_0^R 4r^3\frac{\mathrm{d}j}{\mathrm{d}r}\tilde{\omega}\mathrm{d}r\ . \tag{D.10}$$

From the slow-rotation approximation one has the $J=I\Omega$ relationship, where the proportionality constant I denotes the moment of inertia. The Newtonian moment of inertia I_{newt} for a sphere with a radius R and with the axis of rotation going through the center equals

$$I_{\mathrm{newt}}=\frac{8\pi}{3}\int_0^R \rho r^4\mathrm{d}r\ . \tag{D.11}$$

By comparing Eq. (D.11) with Eq. (D.10) divided by Ω and by putting $2Gm/rc^2\ll 1$ and $P\ll\rho c^2$ one reproduces the Newtonian prefactor. The value of I finally reads

$$I=\frac{J}{\Omega}\int_0^R\frac{|\tilde{\omega}(r)|}{\Omega}\frac{P+\rho c^2}{\sqrt{1-2Gm(r)/rc^2}}e^{-\Phi}r^4\mathrm{d}r\ . \tag{D.12}$$

The values of I used in Chapter 3 were obtained numerically during the solution of the TOV equations (Appendix C).

Appendix E

Basics of spectral methods

Spectral methods in fluid dynamics and astrophysics, especially within the framework of General Relativity, are very efficient for numerically simulating the gravitational collapses, rotating stars and star systems, and many other three-dimensional phenomena. These methods provide, among other advantages, an unique tool for solving partial differential equations (PDE) – results presented in the thesis frequently benefit from this fact.

As opposed to other numerical methods, like finite differences methods or Smooth Particle Hydrodynamics (SPH) which represent functions (scalars or fields) with a set of numbers on *grid points*, spectral methods display the function as another function belonging to a suitable vector space. Let us consider $\mathcal{H}$, the linear (vector) space of functions, in which a scalar product is defined (Hilbert space). Within this space there exist an orthonormal set of functions $\varphi_0, ..., \varphi_N$. Let our function is called u. By the orthogonal projection $\mathcal{P}$ of u on $\mathcal{H}$ (expansion of u in the $\mathcal{H}$ space on the φ-basis) one has

$$\mathcal{P}u = \sum_{n=0}^{N} \hat{u}_n \varphi_n \ , \tag{E.1}$$

where the coefficients $\hat{u}_0, ..., \hat{u}_N$ are given by the scalar product in $\mathcal{H}$,

$$\hat{u}_n = \langle u, \ \varphi_n \rangle \ . \tag{E.2}$$

In general, the above equation is usually a complicated integral. To avoid time-consuming calculations, instead of representing u as $\mathcal{P}u$ one used another function

$$\mathcal{I}u = \sum_{n=0}^{N} \bar{u}_n \varphi_n \ . \tag{E.3}$$

where the coefficients $\hat{u}_n$ were replaced by their approximations $\bar{u}_n$ (if treated without care, this procedure can cause so-called *aliasing error* coming from the difference between $\hat{u}_n$ and $\bar{u}_n$). Let us assume that u is a function from the space U (in most cases of interest $U \equiv \mathbb{R}$). Generally, we are interested in solving the PDE with boundary condition:

$$\begin{aligned} \mathcal{L}u(x) &= s(x), \quad x \in U \ , \\ \mathcal{B}u(y) &= 0, \qquad y \in \partial U \ , \end{aligned} \tag{E.4}$$

where $\mathcal{L}$ and $\mathcal{B}$ are differential operators and s is called the source term. In practice, the solution $\tilde{u}$ of this problem is a function which makes the residual $\mathcal{R}$

$$\mathcal{R} = \mathcal{L}\tilde{u} - s$$

sufficiently small. When $\mathcal{L}$ is a PDE linear operator, the solution amounts for solving a system of linear equations:

$$\mathcal{L}(\mathcal{I}u) = \sum_{n=0}^{N} \bar{u}_n(\mathcal{L}\varphi_n) = \sum_{k=0}^{N} \left(\sum_{n=0}^{N} a_{kn}\bar{u}_n \right) \varphi_k \ , \tag{E.5}$$

with

$$\mathcal{L}\varphi_n = \sum_{k=0}^{N} a_{kn}\varphi_k \ . \tag{E.6}$$

Non-linear PDEs cannot be solved efficiently in that way – the so-called *pseudo-spectral (collocation)* method is used in this case. Function u is described by its values on a finite set of *collocation* points $u(x_0), ..., u(x_N)$, chosen in such a way that will keep the information about the spectral coefficients $\bar{u}_0, ..., \bar{u}_N$ so the evaluation of the operator at those points makes possible the computation of the spectral expansions of the results.

For a smooth (class $\mathcal{C}^\infty$) function the numerical error related to the truncation of the expansion series decreases as $\exp(-N)$ (*evanescent error*), where N is the number of coefficient involved in the series – for pseudo-spectral methods, it is the number of collocation points; with sufficient number of points one can reach the machine accuracy. This rate should be compared with the finite differences method, where typically one has a decrease $\sim 1/N^3$ (and sometimes even slower). In the case of non-smooth functions spectral methods lose some of their accuracy, because of the so-called Gibbs phenomenon – if the

function is of class $\mathcal{C}^p$ only, the error decreases approximately as $\sim 1/N^p$. The discrepancy between exact and computed solutions can be as much as 10% when one uses discontinous functions, the like density jump in star's density profile during phase transition.

The way of resolving such problem is to divide the physical computational range into several domains, with boundaries located in the trouble spots e.g., the density jumps or the surface of the star, and to obtain the solution in each of those domains. In the case of stars the physical coordinates $(r,\ \theta,\ \phi)$ are mapped onto the cross product of intervals $[r_0,\ 1] \times [0,\ \pi] \times [0,\ 2\pi[$, where r_0 depends on the boundary conditions ($r_0 = 0$ if the domain contains the origin, and $r_0 = -1$ otherwise). The last domain is compactified, with the radial coordinate $r \to 1/r$ – in this way the computational domain extend to spatial infinity (which is important in, e.g., the process gravitational waves extraction). In the case of ϕ coordinate it is natural to use Fourier series. The radial coordinate is expanded with the use of Chebyshev polynomials, and in the θ direction the expansion in series of $\sin(j\theta)$ or $\cos(j\theta)$ is performed (depending on the degree of the spherical harmonics; this choice allows to use Fast Fourier Transform to compute expansion coefficients).

The system of spherical coordinates is used in the `LORENE` framework, because astrophysical objects have most often spherical-like shapes, thus an usually low number of points in ϕ direction is a numerical advantage of such coordinates: in the more often numerically used Cartesian coordinates the accuracy of the results depends in equal way on all three directions. Typically, the calculations of rapidly rotating axisymmetric star with one domain star and a polytropic EOS with the accuracy in virial errors of $\sim 10^{-7}$ and the precision of central parameters $\sim 10^{-9}$ demand 33 collocation points in r direction and 17 points in θ direction. Multi-domain calculation (2-3 domains inside a star) demands an increase of collocation points to 65 in r direction and 33 in θ direction for the same accuracy.

Details of mapping and spectral expansions in the general case of 3D compact object is described by Bonazzola et al. (1998). An overview of spectral methods in astrophysics is presented by Bonazzola et al. (1999b). Great general references about spectral methods are books written by Gottlieb and Orszag (1977); Canuto et al. (1988) and Boyd (2001).

Index

Glossary

Subscripts N and S correspond to a normal and super-dense phases, whereas subscript m and index (m) corresponds to the mixed phase. Subscript c designates the central values of parameters, like in $P_{\rm c}$. Also, in Chapter 3 quantities with a bar over a symbol e.q. $\bar{r}_{\rm m}$ are normalized to the reference configuration ($\bar{r}_{\rm m} \equiv r_{\rm m}/R_0$). The time derivative is sometimes represented by a dot over a symbol e.g. $\dot{a}$. In Appendices C and D the symbol λ denotes the metric function. In Appendix E the symbols $\mathcal{L}$ and $\mathcal{R}$ denote the differential operators.

A**,** B	Conformal factors
$A_{\rm B}$	Number of baryon inside a star
β_Q	Linear response coefficient
$\mathbf{B}$, B^i	Shift vector (binary neutron stars case)
c	Velocity of light ($2.99792458 \times 10^{10}$ cm/s^2)
C***,** C**,** C$_0$	Mixed-phase, meta-stable and the reference configurations
D_i	Covariant derivative associated with the spatial metric $\mathbf{h}$
$E_{\rm bind}$	Binding energy [$M_\odot$]
$\mathcal{E}$	Energy density (ρc^2)
$\boldsymbol{\eta}$**,** η_{ij}	Flat spatial 3-metric
fm	Fermi (femtometer: 10^{-13} cm)
G	Gravitational constant (6.672×10^{-8} cm^3/g/s^2)
Γ	Lorentz factor
γ	Adiabatic index ($\mathrm{d}\ln P/\mathrm{d}\ln n_{\rm b}$)
g	Gibbs free energy
$\mathbf{g}$, $g_{\mu\nu}$	Spacetime metric
H	Log-enthalpy (pseudo-enthalpy: $H = \ln h$)
h	Enthalpy
$\mathbf{h}$, h_{ij}	Metric induced on Σ_t
I	Moment of inertia
J	Angular momentum [$GM_\odot^2/c$]
K	Pressure coefficient
K_{ij}	Extrinsic curvature tensor

λ	Density jump
$\underline{\Delta}$	Flat metric $\boldsymbol{\eta}$ Laplacian
$l_{\rm IS}$	Specific angular momentum of a particle at the ISCO
$\mathcal{L}_n$	Lie derivative along vector $\mathbf{n}$
M	Gravitational mass [$M_\odot$]
$M_\odot$	Solar mass (1.989×10^{33} g)
$M_{\rm ADM}$	Arnowitt-Deser-Misner (ADM) mass [$M_\odot$]
$M_{\rm B}$	Baryon mass [$M_\odot$]
$M_{\rm B}^{\rm on}$, $M_{\rm B}^{\rm stat}$, $M_{\rm B}^{\rm sup}$	Baryon masses for the onset of back-bending, the maximal allowable mass of static star, and the baryon mass above which the spin-down is impossible [$M_\odot$]
μ	Chemical potential
$\mathcal{M}$	"Chirp mass" of a binary system
N	Time lapse
$\overline{\nabla}$	Covariant derivative associated with the flat 3-metric $\boldsymbol{\eta}$
$n(\Omega)$	Braking index ($n(\Omega) = \Omega\ddot{\Omega}/\dot{\Omega}^2$)
$n_{\rm nuc}$	Baryon nuclear saturation density ($n_{\rm nuc} = 0.16$ fm^{-3})
$\mathbf{N}$, N^i	Shift vector (axisymmetric star case)
$n_{\rm b}$	Baryon number density [fm^{-3}]
Ω	Spin frequency [Hz]
$\Omega_{\rm on}$	Back-bending onset frequency [Hz]
$\Omega_{\rm GW}$	Frequency of gravitational waves [Hz]
Ψ	Scalar potential of the irrotational flow
P	Pressure [dyne/cm^2]
R	Radius of a non-rotating spherically symmetric star [km]
$R_{\rm eq}$	Equatorial radius of rotating axisymmetric star [km]
ρ	Mass density [g/cm^3]
$\rho_{\rm cc}$	Crust-core interface density ($\simeq 0.6 - 1.4 \times 10^{14}$ g/cm^3)
$\rho_{\rm nd}$	Neutron-drip density ($\simeq 4 \times 10^{11}$ g/cm^3)
$\rho_{\rm nuc}$	Nuclear saturation density (2.8×10^{14} g/cm^3)
$r_{\rm ms}$	Marginally stable orbit radius [km]
$\mathcal{R}_{\mu\nu}$	Ricci curvature tensor
$r_{\rm N}$	Meta-stable core radius [km]
$r_{\rm m}$	Mixed-phase core radius [km]
Σ_t	Hypersurface of $t = const.$
T	Temperature [K]
$\otimes$	Tensor product ($\boldsymbol{A} = \boldsymbol{a} \otimes \boldsymbol{b}$,$A^{ij} = a^i b^j$)
$\mathcal{T}_{\mu\nu}$	Stress-energy tensor
u_μ	4-velocity of the fluid
x_l	Fraction of the angular momentum
$x_{\rm N}$	Relativistic factor $P_{\rm N}/\rho_{\rm N}c^2$

Bibliography

B. Abbott et al. Detector Description and Performance for the First Coincidence Observations between LIGO and GEO. **Nucl. Instrum. Meth. A**, 517:154–179, 2004.

F. Acernese et al. Status of VIRGO. **Class. Quantum Grav.**, 21:S385–S394, 2004.

A. Akmal, V. R. Pandharipande, and D. G. Ravenhall. Equation of state of nucleon matter and neutron star structure. **Phys. Rev. C**, 58:1804–1828, September 1998.

C. Alcock, E. Farhi, and A. Olinto. Strange stars. **ApJ**, 310:261–272, November 1986.

M. Ando et al. Stable operation of a 300-m laser interferometer with sufficient sensitivity to detect gravitational-wave events within our galaxy. **Phys. Rev. Lett.**, 86:3950, 2001.

W. Baade and F. Zwicky. Supernovae and cosmic rays. **Phys. Rev.**, 45:138, 1934a.

W. Baade and F. Zwicky. On supernovae. **Proc. National Acad. Sci.**, 20:254–259, 1934b.

W. Baade and F. Zwicky. Remarks on super-novae and cosmic rays. **Phys. Rev.**, 46:76–77, 1934c.

S. Balberg and A. Gal. An effective equation of state for dense matter with strangeness. **Nucl. Phys.**, A625:435–472, 1997.

S. Balberg, I. Lichtenstadt, and G. B. Cook. Roles of Hyperons in Neutron Stars. **ApJ Supp. Ser.**, 121:515–531, April 1999.

S. Banik, M. Hanauske, D. Bandyopadhyay, and W. Greiner. Rotating compact stars with exotic matter. **Phys. Rev. D**, 70(12):123004, December 2004.

J. M. Bardeen and R. V. Wagoner. Relativistic Disks. I. Uniform Rotation. **ApJ**, 167:359, August 1971.

T. W. Baumgarte, G. B. Cook, M. A. Scheel, S. L. Shapiro, and S. A. Teukolsky. General relativistic models of binary neutron stars in quasiequilibrium. **Phys. Rev. D**, 57:7299–7311, June 1998.

G. Baym and S. A. Chin. Can neutron star be a giant mit bag? **Phys. Lett.**, B62:241–244, 1976.

G. Baym, C. Pethick, and P. Sutherland. The ground state of matter at high densities: Equation of state and stellar models. **ApJ**, 170:299–317, 1971.

M. Bejger, D. Gondek-Rosińska, E. Gourgoulhon, P. Haensel, K. Taniguchi, and J. L. Zdunik. Impact of the nuclear equation of state on the last orbits of binary neutron stars. **A&A**, 431:297–306, February 2005a.

M. Bejger, P. Haensel, and J. L. Zdunik. Mixed-phase induced core-quakes and the changes in neutron star parameters. 2005b. astro-ph/0502348 (accepted by **Mon. Not. R. Astron. Soc.**).

L. Bildsten and C. Cutler. Tidal interactions of inspiraling compact binaries. **ApJ**, 400: 175–180, November 1992.

L. Blanchet. Innermost circular orbit of binary black holes at the third post-Newtonian approximation. **Phys. Rev. D**, 65(12):124009, June 2002.

I. Bombaci. In A. Fabrocini et al. ed. I. Bombaci, A. Bonaccorso, editor, *in: Perspectives on Theoretical Nuclear Physics*, 1995.

S. Bonazzola. The virial theorem in general relativity. **ApJ**, 182:335–340, 1973.

S. Bonazzola and E. Gourgoulhon. A virial identity applied to relativistic stellar models. **Class. Quantum Grav.**, 11:1775–1784, 1994.

S. Bonazzola and G. Maschio. Models of Rotating Neutron Stars in General Relativity. In **IAU Symp. 46: The Crab Nebula**, page 346, 1971.

S. Bonazzola and J. Schneider. An Exact Study of Rigidly and Rapidly Rotating Stars in General Relativity with Application to the Crab Pulsar. **ApJ**, 191:273–290, July 1974.

S. Bonazzola, E. Gorgoulhon, M. Salgado, and J. A. Marck. Axisymmetric rotating relativistic bodies: A new numerical approach for 'exact' solutions. **A&A**, 278:421–443, November 1993.

S. Bonazzola, E. Gourgoulhon, and J. Marck. Relativistic formalism to compute quasiequilibrium configurations of nonsynchronized neutron star binaries. **Phys. Rev. D**, 56: 7740–7749, December 1997.

S. Bonazzola, E. Gourgoulhon, and J. A. Marck. Numerical approach for high precision 3D relativistic star models. **Phys. Rev. D**, 58(10):104020, November 1998.

S. Bonazzola, E. Gourgoulhon, and J. Marck. Numerical Models of Irrotational Binary Neutron Stars in General Relativity. **Phys. Rev. Lett.**, 82:892–895, February 1999a.

S. Bonazzola, E. Gourgoulhon, and J. A. Marck. Spectral methods in general relativistic astrophysics. **J. Comput. Appl. Math.**, 109:433, 1999b.

J. P. Boyd. *Chebyshev and Fourier spectral methods*, volume 2nd edition. Mineola, Dover, 2001.

E. M. Butterworth and J. R. Ipser. On the structure and stability of rapidly rotating fluid bodies in general relativity. I - The numerical method for computing structure and its application to uniformly rotating homogeneous bodies. **ApJ**, 204:200–223, February 1976.

A. G. W. Cameron. A Revised Table of Abundances of the Elements. **ApJ**, 129:676, May 1959.

C. Canuto, M. Y. Hussaini, A. Quarteroni, and T. A. Zang. *Spectral Methods for Fluid Dynamics*. Springer-Verlag, New York, 1988.

B. Carter. in Active Galactic Nuclei. In *Cambridge University Press, Cambridge, England*, page 273, 1979.

J. Chadwick. Possible existence of a neutron. **Nature**, 129:312, 1932.

D. Chakrabarty. Millisecond pulsars in x-ray binaries. *astro-ph/0408004*, 2004.

D. Chakrabarty et al. Nuclear-powered millisecond pulsars and the maximum spin frequency of neutron stars. **Nature**, 424:42, 2003.

K. S. Cheng, Y. F. Yuan, and J. L. Zhang. Phase Transitions in Rotating Neutron Stars: Effects of Stellar Crusts. **ApJ**, 564:909–913, January 2002.

A. Chodos, R. L. Jaffe, K. Johnson, Charles B. Thorn, and V. F. Weisskopf. A new extended model of hadrons. **Phys. Rev.**, D9:3471–3495, 1974.

M. B. Christiansen and N. K. Glendenning. Finite size effects and the mixed quark-hadron phase in neutron stars. **Phys. Rev.**, C56:2858–2864, 1997.

M. B. Christiansen, N. K. Glendenning, and J. Schaffner-Bielich. Surface tension between a kaon condensate and the normal nuclear matter phase. **Phys. Rev. C**, 62(2):025804, August 2000.

E. Chubarian, H. Grigorian, G. Poghosyan, and D. Blaschke. Deconfinement transition in rotating compact stars. **A&A**, 357:968–976, May 2000.

G. B. Cook, S. L. Shapiro, and S. A. Teukolsky. Spin-up of a rapidly rotating star by angular momentum loss - Effects of general relativity. **ApJ**, 398:203–223, October 1992.

G. B. Cook, S. L. Shapiro, and S. A. Teukolsky. Rapidly rotating polytropes in general relativity. **ApJ**, 422:227–242, February 1994a.

G. B. Cook, S. L. Shapiro, and S. A. Teukolsky. Rapidly rotating neutron stars in general relativity: Realistic equations of state. **ApJ**, 424:823–845, April 1994b.

G. B. Cook, S. L. Shapiro, and S. A. Teukolsky. Testing a simplified version of Einstein's equations for numerical relativity. **Phys. Rev. D**, 53:5533–5540, May 1996.

T. Damour, P. Jaranowski, and G. Schäfer. Determination of the last stable orbit for circular general relativistic binaries at the third post-Newtonian approximation. **Phys. Rev. D**, 62(8):084011, October 2000.

F. Douchin and P. Haensel. Inner edge of neutron-star crust with sly effective nucleon-nucleon interactions. **Phys. Lett.**, B485:107–114, 2000.

F. Douchin and P. Haensel. A unified equation of state of dense matter and neutron star structure. **A&A**, 380:151–167, December 2001.

J. A. Faber, P. Grandclement, F. A. Rasio, and K. Taniguchi. Measuring neutron star radii with gravitational wave detectors. **Phys. Rev. Lett.**, 89:231102, 2002.

E. Farhi and R. L. Jaffe. Strange matter. **Phys. Rev.**, D30:2379, 1984.

J. L. Friedman, L. Parker, and J. R. Ipser. Rapidly rotating neutron star models. **ApJ**, 304:115–139, May 1986.

J. L. Friedman, J. R. Ipser, and R. D. Sorkin. Turning-point method for axisymmetric stability of rotating relativistic stars. **ApJ**, 325:722–724, February 1988.

J. L. Friedman, K. Uryū, and M. Shibata. Thermodynamics of binary black holes and neutron stars. **Phys. Rev. D**, 65(6):064035, March 2002.

R. Giacconi, H. Gursky, F. R. Paolini, and B. B. Rossi. Evidence for x-rays from sources outside the solar system. **Phys. Rev. Lett.**, 9:439–443, 1962.

N. K. Glendenning. *Compact stars: Nuclear physics, particle physics, and general relativity.* New York, USA: Springer, 1997.

N. K. Glendenning. Neutron stars are giant hypernuclei? **ApJ**, 293:470–493, June 1985.

N. K. Glendenning. Fast pulsars, variational bound, other facets of compact stars. **Nucl. Phys. Proc. Suppl.**, 24B:110–118, 1991.

N. K. Glendenning. First-order phase transitions with more than one conserved charge: Consequences for neutron stars. **Phys. Rev.**, D46:1274–1287, August 1992.

N. K. Glendenning and S. Pei. Crystalline structure in the confined-deconfined mixed phase. **Heavy Ion Phys.**, 1:323–333, 1995.

N. K. Glendenning and J. Schaffner-Bielich. Kaon Condensation and Dynamical Nucleons in Neutron Stars. **Phys. Rev. Lett.**, 81:4564–4567, November 1998.

N. K. Glendenning and J. Schaffner-Bielich. First order kaon condensate. **Phys. Rev. C**, 60(2):025803, August 1999.

N. K. Glendenning and F. Weber. Signal of Quark Deconfinement in Millisecond Pulsars and Reconfinement in Accreting X-ray Neutron Stars. *Lecture Notes in Physics, Berlin Springer Verlag*, 578:305, 2001a.

N. K. Glendenning and F. Weber. Phase Transition and Spin Clustering of Neutron Stars in X-Ray Binaries. **ApJ**, 559:L119–L122, October 2001b.

N. K. Glendenning, S. Pei, and F. Weber. Signal of Quark Deconfinement in the Timing Structure of Pulsar Spin-Down. **Phys. Rev. Lett.**, 79:1603–1606, September 1997.

T. Gold. Rotating Neutron Stars as the Origin of the Pulsating Radio Sources. **Nature**, 218:731, 1968.

D. Gottlieb and S. A. Orszag. *Numerical Analysis of Spectral Methods*. SIAM, Philadelphia, PA, 1977.

E. Gourgoulhon. *A new formulation for evolving neutron star spacetimes*, 2004. 1st Astro-PF workshop.

E. Gourgoulhon and S. Bonazzola. A formulation of the virial theorem in general relativity. **Class. Quantum Grav.**, 11:443–452, 1994.

E. Gourgoulhon, P. Grandclément, K. Taniguchi, J. Marck, and S. Bonazzola. Quasiequilibrium sequences of synchronized and irrotational binary neutron stars in general relativity: Method and tests. **Phys. Rev. D**, 63(6):064029, March 2001.

P. Haensel. Non-equilibrium neutrino emissivities and opacities of neutron star matter. **A&A**, 262:131–137, August 1992.

P. Haensel. in: Physics of neutron star interiors. In A. Sedrakian D. Blaschke, N.K. Glendenning, editor, *Feature Grouping*. Springer, Berlin, 2001.

P. Haensel and B. Pichon. Experimental nuclear masses and the ground state of cold dense matter. **A&A**, 283:313–318, March 1994.

P. Haensel, J. L. Zdunik, and R. Schaeffer. Strange quark stars. **A&A**, 160:121–128, May 1986a.

P. Haensel, J. L. Zdunik, and R. Schaeffer. Changes in stellar parameters implied by a neutron star corequake. **A&A**, 160:251–258, May 1986b.

P. Haensel, J. L. Zdunik, and F. Douchin. Equation of state of dense matter and the minimum mass of cold neutron stars. **A&A**, 385:301–307, April 2002.

T. Harko, K. S. Cheng, and P. S. Tang. Nucleation of quark matter in neutron stars cores. **ApJ**, 608:945–956, 2004.

J. B. Hartle. Slowly rotating relativistic stars. 1. equations of structure. **ApJ**, 150:1005, 1967.

J. B. Hartle and K. S. Thorne. Slowly Rotating Relativistic Stars. II. Models for Neutron Stars and Supermassive Stars. **ApJ**, 153:807, September 1968.

J. B. Hartle and K. S. Thorne. Slowly Rotating Relativistic Stars. III. Static Criterion for Stability. **ApJ**, 158:719, November 1969.

H. Heiselberg and M. Hjorth-Jensen. Phase Transitions in Rotating Neutron Stars. **Phys. Rev. Lett.**, 80:5485–5488, June 1998.

H. Heiselberg and M. Hjorth-Jensen. Phases of dense matter in neutron stars. **Phys. Rep.**, 328:237–327, May 2000.

H. Heiselberg, C. J. Pethick, and E. F. Staubo. Quark matter droplets in neutron stars. **Phys. Rev. Lett.**, 70:1355–1359, March 1993.

J. Hester, K. Mori, D. Burrows, P. Scowen, M. Halverson, C. Michel, J. Gallagher, and J. Graham. HST and Chandra Monitoring of the Crab Synchrotron Nebula. **Bulletin of the AAS**, 33:1491, December 2001. (Cover photo).

A. Hewish, S. J. Bell, J. D. Pilkington, P. F. Scott, and R. A. Collins. Observation of a Rapidly Pulsating Radio Source. **Nature**, 217:709, 1968.

M. Hewitson et al. A report on the status of the geo 600 gravitational wave detector. **Class. Quantum Grav.**, 20:S581–S591, 2003.

K. Iida and K. Sato. Quantum nucleation of two-flavor quark matter in neutron stars. **Prog. Theor. Phys.**, 98:277–282, 1997.

K. Iida and K. Sato. Effects of hyperons on the dynamical deconfinement transition in cold neutron star matter. **Phys. Rev. C**, 58:2538–2559, October 1998.

N. Itoh. Hydrostatic equilibrium of hypotetical quark stars. **Prog. Theor. Phys.**, 44: 291–292, 1970.

D. Ivanenko and D. F. Kurdgelaidze. Hypothesis on quark stars. **Astrofizika**, 1:479–482, 1965.

D. B. Kaplan and A. E. Nelson. Strange goings in dense nucleonic matter. **Phys. Lett. B**, 175:57–63, 1986.

R. P. Kerr. Gravitational field of a spinning mass as an example of algebraically special metrics. **Phys. Rev. Lett.**, 11:237–238, 1963.

C. S. Kochanek. Coalescing binary neutron stars. **ApJ**, 398:234–247, October 1992.

H. Komatsu, Y. Eriguchi, and I. Hachisu. Rapidly rotating general relativistic stars. I - Numerical method and its application to uniformly rotating polytropes. **Mon. Not. R. Astron. Soc.**, 237:355–379, March 1989a.

H. Komatsu, Y. Eriguchi, and I. Hachisu. Rapidly rotating general relativistic stars. II - Differentially rotating polytropes. **Mon. Not. R. Astron. Soc.**, 239:153–171, July 1989b.

D. Lai, F. A. Rasio, and S. L. Shapiro. Ellipsoidal figures of equilibrium - Compressible models. **ApJ Supp. Ser.**, 88:205–252, September 1993.

D. Lai, F. A. Rasio, and S. L. Shapiro. Hydrodynamic instability and coalescence of binary neutron stars. **ApJ**, 420:811–829, January 1994.

L. D. Landau and E. M. Lifshitz. *Statistical Physics, Part I.* Pergamon, Oxford, 1993.

J. S. Langer. Statistical theory of the decay of metastable states. **Ann. Phys.**, 54:258–275, 1969.

J. M. Lattimer, M. Prakash, D. Masak, and A. Yahil. Rapidly rotating pulsars and the equation of state. **ApJ**, 355:241–254, May 1990.

A. Lichnerowicz. *Relativistic hydrodynamics and magnetohydrodynamics.* New York, USA: Benjamin, 1967.

E. M. Lifshitz and L. P. Pitaevskii. *Physical Kinetics*. Butterworth-Heinemann, 1981.

I. M. Lifshitz and Yu. Kagan. Quantum kinetics of phase transitions at temperatures close the absolute zero. **Sov. Phys.-JETP**, 35:206–214, 1972.

R. N. Manchester, G. B. Hobbs, A. Teoh, and M. Hobbs. The atnf pulsar catalogue. *accepted by* **Astron. J** *(astro-ph/0412641)*, 2004.

V. S. Manko, E. W. Mielke, and J. D. Sanabria-Gomez. Exact solution for the exterior field of a rotating neutron star. **Phys. Rev.**, D61:081501, 2000.

P. Marronetti, G. J. Mathews, and J. R. Wilson. Irrotational binary neutron stars in quasiequilibrium. **Phys. Rev. D**, 60(8):087301, October 1999.

P. Marronetti, M. D. Duez, S. L. Shapiro, and T. W. Baumgarte. Dynamical Determination of the Innermost Stable Circular Orbit of Binary Neutron Stars. **Phys. Rev. Lett.**, 92 (14):141101, April 2004.

F. E. Marshall, E. V. Gotthelf, W. Zhang, J. Middleditch, and Q. D. Wang. Discovery of an Ultrafast X-Ray Pulsar in the Supernova Remnant N157B. **ApJ**, 499:L179, June 1998.

A. B. Migdal. Stability of vacuum and limiting fields. **Zh. Eksp. Teor. Fiz.**, 61:2209–2224, 1971.

A. B. Migdal. Phase transitions in nuclear matter and non-pair nuclear forces. **Sov. Phys.-JETP**, 36:1052–1055, 1972.

J. Miralda-Escudé, B. Paczynski, and P. Haensel. Thermal structure of accreting neutron stars and strange stars. **ApJ**, 362:572–583, October 1990.

C.W. Misner, K.S. Thorne, and J.A. Wheeler. *Gravitation*. W.H. Freeman, New York, 1973.

D. J. Nice, E. M. Splaver, and I. H. Stairs. Heavy Neutron Stars? A Status Report on Arecibo Timing of Four Pulsar - White Dwarf Systems. In **IAU Symposium**, page 49, 2004.

T. Norsen. Strangeness nucleation in neutron star matter. **Phys. Rev. C**, 65(4):045805, April 2002.

T. Norsen and S. Reddy. First order kaon condensation in neutron stars: Finite size effects in the mixed phase. **Phys. Rev. C**, 63(6):065804, June 2001.

R. Oechslin, K. Uryū, G. Poghosyan, and F. K. Thielemann. The influence of quark matter at high densities on binary neutron star mergers. **Mon. Not. R. Astron. Soc.**, 349: 1469–1480, April 2004.

R. C. Oppenheimer and G. M. Volkoff. On Massive Neutron Cores. **Phys. Rev.**, 55: 374–381, February 1939.

F. Pacini. Energy emission for a neutron star. **Nature**, 216:567–568, 1967.

V. R. Pandharipande and D. G. Ravenhall. Hot Nuclear Matter. In *NATO ASIB Proc. 205: Nuclear Matter and Heavy Ion Collisions*, pages 103–132, 1989.

C. J. Pethick and D. G. Ravenhall. Matter at large neutron excess and the physics of neutron-star crusts. **Annu. Rev. Nucl. Part. Sci.**, 45:429–484, 1995.

J. A. Pons et al. Kaon condensation in proto-neutron star matter. **Phys. Rev.**, C62: 035803, 2000.

M. Prakash, I. Bombaci, M. Prakash, P. J. Ellis, J. M. Lattimer, and R. Knorren. Composition and structure of protoneutron stars. **Phys. Rep.**, 280:1–77, 1997.

W. H. Press, S. A. Teukolsky, W. T. Vetterling, and B. P. Flannery. *Numerical recipes in C. The art of scientific computing.* Cambridge: University Press, 1992, 2nd ed., 1992.

H. Quaintrell, A. J. Norton, T. D. C. Ash, P. Roche, B. Willems, T. R. Bedding, I. K. Baldry, and R. P. Fender. The mass of the neutron star in Vela X-1 and tidally induced non-radial oscillations in GP Vel. **A&A**, 401:313–323, April 2003.

D. G. Ravenhall, C. J. Pethick, and J. R. Wilson. Structure of matter below nuclear saturation density. **Phys. Rev. Lett.**, 50:2066–2069, 1983.

P. Ring and P. Schuck. *The Nuclear Many Body Problem.* Berlin, Springer, 1980.

M. Salgado, S. Bonazzola, E. Gourgoulhon, and P. Haensel. High precision rotating netron star models 1: Analysis of neutron star properties. **A&A**, 291:155–170, November 1994.

E. E. Salpeter. Matter at High Densities. **Ann. Phys.**, 11:393, 1960.

R. F. Sawyer. Condensed π^- phase in neutron star matter. **Phys. Rev. Lett.**, 29:382–385, 1972.

D. J. Scalapino. π^- condensate phase in dense matter. **Phys. Rev. Lett.**, 29:386–388, 1972.

R. Schaeffer, L. Zdunik, and P. Haensel. Phase transitions in stellar cores. I - Equilibrium configurations. **A&A**, 126:121–145, September 1983.

S. L. Shapiro and S. A. Teukolsky. Gravitational collapse to neutron stars and black holes - Computer generation of spherical spacetimes. **ApJ**, 235:199–215, January 1980.

M. Shibata. Relativistic formalism for computation of irrotational binary stars in quasiequilibrium states. **Phys. Rev. D**, 58(2):024012, July 1998.

M. Shibata and M. Sasaki. Innermost stable circular orbits around relativistic rotating stars. **Phys. Rev. D**, 58(10):104011, November 1998.

M. Shibata and K. ō. Uryū. Computation of gravitational waves from inspiraling binary neutron stars in quasiequilibrium circular orbits: Formulation and calibration. **Phys. Rev. D**, 64(10):104017, November 2001.

M. Shibata, K. Taniguchi, and K. Uryū. Merger of binary neutron stars of unequal mass in full general relativity. **Phys. Rev. D**, 68(8):084020, October 2003.

L. Smarr and J. W. York. Kinematical conditions in the construction of spacetime. **Phys. Rev. D**, 17:2529–2551, May 1978.

R. D. Sorkin. A Criterion for the Onset of Instability at a Turning Point. **ApJ**, 249:254, October 1981.

R. D. Sorkin. A Stability Criterion for Many Parameter Equilibrium Families. **ApJ**, 257: 847, June 1982.

N. K. Spyrou and N. Stergioulas. Spin-down of relativistic stars with phase transitions and PSR J0537-6910. **A&A**, 395:151–160, November 2002.

I. H. Stairs. Pulsars in Binary Systems: Probing Binary Stellar Evolution and General Relativity. **Science**, 304:547–552, April 2004.

N. Stergioulas and J. L. Friedman. Comparing models of rapidly rotating relativistic stars constructed by two numerical methods. **ApJ**, 444:306–311, May 1995.

F. D. Swesty. Thermodynamically Consistent Interpolation for Equation of State Tables. **J. Comput. Phys.**, 127:118–127, 1996.

K. Taniguchi and E. Gourgoulhon. Quasiequilibrium sequences of synchronized and irrotational binary neutron stars in general relativity. III. Identical and different mass stars with γ=2. **Phys. Rev. D**, 66(10):104019, November 2002a.

K. Taniguchi and E. Gourgoulhon. Various features of quasiequilibrium sequences of binary neutron stars in general relativity. **Phys. Rev. D**, 68(12):124025, December 2003.

K. Taniguchi and E. Gourgoulhon. Equilibrium sequences of synchronized and irrotational binary systems composed of different mass stars in Newtonian gravity. **Phys. Rev. D**, 65(4):044027, February 2002b.

K. Taniguchi, E. Gourgoulhon, and S. Bonazzola. Quasiequilibrium sequences of synchronized and irrotational binary neutron stars in general relativity. II. Newtonian limits. **Phys. Rev. D**, 64(6):064012, September 2001.

S. A. Teukolsky. Irrotational Binary Neutron Stars in Quasi-Equilibrium in General Relativity. **ApJ**, 504:442, September 1998.

R. C. Tolman. Static Solutions of Einstein's Field Equations for Spheres of Fluid. **Phys. Rev.**, 55:364–373, February 1939.

R. F. Tooper. Adiabatic Fluid Spheres in General Relativity. **ApJ**, 142:1541, November 1965.

K. ō. Uryū and Y. Eriguchi. New numerical method for constructing quasiequilibrium sequences of irrotational binary neutron stars in general relativity. **Phys. Rev. D**, 61 (12):124023, June 2000.

K. ō. Uryū, M. Shibata, and Y. Eriguchi. Properties of general relativistic, irrotational binary neutron stars in close quasiequilibrium orbits: Polytropic equations of state. **Phys. Rev. D**, 62(10):104015, November 2000.

R. M. Wald. *General Relativity*. Chicago, Usa: Univ. Pr., 1984.

F. Weber. Pulsars as astrophysical laboratories for nuclear and particle physics. *IoP Publishing, Bristol & Philadelphia*, 1999.

F. Weber and N. K. Glendenning. Exact versus approximate solution of einstein's equations for rotating neutron stars. **Phys. Lett.**, B265:1–5, 1991.

F. Weber and N. K. Glendenning. Application of the improved Hartle method for the construction of general relativistic rotating neutron star models. **ApJ**, 390:541–549, May 1992.

J. R. Wilson. Models of Differentially Rotating Stars. **ApJ**, 176:195, August 1972.

J. R. Wilson and G. J. Mathews. Instabilities in Close Neutron Star Binaries. **Phys. Rev. Lett.**, 75:4161–4164, December 1995.

J. R. Wilson, G. J. Mathews, and P. Marronetti. Relativistic numerical model for close neutron-star binaries. **Phys. Rev. D**, 54:1317–1331, July 1996.

E. Witten. Cosmic separation of phases. **Phys. Rev.**, D30:272–285, 1984.

J. L. Zdunik. Strange stars - linear approximation of the EOS and maximum QPO frequency. **A&A**, 359:311–315, July 2000.

J. L. Zdunik, P. Haensel, and R. Schaeffer. Phase transitions in stellar cores. II - Equilibrium configurations in general relativity. **A&A**, 172:95–110, January 1987.

J. L. Zdunik, P. Haensel, and E. Gourgoulhon. Recycling strange stars to millisecond periods. **A&A**, 381:933–940, January 2002.

J. L. Zdunik, P. Haensel, E. Gourgoulhon, and M. Bejger. Hyperon softening of the EOS of dense matter and the spin evolution of isolated neutron stars. **A&A**, 416:1013–1022, March 2004.